

AMERICAN UNIVERSITY OF BEIRUT

Breaking of symmetry in shallow rotating flows

by  
Ahmad Lalti

A thesis  
submitted in partial fulfillment of the requirements  
for the degree of Master of Science  
to the Department of Physics  
of the Faculty of Science  
at the American University of Beirut

Beirut, Lebanon  
May 2018


# AMERICAN UNIVERSITY OF BEIRUT

## Breaking of symmetry in shallow rotating flows

by  
Ahmad Lalti

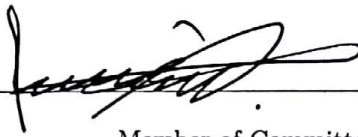
Approved by:

\_\_\_\_\_  
Dr. Ghassan Antar, Professor

  
Advisor


Physics

\_\_\_\_\_  
Dr. Jihad Touma, Professor

  
Member of Committee

Physics

\_\_\_\_\_  
Dr. Leonid Klushin, Professor

  
Member of Committee

Physics

Date of thesis defense: May 11, 2018

# AMERICAN UNIVERSITY OF BEIRUT

## THESIS, DISSERTATION, PROJECT RELEASE FORM

Student Name: Lalti Ahmad Radwan  
Last First Middle

Master's Thesis       Master's Project       Doctoral Dissertation

I authorize the American University of Beirut to: (a) reproduce hard or electronic copies of my thesis, dissertation, or project; (b) include such copies in the archives and digital repositories of the University; and (c) make freely available such copies to third parties for research or educational purposes.

I authorize the American University of Beirut, to: (a) reproduce hard or electronic copies of it; (b) include such copies in the archives and digital repositories of the University; and (c) make freely available such copies to third parties for research or educational purposes after: **One** \_\_\_ year from the date of submission of my thesis, dissertation or project.  
**Two** \_\_\_ years from the date of submission of my thesis, dissertation or project.  
**Three** \_\_\_ years from the date of submission of my thesis, dissertation or project.

  
Signature

15-5-2018  
Date

This form is signed when submitting the thesis, dissertation, or project to the University Libraries

# Acknowledgements

Firstly, I would like to thank my adviser Dr. Ghasan Antar for his continuous guidance and supervision throughout my research years, I am genuinely grateful for his patience. Also I would like to thank my thesis committee members, namely Dr. Leonid Klushin, and Dr. Jihad Touma for putting up the time to read my thesis and giving insightful comments and encouragements. A special thanks for Dr. Klushin, for his questions and remarks that are still giving me some hard time to answer. Last but not least, I would like to thank family and friends for providing me with the proper supportive and encouraging environment, without which this accomplishment wouldn't have been possible.

# An Abstract of the Thesis of

Ahmad Lalti for Master of Science

Major: Physics

Title: Breaking of symmetry in shallow rotating flows

We show theoretically and experimentally that the breaking of symmetry of shallow rotating axisymmetric flow is spontaneous and does not require forcing under certain flow parameters. To do this we build a novel experiment, in which a cylindrical container of radius  $R$  is placed in a set of electromagnets generating a uniform magnetic field in the  $z$ -direction. KOH solution is poured into the cylinder with a depth  $h$ , and a current is passed in it. The Lorentz force  $\vec{J} \times \vec{B}$  drives the rotation of the flow. Three flow regimes are explored. At shallow depth, or large aspect ratio  $\Gamma = R/h$ , and low Reynold's number  $Re = hV_\theta/\nu$ , the flow is laminar. At lower  $\Gamma$ s and higher  $Re$  the flow is subject to a primary axisymmetric instability due to the boundary layer near the outer edge of the flow. Finally, above a Reynolds number  $Re = 241$ , the symmetry of the primary flow is broken and non-axisymmetric vortices are formed. The source of the secondary structures is a shear layer in the  $(r - z)$  plane. These results are also confirmed using theoretical analysis, where we modeled the primary flow by two counter

rotating vortices. We perform linear stability analysis on this base flow, and we find that the conditions for the instability are close to those of the experiment. We conclude that the symmetry of shallow rotating flows is *naturally* broken, due to the primary flow dynamics, if the Reynold's number is high enough.

# Contents

<b>Acknowledgements</b>	<b>v</b>
<b>Abstract</b>	<b>vi</b>
<b>1 Introduction</b>	<b>1</b>
1.1 Motivation . . . . .	1
1.2 Literature review . . . . .	2
<b>2 Experimental setup, diagnostics and data processing</b>	<b>6</b>
2.1 Introduction . . . . .	7
2.2 The KOH solution . . . . .	8
2.3 The magnetic field . . . . .	9
2.4 The electrical current flowing in the KOH solution . . . . .	10
2.5 Quantitative and Qualitative Diagnostics . . . . .	11
2.5.1 Qualitative measurements . . . . .	12
2.5.2 Quantitative measurements . . . . .	12
2.6 Numerical Codes for Velocity Measurements . . . . .	12
2.6.1 Eulerian code for velocity measurements . . . . .	14
2.6.2 Lagrangian code for particle tracking . . . . .	16

<b>3</b>	<b>Experimental results</b>	<b>18</b>
3.1	Preliminaries . . . . .	18
3.2	Laminar flow at high aspect ratio . . . . .	20
3.3	The Primary axially symmetric flow . . . . .	21
3.4	Stability of the axially symmetric flow at different Reynold's number	23
3.4.1	Critical Reynold's number . . . . .	25
3.5	Stability of the Taylor Couette flow at different aspect ratio . . . .	27
3.6	Variation of the experimental setup . . . . .	30
3.6.1	Effect of current profile variations . . . . .	30
3.6.2	Dynamical similarity of the flow . . . . .	32
3.7	Conclusion . . . . .	34
<b>4</b>	<b>Stability Theory of Thin Rotating Flows</b>	<b>35</b>
4.1	Introduction . . . . .	36
4.1.1	A review of basic Fluid concepts . . . . .	36
4.2	Laminar flows at Large Aspect Ratio . . . . .	43
4.3	The Taylor-Couette instability . . . . .	47
4.4	Secondary Instability and the Breaking of Axisymmetry . . . . .	52
4.5	Conclusion . . . . .	69
<b>5</b>	<b>Conclusions and Future works</b>	<b>70</b>
	<b>Appendices</b>	<b>72</b>
<b>A</b>	<b>Submitted paper</b>	<b>73</b>



# List of Figures

1.1	(a) Schematics of the experimental setup used in [1], (b) Schematics of the flow studied in Ref. [2] . . . . .	4
2.1	This figure shows the experimental setup used. (1) indicates the electromagnets, (2), the cylinder with the inner and outer electrodes, (3), the UV lights, (4) the camera and (5) the power supply used to pass the current in the fluid. . . . .	7
2.2	Dynamics of the electrodes . . . . .	9
2.3	plot of the variation of the magnetic field as a function of the radius at a fixed z position in the cylinder. . . . .	10
2.4	(a) raw image taken from the video. (b) image after application of the mask. (c) image after subtracting the average image and applying the high pass filter. (d) image after zeroing low intensity noise . . . . .	13
2.5	Schematics of continuity condition employed in Both Lagrangian and Eulerian codes . . . . .	14
2.6	Getting an average $V_r$ velocity from the tracking of one bead. . .	16

3.1	$V_\theta/V_9$ vs $r$ with $V_9 = V_\theta(r = 9\text{cm})$ , for $Re = 11, 18$ and $24$ overlaid with an average experimental profile in black dots, and a theoretical profile in red dots . . . . .	21
3.2	At $h = 1.5$ cm this figure shows the stable primary axisymmetric vortex confined to the region $[R - h, R]$ at $Re = 206$ . . . . .	22
3.3	$\partial_r (rV_\theta)^2$ vs $r$ for $Re = 162$ and $241$ . . . . .	23
3.4	At $h = 1.5$ cm this figure shows the evolution with time from the stable primary flow shown in (a) taken to be at $t = 0$ and $Re = 206$ , (b) an intermediate step after we increase $Re$ to $241$ , and (c) the fully developed secondary instability . . . . .	23
3.5	(a) $V_\theta$ vs $r$ and (b) $\delta V_\theta$ vs $r$ at $Re = 162$ and $241$ while (c) shows $V_r$ vs $r$ at $Re = 206$ . . . . .	25
3.6	(a) $V_\theta$ at $r = R - h = 8$ vs time and (b) $\delta V_\theta$ at $r = R - h = 8$ cm vs time overlaid with the growth rate of the instability $\gamma$ at $Re = 262$ and (c) $\delta V_\theta$ vs $Re$ as we increase the Reynold's number from $166$ to $216$ to $262$ . . . . .	26
3.7	At $h = 2.5$ cm this figure shows the evolution with time of the flow starting from rest, (a) is taken at $t = 16$ (s) after we increase the current from $0$ to $120$ mA, (b) through (d) shows the evolution of the secondary instability with time . . . . .	28
3.8	This figure shows (a) $V_\theta$ vs $r$ and (b) $\delta V_\theta$ vs $r$ at $Re = 244$ and $377$ while (c) shows $V_r$ vs $r$ at $Re = 318$ . . . . .	29
3.9	(a) $m=6$ instability at $\Gamma = 3.86$ , (b) $m=10$ instability at $\Gamma = 6.4$ , (c) $m=19$ instability at $\Gamma = 32$ . . . . .	30
3.10	Two cylindrical containers, of respective radii of $4.5$ and $9.65$ cm from left to right. . . . .	31

3.11	(a) container with outer one continuous sheet electrode. (b) container with 16 outer electrodes. (c) container with 8 outer electrodes. All with a radius of 4.6 cm. . . . .	31
3.12	(a) shows an $m=6$ non-axisymmetric instability in the sheet setup. (b) shows an $m=4$ non-axisymmetric instability in the rod setup, both at a current of 85 mA, and $\Gamma = 3$ . . . . .	32
3.13	$m=5$ instability for at a current of 80 mA, in a fluid with $\Gamma = 3.86$ in the cylinder with radius (a) $R = 4.6$ cm and (b) $R = 9.65$ cm .	33
3.14	plot of the variation of the magnetic field as a function of the radius at a fixed $z$ position using a permanent magnet. . . . .	33
4.1	Variation of average temperature inside a fluid element with variation of its scale. [3] . . . . .	37
4.2	(a) pressure forces, (b) viscous forces . . . . .	40
4.3	Experimental profile for $V_\theta$ as a function of $r$ overlaid with the theoretical profile taken the outer boundary condition as (a) experimental value of $V_\theta$ , (b) no slip boundary condition . . . . .	46
4.4	$V_\theta$ vs $r$ for a current density that is proportional to $\exp(-(r-a)/\lambda)$ in dashed blue line overlaid with the same plot but for a current density proportional to $1/r$ . . . . .	47
4.5	Schematics of the modeled cylindrical channel flow . . . . .	53
4.6	Schematics of the modeled cartesian channel flow . . . . .	56
4.7	Streamlines of the zeroth order profile in normalized units . . . .	57
4.8	$\gamma_1$ and $\gamma_2$ plotted as a function of $x$ and $y$ . . . . .	62
4.9	$\gamma$ plotted as a function of $r$ and $z$ for $\lambda_r = 6h$ , $\lambda_z = 60h$ , $m = 2$ , $Re = 205$ and $\delta V_r/V_\theta = 0.0145$ . . . . .	64

4.10	(a) periodic zeroth order velocity profile (b) the instability over four vortexes . . . . .	65
4.11	$\gamma$ vs $m$ for $\lambda_z$ between $8h$ and $500h$ with a logarithmic scale between the $\lambda_z$ s. Curves with $\lambda_z = 15h$ and $100h$ are highlighted to stress on the fact that they are the curves between which the maximum $\gamma$ point, or the point of highest instability growth rate, varies between $m = 2$ and $m = 12$ . . . . .	66
4.12	$\gamma$ (1/s) vs $m$ for different Reynold's numbers taken at $h = 1.5$ cm with $K_z = \pi/25$ $K_r = \pi/(2 \times \text{width of the channel})$ in normalized units, (a) for aspect ratio $\Gamma = 1$ and with a maximum $\gamma$ at $m_{max} = 2$ for all Reynold's numbers, (b) for aspect ratio $\Gamma = 2$ and with a maximum $\gamma$ at $m_{max}$ between 4 and 5, (c) for aspect ratio $\Gamma = 4$ and with a maximum $\gamma$ at $m_{max}$ between 5 and 7 . . . . .	68

# List of Tables

3.1 ..... 19

# Chapter 1

## Introduction

### 1.1 Motivation

A realistic description of any dynamical system usually includes rotational degrees of freedom. They add to the complexity of the problem and cause the emergence of new behavior that is unknown without rotation. This also applies to fluid dynamics, where new instabilities and behavior emerge just by making the fluid rotate. Although intrinsically complicated, studying rotating flows is inevitable when tackling a real world fluid dynamics problem due to their abundance [4]. Understanding their stability is essential for the understanding of many physical phenomena, from planetary atmospheres to accretion disks around black holes. Also essential for the development and optimization of many engineering systems that interacts with rotating fluids, from accounting for the pressure variation in curved pipes, to accounting for the energy dissipation due to fluid rotation in pumps and jet engines.

While tackling such complex problems, one seeks to employ as many simplifying assumptions and exploit any symmetry in the system to make the problem

easier to solve. One symmetry that is of great importance to many fluid flows is axisymmetry, where the fluid rotates around a common fixed axis of symmetry. The properties of these flows are invariant under the rotation around that axis. Axisymmetric flows have been extensively studied both theoretically and experimentally. One example is the Taylor-Couette flow, in which an axisymmetric fluid rotates between two concentric cylinders [5]. We will review this flow in chapter 4. Another example to that is accretion disks around black holes, where a gas rotates in a disk of thickness much less than the radius of the disk, around a central heavy object. Assuming a Keplerian velocity profile for the disk seems intuitive, but it does not match the observed turbulent profile in the disks. Keplerian profiles always satisfied Rayleigh stability criterion [6], namely that  $\frac{d(r^2\Omega)^2}{dr} > 0$  where  $r$  is the radius from the center at a fixed  $z$ , and  $\Omega$  is the angular velocity of the fluid at a certain radial position (more on the criterion in chapter 4). This was resolved by Steven A. Balbus who showed the importance of the magnetic field perturbation in destabilizing the flow [7, 8, 9]. Namely, any magnetic field even with small magnitude, renders the disk unstable to what is called Magneto-Rotational Instability (MRI), an axisymmetric instability, under the condition:  $\frac{d\Omega^2}{dr} < 0$ .

Research is still on going to answer the question: what is driving the breaking of axisymmetry in rotating flows. The purpose of this thesis is to investigate experimentally and theoretically a new mechanism for symmetry breaking.

## 1.2 Literature review

Driven by different applications, many experiments were developed to simulate and study non-axisymmetric structures. In general, we could divide these ex-

periments into two general categories: experiments with barotropic flow, and experiments with baroclinic flow. Barotropic flow is a fluid generally with constant density, or a density that depends only on pressure. The velocity profile in barotropic flows are generally similar to those of a shear layer as defined in [3], mainly “a flow in which the velocity varies principally in a direction at right angles to the flow direction”. On the other hand, baroclinic flows are generally fluids with density that vary with both pressure and temperature. The velocity profile in such flows usually vary with the depth of the axial direction.

For experiments involving barotropic flows, one could refer to the following review articles [10, 11, 12]. The experimental setup usually is a variation of the following: a cylindrical closed tank with a fluid, usually water, rotating on a spinning table, so that the fluid achieve rigid rotation, Fig. 1.1 (a) shows an example of a barotropic experiment used by [1]. A shear layer is imposed on the fluid by different techniques usually involving differential rotation of a part of the top and bottom boundaries of the tank to create a shear layer see Refs. [13, 14, 15] to name a few, or to create a jet in the bulk of the fluid, see Refs. [16, 1]. Each of these experiments characterize the dimensionless numbers that are best suited to describe the flow. For example Ref. [13], used a Reynold’s number defined as  $Re = \Delta\Omega Rh/\nu$  to characterize the breaking of axisymmetry, and found a critical value  $Re_c = 85 - 110$  depending on the aspect ratio of the flow  $\frac{R}{h}$ . Here  $R$  is the radius of the container,  $h$  is the depth of the fluid  $\Delta\Omega$  is the discontinuity in the angular velocity around the shear layer, and  $\nu$  the kinematic viscosity of the fluid. Also, the authors in this reference studied the evolution of the number of vortices of the non-axisymmetric flow with the variation of the flow parameters, and what they found is that the mode number  $m$  is inversely proportional to  $h$ , and  $Re$ . On the other hand, Ref. [1] found that a better



Reynold's number would be  $Re = VL/\nu$  with  $V = \omega a/2$ ,  $L = (E/4)^{1/4} H$  with  $a$  the radial location of the shear layer,  $E = \nu/(\omega H^2)$  the Ekman number and  $H$  the depth of the flow. The results are in good agreement with linear stability model of the flow, including Ekman friction.

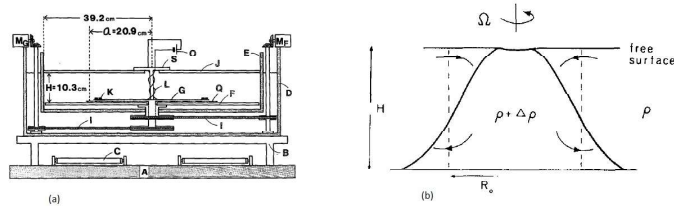


Figure 1.1: (a) Schematics of the experimental setup used in [1], (b) Schematics of the flow studied in Ref. [2]

For baroclinic experiments the setup used include variation of one of the flow parameters with depth. For example, Ref. [2] uses a flow where there is a density variation with height, a tank full of a fluid of density  $\rho$  rotates rigidly, with a bottomless cylinder in the middle containing a fluid of density  $\rho + \Delta\rho$ , when the cylinder is removed the interaction between the two fluids creates a shear layer. A schematic of the baroclinic flow is shown in Fig. 1.1 (b). On the other hand, Ref. [17] varies temperature with height. Two concentric cylinders are filled with a fluid, then the temperature of the walls of the cylinder are varied with height. The authors of Ref. [18] use a cylindrical container in which the top and bottom lids have separate angular velocities, creating a shear layer in the  $z$  direction.

All of the above experiments are designed in such a way to artificially force a shear layer in the flow. Ref. [19, 20] uses an electrolyte between two cylindrical electrode sheets and an axial magnetic field of a certain configuration to drive the flow. In this way, there is no shear layer of the azimuthal velocity in the radial direction created forcefully, but nevertheless it develops naturally near the

electrode cheats.

In this thesis we present a novel experiment in which an electrolyte is used with an axial magnetic field to drive the motion, but no apparent shear layer in the  $(r-\theta)$  plane is formed, yet we achieve symmetry breaking. We show, experimentally and theoretically that a shear layer in the  $(r-z)$  plane causes the transition, on top of that we calculate an experimental estimate of the critical Reynold's number, above which the flow becomes unstable, which turns out to be of the same order of magnitude as that gotten from the theoretical analysis. Furthermore, we find a trend between the mode number  $m$ , or the number of vortices resulting from the secondary instability, and the aspect ratio  $\Gamma = \Delta R/h$ , which is also reproduced theoretically. In Chapter 2, we describe in details the experimental setup and the diagnostics used to fully characterize the flow. In chapter 3, we present the experimental results at different heights and different Reynold's number, from them we characterize the flow stability, and propose a mechanism for symmetry breaking. In chapter 4 we model the axisymmetric base flow and then apply linear theory analysis to probe its stability, we then reproduce the conclusions gotten from the experimental results. In chapter 5, we present the possible developments to the experiment that can increase the accuracy of the results and the possible future work that can be done. A paper under development to be submitted to Journal of Fluid dynamics is attached in Appendix A.

## Chapter 2

# Experimental setup, diagnostics and data processing

## 2.1 Introduction



Figure 2.1: This figure shows the experimental setup used. (1) indicates the electromagnets, (2), the cylinder with the inner and outer electrodes, (3), the UV lights, (4) the camera and (5) the power supply used to pass the current in the fluid.

The previous chapter shows that most of the experiments that study non-axisymmetric structures in rotating flows force a shearing layer to develop. Our experiment is novel in the sense that the shearing layer, that causes the secondary vortices, is not forced.

The Rayleigh criterion is a criterion for the stability of cylindrically rotating flows [21], if met an axisymmetric instability will kick in the flow. In our experiment, this criterion is met due to the no slip boundary condition, which causes a radial gradient in the  $V_\theta$  velocity. An axisymmetric vortex is established in the flow.

Consequently the flow is divided into two parts: an outer axisymmetric vortex in the  $(r - z)$  plane rotating counter-clockwise, interacting with an inner vortex

rotating clockwise. This interaction creates a shear layer between those two vortices and causes the symmetry to be broken with suitable parameters. We use the experimental setup shown in Fig. 2.1. It consists of a Plexiglas cylindrical container of radius  $r= 9.65$  cm. With an inner stainless-steel rod shaped electrode, and a sheet electrode covering the inner face of the edge of the cylinder.

The cylinder is then filled with a Potassium Hydroxide solution at 26% mass concentration, the concentration at which the solution has maximum conductivity of about 55 S/m. A potential difference is applied between the electrodes, which causes a current to be driven in the solution.

The cylinder is placed at the center of a stack of electromagnets generating an axial magnetic field of the order of 45 mT.

The Lorentz force coming from the interaction of the magnetic field with the current in the solution,  $\vec{J} \times \vec{B}$ , drives the rotation of the flow.

Two main parameters are to be varied in this experiment. The aspect ratio of the experiment,  $\Gamma = \Delta R/h$ , which is the ratio of the difference in the radius between the outer and the inner electrodes to the depth of the fluid. The strength of the forcing varied by varying the potential difference between the outer and inner electrode, leading to different currents passing in the solution, hence different rotational velocities.

## 2.2 The KOH solution

The solution used for this experiment is Potassium Hydroxide at 26% mass concentration. This concentration was shown to have maximum electrical conductivity at room temperature. The KOH solution has a density of  $1246.85 \text{ Kg}/m^3$  [22] and a dynamic viscosity  $\mu$  of 1.57 mPa.s [23], it has a conductivity of  $\sigma = 56.95$

S/m at a temperature of  $T = 20^\circ \text{C}$  and a concentration of 26%wt [22]. One liter of the solution is prepared by mixing 260 g of KOH pellets with 1 L of water, then waiting for a while until the solution cools down since dissolving KOH in water is exothermic.

## 2.3 The magnetic field



Figure 2.2: Dynamics of the electrodes

The magnetic field is generated by a stack of four electromagnets connected in parallel to a DC power supply. The dimensions of the electromagnets are shown in Fig. 2.2. The magnetic field produced is almost uniform. In the  $z$ -direction it varies linearly from 40 to 45 mT, while its variation in the radial direction from the center of the electromagnets to the edge is shown in figure 2.3.

The near uniformity of the magnetic field allows us to assume its constancy in any theoretical modeling of the system.

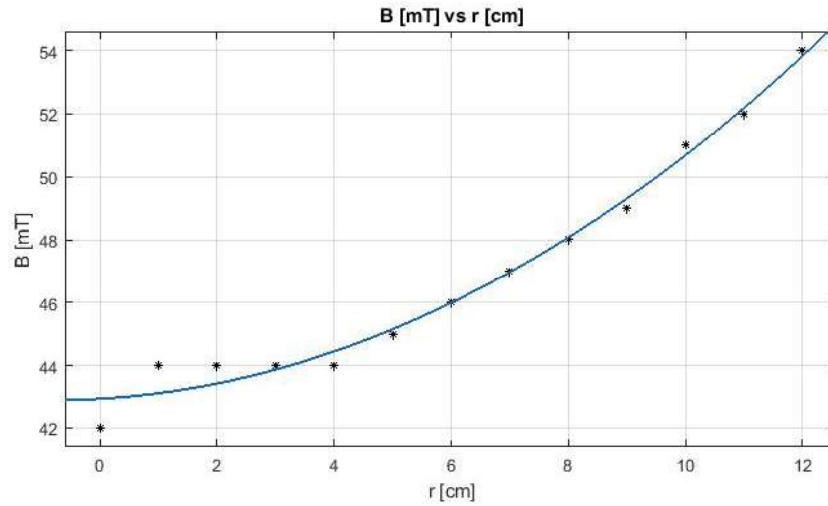


Figure 2.3: plot of the variation of the magnetic field as a function of the radius at a fixed  $z$  position in the cylinder.

## 2.4 The electrical current flowing in the KOH solution

The distribution of ions in an electrolytic solution can be assumed to be uniform in the bulk of the solution. On the other hand, at the electrode-electrolyte interface there is always an exchange of electrons, so this concentration must vary near that interface, and from that exchange of electrons a current is created in the solution.

Three processes control the transport of the electrolyte and the products of electrolysis from the interface to the bulk. These processes are: (1) ionic migration, (2) diffusion, and (3) convection. Each of these processes form a boundary layer with a certain width. The width of the boundary layer has been studied in depth throughout the literature for various assumptions and geometries [24, 25]. It is found that for the case of forced convection, where the bulk solution is being

stirred, over a flat plate, the thickness of the boundary layer is given by [25]:

$$\delta = 3 \left( \frac{\nu}{D} \right)^{-\frac{1}{3}} \left( \frac{\nu x}{U} \right)^{\frac{1}{2}} \quad (2.1)$$

With  $\nu$ ,  $D$ ,  $U$  and  $x$  being the dynamic viscosity  $\mu$  divided by the density  $\rho$ , named the kinematic viscosity, diffusion coefficient, bulk velocity of the fluid, and distance along the electrode from leading edge respectively. In our case  $x$  can be taken to be the depth of the fluid  $h$ .

Plugging the relevant numbers in our solution, we get a  $\delta$  of the order of 1 mm. Based on the analysis above, the current density profile can be assumed to have an exponentially decaying form

$$J = J_0 \exp(-(r - a)/\lambda)$$

with  $\lambda = \delta$  and  $a$  being the radius of the inner rod.

This current profile restricts the effect of the driving force to the center of the flow, to a region of radius of around a millimeter. While the bulk motion is due to viscously transporting that momentum outwards.

## 2.5 Quantitative and Qualitative Diagnostics

To study the dynamics and properly characterize the flow, we use a high-resolution camera to film the motion of the fluid. From the resultant video we infer quantitatively and qualitatively the characterization of the flow.



### 2.5.1 Qualitative measurements

Qualitative data is obtained using fluorescent material of density compared to that of water. This material emits in the green when exposed to ultraviolet(UV) light and allows us to visualize streamlines and different dynamical structures of the flow. Using analyses codes, we can better visualize the flow properties in space and time.

### 2.5.2 Quantitative measurements

Quantitative data is achieved by the virtue of fluorescent beads made of polyethylene, and of radius  $200 \mu m$ , which reacts with UV light of wavelength around  $365 \text{ nm}$  and emits in the green. Videos are taken with the beads moving on the surface of the fluid. The analysis of the videos allows us to measure surface velocity profiles, hence infer on the dynamics in a quantitative fashion. The camera resolution is  $2048 \times 1536$  and the field of view (FOV) is about  $24 \text{ cm}$ . Hence the camera can resolve around  $0.012 \text{ cm/pixel}$  and the videos are taken at a frame rate of 10 frames per second, which gives a time resolution of 0.1 seconds per frame. Knowing that on average one bead is around three pixels in diameter, and if we set the minimum distance for the bead to move to be its diameter, the lowest velocity that we can resolve would be  $0.3 \text{ cm/s}$ .

## 2.6 Numerical Codes for Velocity Measurements

Two separate codes were developed to analyze quantitatively the movies containing the fluorescent beads. One to calculate the flow velocity throughout the domain, in other words, it gives an Eulerian velocity field. The other code tracks each bead separately and saves its position and velocity throughout the video, in

other words, it gives a Lagrangian velocity field.

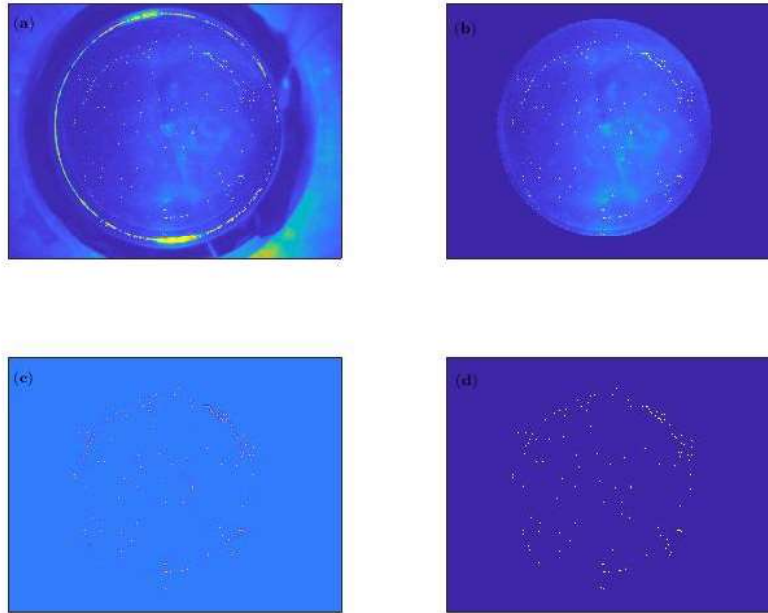


Figure 2.4: (a) raw image taken from the video. (b) image after application of the mask. (c) image after subtracting the average image and applying the high pass filter. (d) image after zeroing low intensity noise

The video is loaded into MATLAB and analyzed frame by frame. The image is initially transformed from uint8 to double format which allows us to arithmetically manipulate it as shown in Fig. 2.4(a). We remove unnecessary parts of the image, where no dynamics happens, by multiplying it by a mask, which is a matrix of the same size as the image with zeros in the undesired regions and ones in the remaining entries Fig. 2.4(b). Then, an average image is calculated, obtained by adding all the frames in the video and then divide the result by the number of frames in the movie. We subtract from each frame the average image. This will remove most of the static noise in the image. To eliminate low frequency noise

we apply a high pass filter to the image Fig. 2.4(c). Then a threshold intensity is calculated, under which all intensities are zeroed to keep the signature of the beads only. This intensity is calculated by getting the standard deviation of the intensities distributed in the pixels of the image, then multiplying it by 4. The final result contains the intensity peaks of the beads only and this is shown in Fig. 2.4(d).

### 2.6.1 Eulerian code for velocity measurements

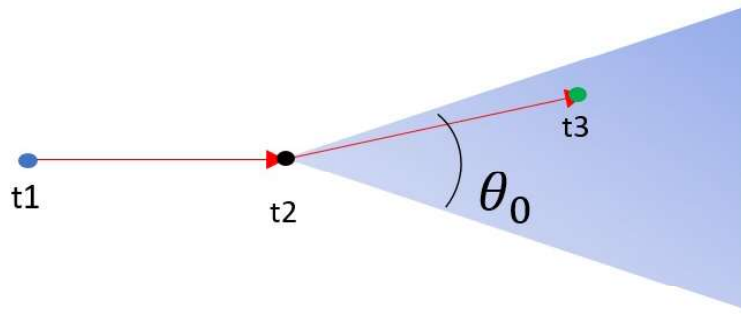


Figure 2.5: Schematics of continuity condition employed in Both Lagrangian and Eulerian codes

To determine the velocity of each bead as it moves in time, an intensity contour is taken, and a circle is fitted to the intensity peaks. The centers of the circles are taken to be the coordinates of the beads themselves. The error on the position of the beads is of the order of the radius of the beads, that is  $0.2[mm]$ .

After we get the positions of all the beads throughout the whole video, we go about calculating the velocities. First, we need to set a restriction on the maximum and minimum distance a bead could have traveled. We calculate the

distance between a chosen bead and all other beads in the next frame, and we get the bead from the next frame with the minimum distance. We do the same for all beads in the frame under study. Then we average this minimum distance, and we set it as half our maximum limit that any bead in this frame could travel. As for the minimum distance it is the diameter of a bead, so we set the minimum limit that any bead in this frame could travel to be the average diameter of all beads in the frame under study. Now in this frame we choose a bead, and we get its closest neighbor in both the previous frame and the next frame. If the distance between them falls in the range of minimum and maximum distances, then this bead is highly likely to be the same bead under study but at different instances in time. As a final check we apply a continuity condition, where we assume that under the time resolution, set by the frame rate of our experiment, both the magnitude and the direction of the velocity of the bead could not change drastically. So we calculate the velocity vector between the frames  $i$  and  $i + 1$ , and between frames  $i + 1$  and  $i + 2$  leading to two velocities  $V_{i,i+1}$  and  $V_{i+1,i+2}$  respectively. The angle between these two vectors could not be larger than a  $\theta_0$  which is of the order of  $10^\circ$ . So, if the calculated angle between these two vectors is larger than  $\theta_0$  then the bead is counted as lost and its position and velocity is discarded, otherwise the velocity of the bead in frame  $i + 1$  is calculated by central differencing with the following formula:

$$\vec{V}_{i+1} = \frac{\vec{X}_{i+2} - \vec{X}_i}{2\Delta t} \quad (2.2)$$

Where  $\vec{V}_{i+1}$  is the velocity vector of the bead at frame  $i + 1$ ,  $\vec{X}_i$  and  $\vec{X}_{i+2}$  are the position vector of the bead in frames  $i$  and  $i+2$  respectively, and  $\Delta t$  is the time between two successive frames, Fig. 2.5. We do this for all beads in a frame, and

for all frames in the video.

### 2.6.2 Lagrangian code for particle tracking

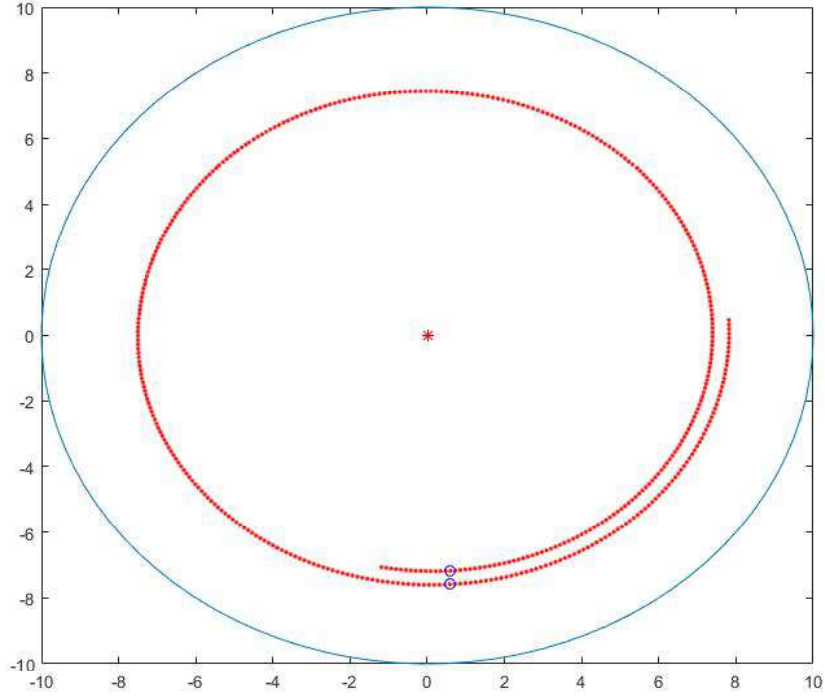


Figure 2.6: Getting an average  $V_r$  velocity from the tracking of one bead.

The radial velocity of the flow is much smaller than the azimuthal velocity, especially near the shear layer. To measure  $V_r$ , we developed a Lagrangian code that allows us to calculate the radial velocity profile. The code starts off the same as the Eulerian code up until we get the positions of each bead in the first frame.

In the first frame, we choose one bead. In the next frame we look for all beads in a box of sides 20 pixels by 20 pixels, centered around the position of the initial bead in the first frame. If the box contains more than one bead, then the same

continuity condition in the Eulerian code is employed. If the box is empty, we interpolate from previous positions of the same bead, if the bead is not found after 5 interpolations the bead is marked as lost.

From the tracking of each bead, we can calculate how much outwards did the bead travel after a full revolution figure 2.6. Knowing the time, it takes the bead to do a full revolution we can calculate an average  $V_r$  velocity.

# Chapter 3

## Experimental results

### 3.1 Preliminaries

Before presenting the experimental results, it is essential to define the nondimensional parameters that control the flow. First, we need to specify a scale length for our experiment. As will be discussed below, both the radius of the channel, and the depth of the fluid can be varied in such a way to produce dynamically similar flows. To get our results We fixed the radius and varied the depth of the fluid, hence the chosen scale length of our experiment is  $h$ , the depth of the fluid. It is worth noting that a lot of the experiments studying baroclinic instabilities also use  $h$  as their scale length, see Refs. [13, 16, 26] as an example. On top of that we choose the scale velocity of the fluid to be the azimuthal velocity of the fluid at the shear layer between the primary axisymmetric vortex and the bulk flow at a radius  $r = R - h$  with  $R$  being the outer radius of the cylinder, and  $h$  the depth of the fluid.

With these reference scales, we could define the non-dimensional numbers that characterize our flow. We characterize the axial variation of the flow with the

$h$ [cm]	$I_M$ [mA]	$V_\theta(r = (R - h))$ [cm/s]	$Re$	$E_k$	$\delta$ [mm]
0.3	60	0.48	11	2.6	4.9
0.3	90	0.72	18	1.7	3.9
0.3	120	1.01	24	1.2	3.3
1.5	60	1.36	162	$33 \times 10^{-3}$	2.7
1.5	90	1.73	206	$26 \times 10^{-3}$	2.4
1.5	120	2.02	241	$22 \times 10^{-3}$	2.2
2.5	60	1.23	244	$12 \times 10^{-3}$	2.7
2.5	90	1.6	318	$9 \times 10^{-3}$	2.3
2.5	120	1.9	377	$7 \times 10^{-3}$	2.2

Table 3.1:

Ekman number,  $E = \nu/\Omega h^2$ , defined as the ratio between the viscous forces and the Coriolis force in the flow. From this number we can infer on the effect of the boundary layer between the bulk rotation and the bottom of the container. For  $E \ll 1$ , this boundary layer does not have major effect on the flow and it can be neglected in the analysis. The thickness of that boundary layer is  $\delta = \sqrt{\nu/\Omega}$ . Table 3.1, Shows the values of the relevant dimensional and non-dimensional numbers characterizing our flow, at all the depth and current variations taken in our experiment. For the depth of 1.5 and 2.5 cm, the Ekman number is much smaller than unity, and the Ekman layer thickness is much smaller than the depth of the fluid, so away from that boundary layer viscous effects from the bottom can be neglected and the flow can be considered as barotropic. The case where  $h = 3$  mm has high Ekman number and the Ekman layer thickness is appreciable compared to the depth of the fluid, this case will be discussed in the next section.

The parameter that describe the transition from the primary to the secondary instability is the Reynold's number defined as  $Re = V_\theta h/\nu$ , where  $V_\theta$  is the characteristic velocity of the flow as defined above.



We need a quantitative way to tell when the instability kicks in. To do that, we use the standard deviation of  $V_\theta$ ,  $\delta V_\theta = \sqrt{\langle (u_\theta - V_\theta)^2 \rangle}$ , where  $\langle \rangle$  denotes averaged quantities over time and azimuthal angle. In the axisymmetric flow the dynamics are uniform, so the level of fluctuation of  $V_\theta$  is dominated by experimental noise. When the symmetry is broken, and non-axisymmetric vortices develops,  $V_\theta$  fluctuates even more, since there will be an exchange of momentum between the azimuthal direction and the radial direction, hence  $\delta V_\theta$  increases.

### 3.2 Laminar flow at high aspect ratio

We want to check whether our experimental measurement actually describes the flow dynamics. So we use a flow with depth  $h = 3$  mm, or an aspect ratio of  $\Gamma = 32$ . As is clear in Table 3.1, the size of the Ekman layer is comparable to the depth of the fluid, and the Ekman number is larger than 1, hence viscous effects are appreciable especially at the values of the Reynold's number that we used. This allow us to make some simplifying assumptions, for the flow at the surface of the fluid, which opens up the possibility to model the flow dynamics and get an analytical solution, this analysis will be presented in full in Chap. 4, we get the following analytical velocity profile

$$V_\theta = \frac{A}{r} + Cr + \frac{J_0 B_z \lambda^3}{\mu r} \exp(-r/\lambda) + \frac{J_0 B_z \lambda^2}{\mu} \exp(-r/\lambda) \quad (3.1)$$

gotten by solving the NS equations for a 2-D incompressible viscous axisymmetric flow, subject to a Lorentz force. We compare the theoretical profile, with the experimental measurement. Fig. 3.1 shows a plot of experimental  $V_\theta/V_9$  vs  $r$  at  $Re = 11, 18$  and  $24$  overlaid with the theoretical profile, where  $V_9$  is the

azimuthal velocity at  $r = 9$  cm. We see that far from the boundary, we have excellent agreement between theory and experiment, indicating that at this aspect ratio, the flow can be assumed to be two dimensional, and that the measurements are representative of the flow dynamics.

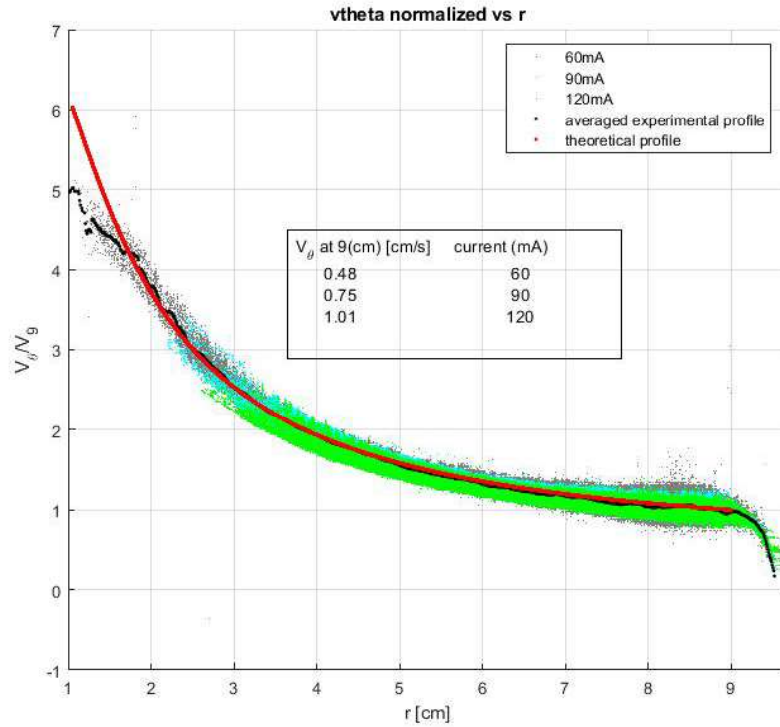


Figure 3.1:  $V_\theta/V_9$  vs  $r$  with  $V_9 = V_\theta(r = 9\text{cm})$ , for  $Re = 11, 18$  and  $24$  overlaid with an average experimental profile in black dots, and a theoretical profile in red dots

### 3.3 The Primary axially symmetric flow

At a relatively low Reynold's number the flow is unstable to axially symmetric perturbations. An axisymmetric vortex ring of radius equals to the depth of the fluid  $h$  is formed at the outer edge of the cylinder. This vortex ring forms a shear

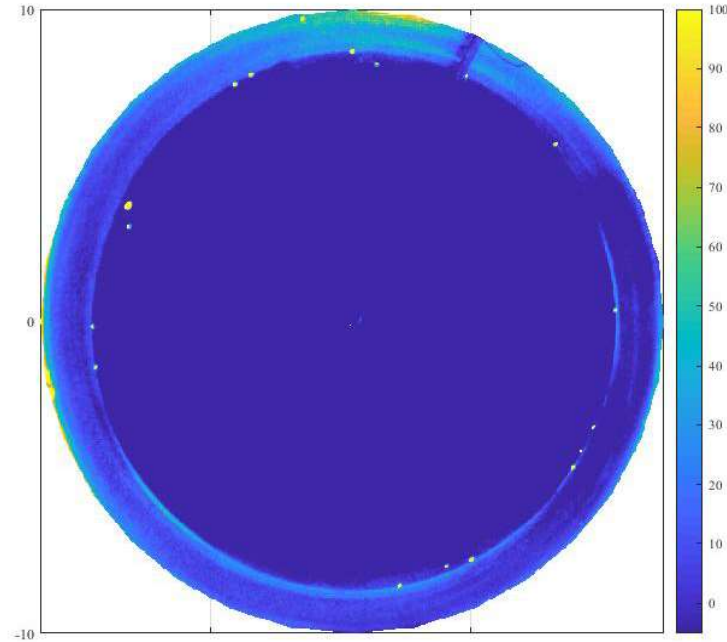


Figure 3.2: At  $h = 1.5$  cm this figure shows the stable primary axisymmetric vortex confined to the region  $[R - h, R]$  at  $Re = 206$ .

layer with the bulk flow. We can show the existence of this vortex ring and that its width is  $h$  both qualitatively and quantitatively. Fig. 3.2 (a) shows a fluid of depth 1.5 cm with  $Re = 206$ . We insert dye at the boundary of the container and wait for it to spread throughout the fluid following the streamlines of the flow. The dye does not penetrate the flow but is confined to an outer axisymmetric ring of width equals to  $h$ . Fig. 3.3 is a plot of  $\partial_r (rV_\theta)^2$  vs  $r$ , the Rayleigh criterion states that if this quantity is anywhere negative in the flow, then this region is unstable to axisymmetric perturbations. We see that the only region where this criterion is satisfied is between  $R - h$  and  $R$ . The above, complemented with the results of the next section, shows that there is an axisymmetric fluid ring near the edge of the container, with a width equals to the depth of the fluid.

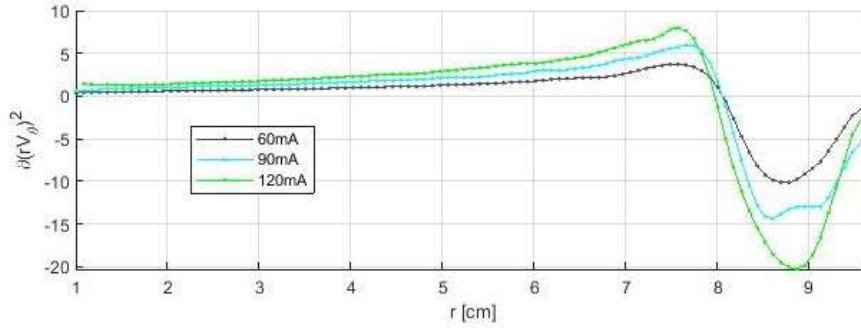


Figure 3.3:  $\partial_r (rV_\theta)^2$  vs  $r$  for  $Re = 162$  and  $241$

### 3.4 Stability of the axially symmetric flow at different Reynold's number

At the Reynold's number of 241, we see that another instability develops on top of the primary axisymmetric instability, with a growth time equals to around 100 (s) as shown qualitatively in Fig. 3.4. In this figure we insert the dye at the edge of the cylinder when the flow is with only the primary instability without the secondary instability at a  $Re = 206$ , then we increase the current and observe the transient behavior of the flow.

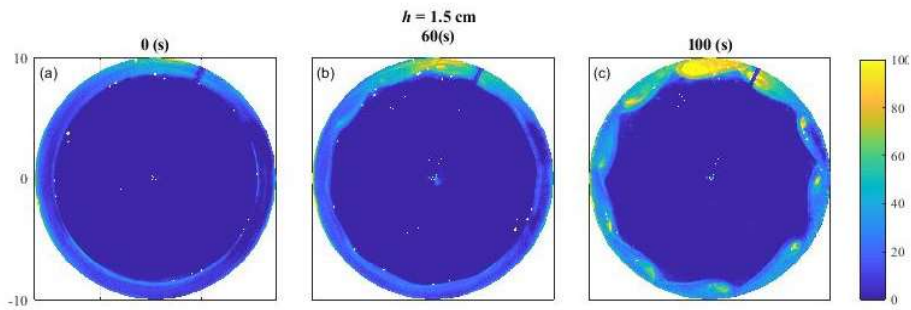


Figure 3.4: At  $h = 1.5$  cm this figure shows the evolution with time from the stable primary flow shown in (a) taken to be at  $t = 0$  and  $Re = 206$ , (b) an intermediate step after we increase  $Re$  to 241, and (c) the fully developed secondary instability

As shown in Chapter 1, most of the previous literature have a shear layer in the  $r - \theta$  plane that is at the heart of the symmetry breaking. But that is not the case in our experiment. Fig. 3.5 is a plot of the azimuthal and radial velocities, and the fluctuations in the azimuthal velocity vs the radius. To get to the data of this image, we run the experiment at a depth of  $h = 1.5$  cm giving an aspect ratio  $\Gamma = 6.4$ . We take several recordings of the flow each at different current after the flow had reached steady state, hence different Re, then we use the analysis code described in Chapter 2 to get to the required quantities. If we look at the  $V_\theta$  vs  $r$  profile for our flow shown in Fig. 3.5 (a) we see that there is no big gradients in  $V_\theta$  around the location of the shear layer between the vortex and the bulk flow. The only gradient is that due to the boundary layer which causes the axisymmetric instability in the first place. Fig. 3.5 (b) shows that at  $\text{Re} = 241$   $\delta V_\theta$  increases significantly around  $R - h$  indicating that the flow is unstable to secondary perturbations. We have a secondary instability that developed without any apparent shear layers in the  $(r-\theta)$  plane. We measure the radial velocity profile vs  $r$  in Fig. 3.5 (c). It shows that around  $R - h = 8$  cm  $V_r$  changes sign, so there is a maximum in the gradient of its profile at this location, due to the shear layer between the axisymmetric vortex and the bulk flow. From this we could infer that a secondary instability develops due to a shear layer, but contrary to previous literature, this shear layer is not in the  $(r - \theta)$  plane but coming from the gradients that are naturally occurring in the axisymmetric flow, mainly in the  $(r - z)$ -plane.

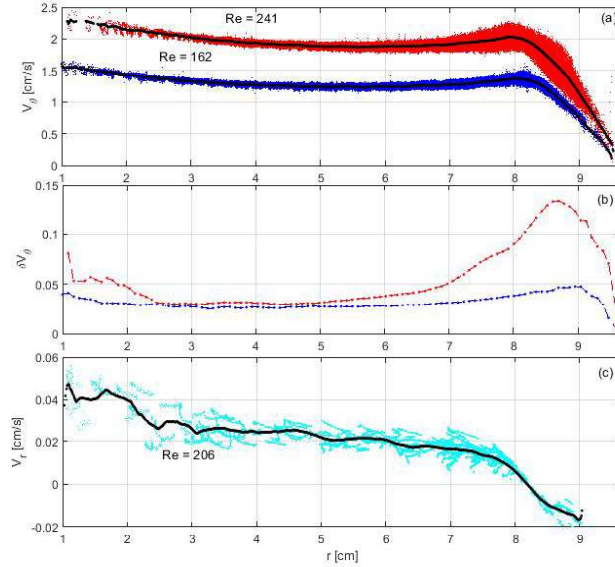


Figure 3.5: (a)  $V_\theta$  vs  $r$  and (b)  $\delta V_\theta$  vs  $r$  at  $Re = 162$  and  $241$  while (c) shows  $V_r$  vs  $r$  at  $Re = 206$ .

### 3.4.1 Critical Reynold's number

It is informative to get an estimate of the critical  $Re$ , above which the symmetry of the flow is broken.

Fig. 3.6 (a) and (b) shows a plot of  $V_\theta$  and  $\delta V_\theta$  vs time respectively, while Fig. 3.6 (c) shows  $\delta V_\theta$  vs  $V_\theta$ . The movie analyzed is taken with the fluid already in steady state axisymmetric flow at a current of 60 mA, then the current is increased to 90 mA, we wait till it reaches steady state, and finally increase the current to 120 mA. Qualitatively the flow at 60 and 90 mA is still an axisymmetric flow, while at 120 mA we have secondary instability.

This figure shows that at 60 and 90 mA  $\delta V_\theta$  is small and does not vary much, but when the current is increased to 120 mA, it starts increasing until it reaches a steady state value. Fig. 3.6 (a) shows that after around 120 seconds the value of  $V_\theta$  starts fluctuating around a mean value, concurrently with the development

of the secondary instability, this adds to the validity of using  $\delta V_\theta$  as an indicator of the secondary instability. The main purpose of this figure was to calculate the critical  $Re$  from Fig. 3.6 (c), which we thought it would be the  $Re$  at which  $\delta V_\theta$  starts to increase, and it turned out to be  $Re_c = 260$ . Looking at Fig. 3.5 (b), we see that we have an instability at  $Re = 241$ . To solve this, we calculated from Fig. 3.6 (b) the growth rate of the instability to be 25 seconds. But when we increase the current, the time it takes for the  $Re$  to reach its steady state value is less than the growth rate of the instability. Hence this method failed to serve its initial purpose but turned out to be informative as a check for the  $\delta V_\theta$  as an indicator of the presence of non-axisymmetric vortices.

So to get to the critical  $Re$ , we use information in Fig. 3.6 (c), namely that at  $Re = 216$  the flow is still stable. And we use Fig. 3.5 (a) and (b), which shows that at  $Re = 241$  the instability is present. From this we could set a range for the critical Reynold's number to be between 216 and 241.

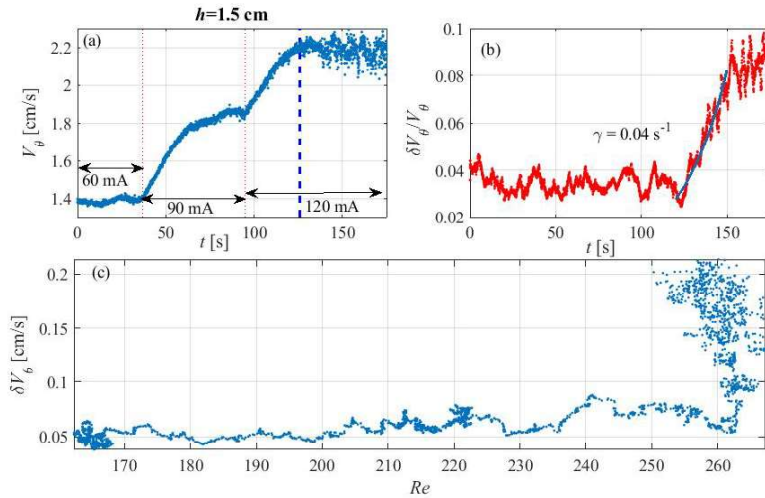


Figure 3.6: (a)  $V_\theta$  at  $r = R - h = 8$  vs time and (b)  $\delta V_\theta$  at  $r = R - h = 8$  cm vs time overlaid with the growth rate of the instability  $\gamma$  at  $Re = 262$  and (c)  $\delta V_\theta$  vs  $Re$  as we increase the Reynold's number from 166 to 216 to 262

### 3.5 Stability of the Taylor Couette flow at different aspect ratio

In this section, we vary the depth of the fluid to better understand the flow dynamics. From this we prove the importance of the depth  $h$  as the definition for the scale length of the flow. On top of that we show that the instability is generated from a shear layer located at  $r = R - h$ .

To understand the importance of  $h$  as the scale length of the flow, we use the same currents at  $h = 1.5$  cm for  $h = 2.5$  cm, namely 60, 90 and 120 mA. It turns out, as is shown in Table 3.1, that the values of  $V_\theta$  do not vary much between the two depth. If we define the Reynold's number with the radius of the container as the scale length, we would have two cases where the Reynold's number is comparable, but one is stable and the other is unstable. For example at 60 mA for  $h = 1.5$  cm, if we use  $R = 9.65$  cm as the scale length, we would get  $Re' = V_\theta R/\nu = 1042$ , and the system is stable. At 60 mA but for  $h = 2.5$  cm, for the same definition of  $Re'$ , we get  $Re' = 943$ , and the system is unstable. This clearly shows that using the radius of the container as the scale length of the flow is not a good choice. On the other hand, if we take the depth of the fluid to be the scale length, we see that at 60 mA and  $h = 1.5$  cm,  $Re = 162$ , less than the critical Reynold's number determined above. While at 60 mA and  $h = 2.5$  cm,  $Re = 244$  larger than the critical Reynolds number. So, this shows that the depth of the fluid is the suitable choice for the scale length of the flow.

Fig. 3.7 shows the evolution of the fluid motion from rest till steady state secondary flow. To get to this image we insert fluorescent dye on the surface of the fluid while at rest, then we turn on the current to 90 mA, and record a movie of the flow. We see that the dye in Fig. 3.7 (a) was distributed in the flow, then



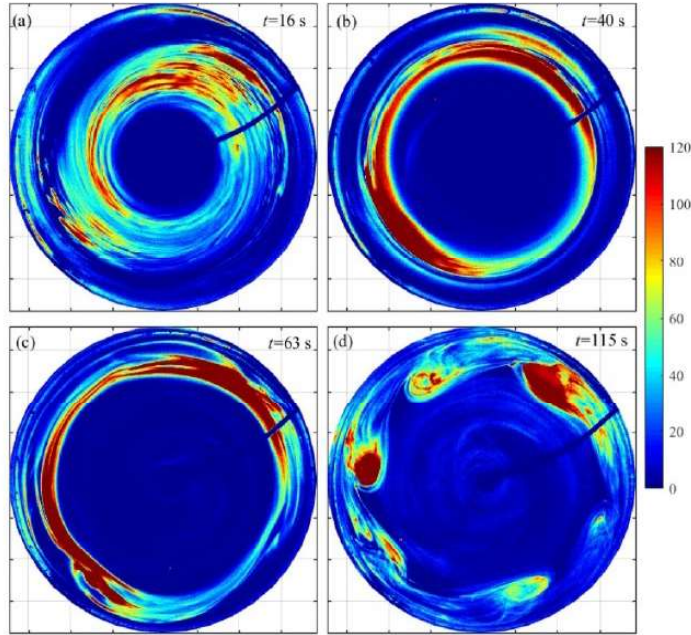


Figure 3.7: At  $h = 2.5$  cm this figure shows the evolution with time of the flow starting from rest, (a) is taken at  $t = 16$  (s) after we increase the current from 0 to 120 mA, (b) through (d) shows the evolution of the secondary instability with time

in (b) the dye started to gather at a distance  $r = R - h = 7$  cm away from the boundary, indicating the formation of an axisymmetric vortex of diameter equals to  $h = 2.5$  cm. Because the  $Re$  is larger than the critical  $Re$ , the flow is prone to secondary instability and Figs. 3.7 (c) and (d) shows the evolution of that instability. Qualitatively, from the fact that the initial axisymmetric vortex in Fig. 3.7 (b) had a width equals to  $h$ , and that the non-axisymmetric vortices in (d) have a diameter of  $h$ , we deduce that the shear layer is located at a radius  $r = R - h$ .

Fig.3.8 shows quantitatively the velocities of the flow at a depth of  $h = 2.5$  cm, and with currents ranging from 60 to 120 mA. (a) is a plot of  $V_\theta$  vs  $r$ , in

which we see that the region in which we have a gradient in the azimuthal profile now starts at a radius of  $r = R - h = 7.15$  cm. While (b) is a plot of  $\delta V_\theta$  vs  $r$ , it shows that the increase in  $\delta V_\theta$ , hence the location of the vortices, is also shifted to a radius of  $r = R - h = 7.15$  cm. Finally, (c) is a plot of  $V_r$  vs  $r$  at  $Re = 318$ , it shows a change of sign in  $V_r$  at  $r = 7.15$  cm, indicating the location of the interface between the outer vortex and the bulk flow, and showing a high gradient in  $V_r$  at that location. This figure restates that the instability is not due to a shear layer in the  $r - \theta$  plane, but a shear layer between different directions of the flow. And it also stresses on the fact that the location of the shear is not fixed, but it depends on the depth of the fluid,  $r_{shear} = R - h$ .

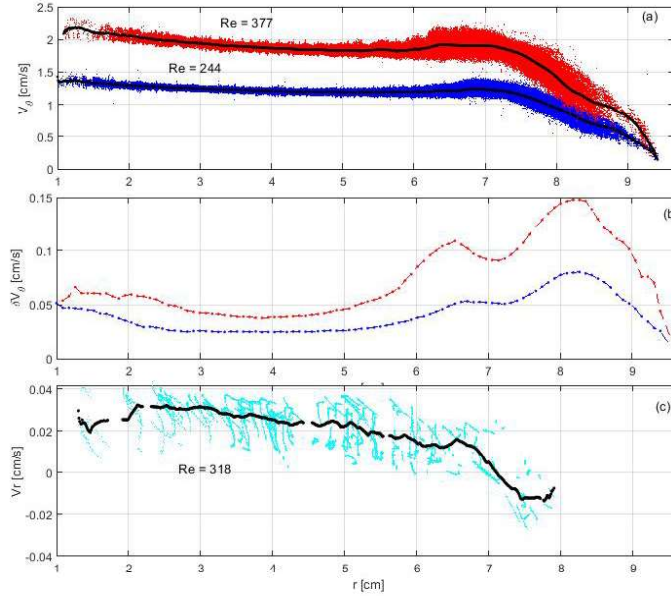


Figure 3.8: This figure shows (a)  $V_\theta$  vs  $r$  and (b)  $\delta V_\theta$  vs  $r$  at  $Re = 244$  and  $377$  while (c) shows  $V_r$  vs  $r$  at  $Re = 318$

On the other hand, for a height of  $h = 0.3$  cm we notice that for the currents used, the Reynold's number is always very low compared to the critical  $Re$ , and if we increase the  $Re$  above its critical value we will observe non-axisymmetric

vortices. This is clearly shown in Fig. 3.9 (c) showing the vortices at  $h = 0.3$  cm.

One more thing to add to this is the dependence of the mode number on the depth of the fluid. Fig. 3.9 compares between the mode number gotten at three different aspect ratios  $\Gamma = 3.86, 6.4$  and  $32$ . It shows that as we increase the aspect ratio the mode number  $m$  also increases from around 6, to around 10, to around 19 respectively. It is worth noting that the mode number have small dependence on the  $Re$ , where at a fixed  $Re$ ,  $m$  varies slightly. This trend is also reproduced in Chap. 4.

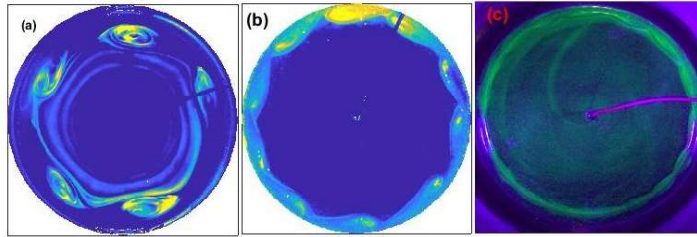


Figure 3.9: (a)  $m=6$  instability at  $\Gamma = 3.86$ , (b)  $m=10$  instability at  $\Gamma = 6.4$ , (c)  $m=19$  instability at  $\Gamma = 32$

## 3.6 Variation of the experimental setup

We explore the effect of varying the current profile by varying the geometry of the outer electrode in the cylinder. Also, we explore the dynamical similarity in the flow with the aspect ratio, and the minute effect of the magnetic field variations on the flow.

### 3.6.1 Effect of current profile variations

First we varied the geometry of the outer electrode, as shown in Fig. 3.11. This variation serves to test the effect of the  $\theta$  dependence of the current density

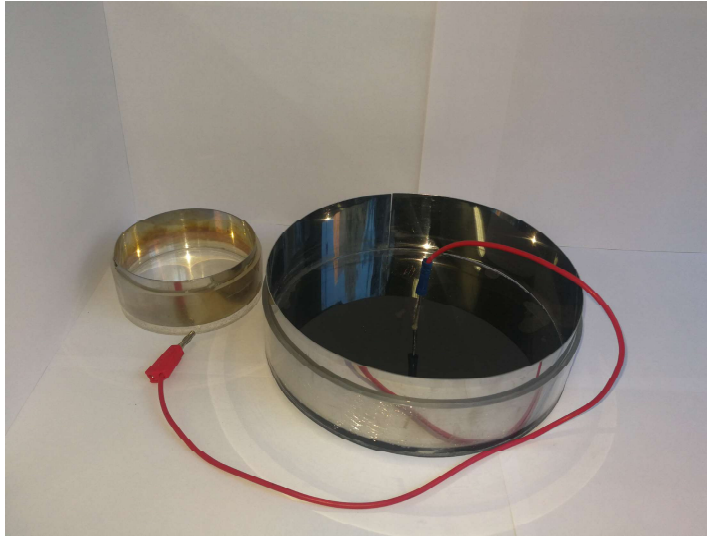


Figure 3.10: Two cylindrical containers, of respective radii of 4.5 and 9.65 cm from left to right.



Figure 3.11: (a) container with outer one continuous sheet electrode. (b) container with 16 outer electrodes. (c) container with 8 outer electrodes. All with a radius of 4.6 cm.

profile on the dynamics of the flow. Where the configuration of the electrode gives  $J(r, \theta)$  while the sheet electrode will have azimuthal symmetry and  $J(r)$  will be only radially dependent.

Fig. 3.12 shows that the dynamics of the secondary instability, for a flow with constant aspect ratio of  $\Gamma = 3$  and a constant current of 85 mA, changed significantly between the setup with outer rod electrodes, where  $J$  depends on  $\theta$ , and the setup with outer sheet electrode, where  $J$  independent on  $\theta$ . We notice that for the axisymmetric  $J(r)$ , the mode number  $m$  is equal to 6 and the vortices are more regularly distributed in the cylinder. On the other hand

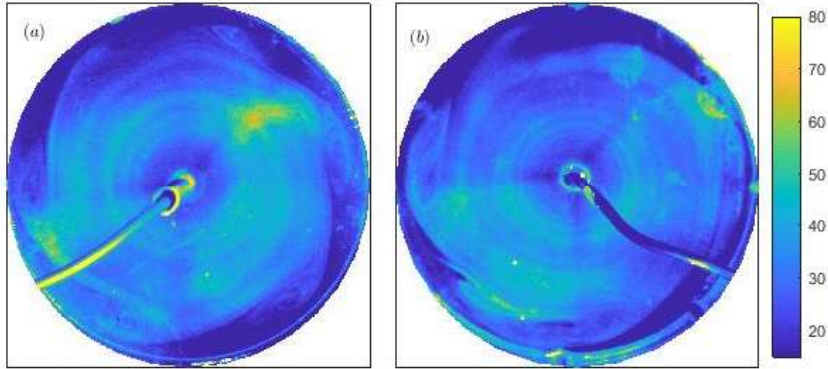


Figure 3.12: (a) shows an  $m=6$  non-axisymmetric instability in the sheet setup. (b) shows an  $m=4$  non-axisymmetric instability in the rod setup, both at a current of 85 mA, and  $\Gamma = 3$ .

for  $J(r, \theta)$ ,  $m = 4$  and the vortices are less regular. Although we can achieve axisymmetric flow in both setups before the secondary instability kicks in, the large effect of the rod electrodes on the secondary flow is not desirable since we are seeking to study the intrinsic causes of symmetry breaking and we do not want any external factor to enter into play. Hence, we chose to use the electrode sheet as the standard experimental setup of the experiment.

### 3.6.2 Dynamical similarity of the flow

We varied the radius of the cylinder, two radii were used, 9.65 cm and 4.5 cm shown in Fig. 3.10. Fig. 3.13 shows the secondary vortices gotten with the use of fluorescent dye, for two different radii of the cylinder, but varying the depth of the fluid in order to keep  $\Gamma$  constant. The magnetic field used for the big radius is generated by electromagnets and is plotted in Fig. 2.3, while  $B$  used for the small radius is generated by permanent magnets and is plotted in Fig. 3.14. In both cases we get the same mode number of the instability  $m = 5$ . From this

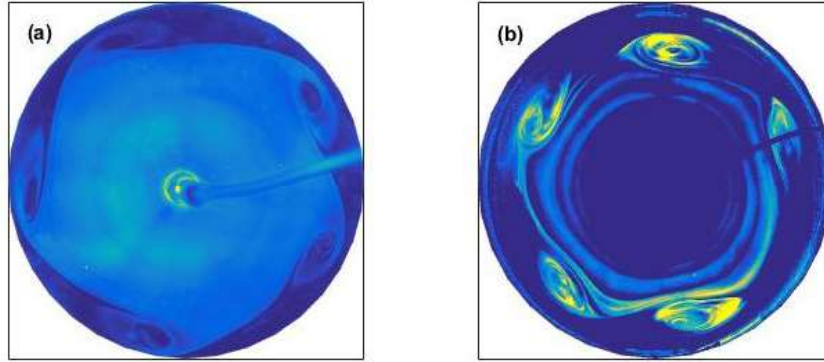


Figure 3.13:  $m=5$  instability for at a current of 80 mA, in a fluid with  $\Gamma = 3.86$  in the cylinder with radius (a)  $R = 4.6$  cm and (b)  $R = 9.65$  cm

we could conclude two things. First that we have dynamical similarity between the two cylinders. So, we choose to use the larger radius since it will allow us to explore larger variations in the aspect ratio. Second that the variation in the magnetic field has minor effects on the dynamics of the fluid and taking it to be constant in our theoretical model is justified.

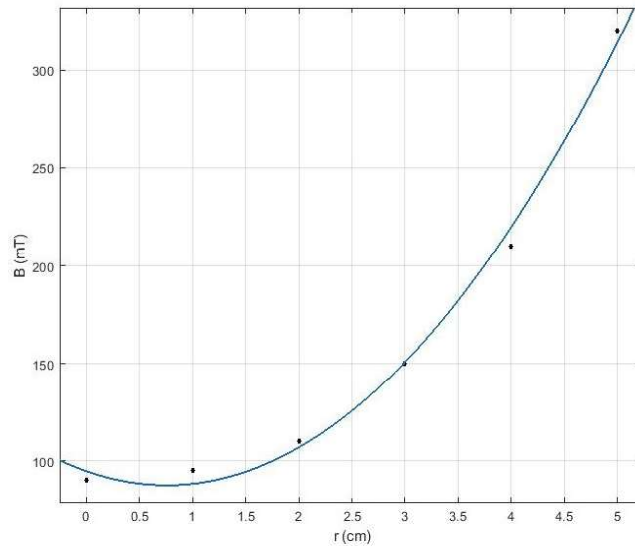


Figure 3.14: plot of the variation of the magnetic field as a function of the radius at a fixed  $z$  position using a permanent magnet.

### **3.7 Conclusion**

In this section we showed experimentally that the transition to non-axisymmetry occurs naturally on top of any axisymmetric vortex, above a critical Reynold's number. We also showed that the cause of this instability is a shear layer in a plane different than the radial-azimuthal plane. On top of that we showed that depth of the fluid has a big effect on the number of secondary vortices generated in the flow.

## Chapter 4

# Stability Theory of Thin Rotating Flows



## 4.1 Introduction

After exploring the experimental results, we analyze the flow theoretically, with the purpose of better exploring the correct parameters that mostly affect the development of the secondary instability. We first review basic concepts in fluid mechanics, then we study the two-dimensional flow in order to make sure that the experimental results are a good measure of the actual flow. We then review the physics of the Taylor-Couette instability, and finally we model the steady state axisymmetric flow and study its first order stability.

### 4.1.1 A review of basic Fluid concepts

To analyze theoretically the flow dynamics at hand we employ the machinery of fluid mechanics. In this section, we develop a quick overview of the basic concepts underlying conservation equations used to understand the onset of instabilities.

#### The continuum hypothesis

A fluid system is a dynamical system that is formed of a huge number of degrees of freedom, a number so big that attempting a particle dynamics analysis, or even a kinetic theory analysis is impossible. Assumptions must be made to progress in studying the macroscopic behavior of such systems. These assumptions should take us from a discrete particle or distribution of particles to a continuous field perspective. It allows us to introduce the concept of a *fluid/volume element*, over which the fields under study vary smoothly and continuously. This assumption is called the continuum hypothesis.

For continuum hypothesis to be valid, the length scale of the fluid element, denoted by  $l$ , should be big enough to contain enough particles, that any random

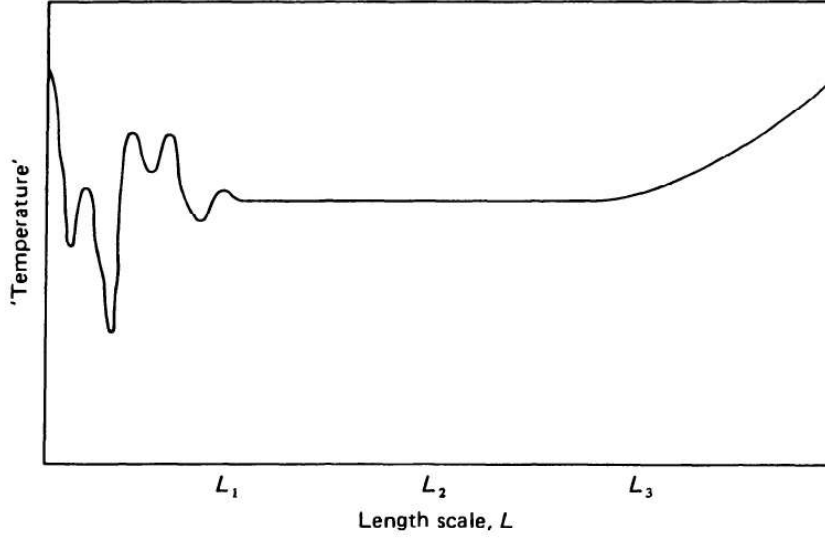


Figure 4.1: Variation of average temperature inside a fluid element with variation of its scale. [3]

variation of the number of particles would be insignificant on any averaged quantity inside the fluid element, so  $l$  should be much bigger than the length scale of a single molecule  $L_1$ . Moreover, the mean free path of the molecules  $\lambda$ , which is the average distance of collision between the molecules, can be much bigger than the size of the molecules, hence the size of the fluid element should also be much larger than the mean free path. On the other hand,  $l$  should be much smaller than the length scale under which any significant macroscopic variations would be felt. This is summarized in Fig. 4.1. In our experiment, if we take the depth of the fluid to be the characteristic length of the flow, so of the order of one centimeter. If we take the fluid element to have a scale length of  $10^{-3}$  cm, so a volume of  $10^{-9} \text{ cm}^3$ , the average number of molecules of water, for example, in such a volume is of the order of  $10^{13}$  molecules. So a fluid element of that size

would satisfy the conditions for the continuum hypothesis.

### The continuity equation

Having discussed the concept of a fluid element, we are able now to apply basic conservation laws on it. We start by applying the conservation of mass. In the absence of sources, the change of the amount of the fluid inside the volume element should be equal to the total flux of elements through the surface of that volume. Put in mathematical form, and accounting for the sign convention in the expression of the flux, the conservation of mass reads:

$$\frac{d}{dt} \int_V \rho dV = - \int_S \rho \vec{u} \cdot d\vec{S} \quad (4.1)$$

$V$  is the volume of the fluid element,  $S$  is the surface enclosing that volume,  $\vec{u}$  is the velocity of the fluid at the position of the element,  $\rho$  is the density of the fluid and the negative sign is to have a decrease in the total density corresponds to a positive outward flux of matter from the volume element.

Employing Leibniz integral rule on the left-hand side of the equation, and Gauss's law on the right hand side and rearranging we get:

$$\int_V \frac{\partial \rho}{\partial t} + \nabla \cdot (\rho \vec{u}) dV = 0 \quad (4.2)$$

and having the volume to be arbitrary, the integrand should be zero, and we get what is called the continuity equation in differential form:

$$\frac{\partial \rho}{\partial t} + \nabla \cdot (\rho \vec{u}) = 0 \quad (4.3)$$

The fluid that we are dealing with in our experiment is incompressible, so its

density is constant and the continuity equation reduces to:

$$\vec{\nabla} \cdot \vec{u} = 0 \tag{4.4}$$

**Conservation of momentum:**

We apply the conservation of energy/momentum to the fluid element, or in other words, second law of motion. To do that let us introduce the concept of a material derivative, which is an operator that considers the changes coming not only from local time variation of a certain quantity, but also from the spatial variation at a set time of the same quantity. Mathematically this operator reads:

$$\frac{D}{Dt} = \frac{\partial}{\partial t} + \vec{u} \cdot \vec{\nabla}. \tag{4.5}$$

The first term on the left-hand side account for the time variation at a specific region of space, while the second term account for the spatial variation at a fixed moment in time.

By applying the material derivative to the momentum, and taking the density to be constant and not varying with time, we have the acceleration field, and hence the left-hand side of Newton's equations, which reads per unit volume:

$$\frac{D(\rho\vec{u})}{Dt} = \rho \frac{D\vec{u}}{Dt} \tag{4.6}$$

The change in the momentum, according to Newton, is equated to the sum of forces applied on the elementary volume. These forces can be divided into body forces and surface forces. The former are forces that act on the bulk of the fluid element like gravity or electric forces in the case of charged fluids, we refer to body forces in our equations as the vector  $\vec{F}$ . The latter are forces that acts on

the surface of the fluid element, they can be divided into forces that are parallel or perpendicular to the normal of the surface.

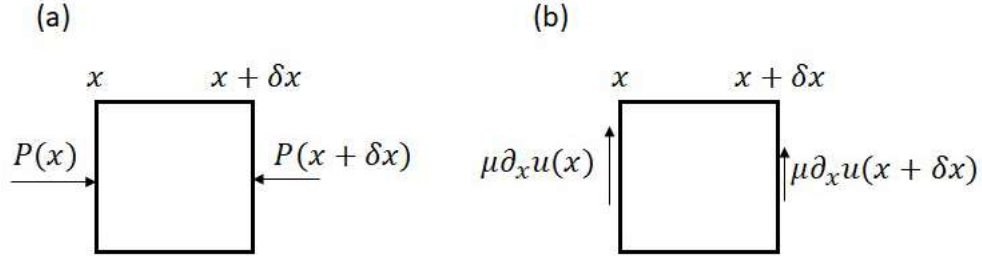


Figure 4.2: (a) pressure forces, (b) viscous forces

The total force exerted by the surrounding fluid on the fluid element is the vector sum of the force on each face of the surface of the element. As shown in Fig. 4.2 (a) the total force in the  $x$  direction parallel to the normal of the surface can be written as:

$$P(x)\delta y\delta z - P(x + \delta x)\delta y\delta z \quad (4.7)$$

Where  $P$  is the force per unit area, or pressure on the surface. Expanding the first term:

$$P(x)\delta y\delta z - \left( P(x) + \frac{\partial P}{\partial x} \delta x \right) \delta y\delta z \Rightarrow -\frac{\partial P}{\partial x} \delta x \delta y\delta z \quad (4.8)$$

Generalizing in all direction the force per unit volume parallel to the surface of the element becomes:

$$-\vec{\nabla} P. \quad (4.9)$$

We account for the shearing between fluid layers. Empirically it was shown that at any location the force per unit area is proportional to the velocity gradient at that location, with a proportionality constant  $\mu$ , what is called the dynamic viscosity of the fluid . Using the same analysis as the pressure forces, we get a

total shear force per unit volume on the fluid element to be:

$$\mu \nabla^2 \vec{u}. \quad (4.10)$$

Putting it all together we get Newton's second law per unit volume written for the fluid element:

$$\rho \frac{D\vec{u}}{Dt} = -\vec{\nabla}P + \mu \nabla^2 \vec{u} + \vec{F} \quad (4.11)$$

dividing everywhere by  $\rho$  we get:

$$\frac{D\vec{u}}{Dt} = -\frac{1}{\rho} \vec{\nabla}P + \nu \nabla^2 \vec{u} + \frac{\vec{F}}{\rho} \quad (4.12)$$

Along with the continuity equation, we get the Navier-Stokes equations fully describing a fluid flow.

Written in a coordinate system that is mostly suitable for the geometry of the problem, the equations are non-linear and do not have an explicit solution yet, to solve them one has to constraint them with simplifying assumptions. Our experimental setup is cylindrical, so the natural coordinate system to be use is cylindrical coordinates. In that coordinate system the fully developed equations read:

**$\hat{r}$ -direction:**

$$\begin{aligned} \frac{\partial V_r}{\partial t} + V_r \frac{\partial V_r}{\partial r} + \frac{V_\theta}{r} \frac{\partial V_r}{\partial \theta} - \frac{V_\theta^2}{r} + V_z \frac{\partial V_r}{\partial z} = -\frac{1}{\rho} \frac{\partial P}{\partial r} \\ + \nu \left[ \frac{1}{r} \frac{\partial}{\partial r} \left( r \frac{\partial V_r}{\partial r} \right) + \frac{1}{r^2} \frac{\partial^2 V_r}{\partial \theta^2} + \frac{\partial^2 V_r}{\partial z^2} - \frac{V_r}{r^2} - \frac{2}{r^2} \frac{\partial V_\theta}{\partial \theta} \right] + F_r \end{aligned}$$

$\hat{\theta}$ -direction:

$$\begin{aligned} \frac{\partial V_\theta}{\partial t} + V_r \frac{\partial V_\theta}{\partial r} + \frac{V_\theta}{r} \frac{\partial V_\theta}{\partial \theta} + \frac{V_\theta V_r}{r} + V_z \frac{\partial V_\theta}{\partial z} = -\frac{1}{\rho} \frac{\partial P}{\partial \theta} \\ + \nu \left[ \frac{1}{r} \frac{\partial}{\partial r} \left( r \frac{\partial V_\theta}{\partial r} \right) + \frac{1}{r^2} \frac{\partial^2 V_\theta}{\partial \theta^2} + \frac{\partial^2 V_\theta}{\partial z^2} - \frac{V_\theta}{r^2} + \frac{2}{r^2} \frac{\partial V_r}{\partial \theta} \right] + F_\theta \end{aligned}$$

$\hat{z}$ -direction:

$$\begin{aligned} \frac{\partial V_z}{\partial t} + V_r \frac{\partial V_z}{\partial r} + \frac{V_\theta}{r} \frac{\partial V_z}{\partial \theta} + V_z \frac{\partial V_z}{\partial z} = -\frac{1}{\rho} \frac{\partial P}{\partial z} \\ + \nu \left[ \frac{1}{r} \frac{\partial}{\partial r} \left( r \frac{\partial V_z}{\partial r} \right) + \frac{1}{r^2} \frac{\partial^2 V_z}{\partial \theta^2} + \frac{\partial^2 V_z}{\partial z^2} \right] + F_z \end{aligned}$$

Continuity:

$$\frac{1}{r} \frac{\partial r V_r}{\partial r} + \frac{1}{r} \frac{\partial V_\theta}{\partial \theta} + \frac{\partial V_z}{\partial z} = 0. \quad (4.13)$$

In our experiment  $\vec{F}$  is the sum of the force of gravity and the lorentz force. The force of gravity is simply  $\vec{g} = (0, 0, g)$ , while the lorentz force is as mentioned above  $F_L = \vec{J} \times \vec{B}$ , where  $\vec{J} = J_0 \exp(-r/\lambda) \hat{r}$  is the current density and  $\vec{B} = (0, 0, B_z)$  is the magnetic field which is taken as constant.

## Boundary conditions

Being a set of second order differential equations in space, and first order in time, integrating the incompressible Navier-Stokes will result in three arbitrary integration constants for each velocity component, that will be fixed by the boundary and initial conditions of the system.

There exist various types of boundary conditions, but we will discuss only those that are relevant to our experiment, namely a rigid impermeable wall.

First the fluid cannot penetrate through the wall, so at the boundary the fluid

velocity  $\vec{v}$  must be the same as the velocity of the wall  $\vec{U}$ . Or in other words:

$$\vec{U} \cdot \hat{n} = \vec{v} \cdot \hat{n} \quad (4.14)$$

Second the fluid velocity just next to the wall must be the same tangentially as that of the wall, so:

$$\vec{U} \times \hat{n} = \vec{v} \times \hat{n} \quad (4.15)$$

## 4.2 Laminar flows at Large Aspect Ratio

We investigate in this section the simplified case of large aspect ratio  $\Gamma$ , since it allows us to do some simplifying assumptions.

At large  $\Gamma$ , as is shown in Chapter 3, the effects of the Ekman layer cannot be ignored. So, the assumptions of the Ekman layer analysis are required. We will not go in depth with the analysis but will state the following. For an Ekman layer one starts off with the assumption that the velocity profiles are only  $z$ -dependent [27], from this we use the continuity equation and the no slip boundary condition to prove that  $V_z = 0$ . For our flow, we cannot assume that we only have  $z$ -dependence, but we can assume that the velocity profiles are only  $r$  and  $z$  dependent with no  $\theta$  dependence due to axisymmetry. Furthermore, since the depth of the fluid is much smaller than the radius of the cylinder, or in other words, the allowed domain of motion in the  $z$ -direction is much smaller than that in the  $r$ -direction, we can assume that  $V_z \ll (V_r, V_\theta)$ , hence we take  $V_z = 0$ . We plug this in the continuity equation written in cylindrical coordinates:

$$\frac{\partial r V_r}{\partial r} = 0 \quad (4.16)$$



Integrating with respect to  $r$ , we get  $rV_r = \text{constant}$ . Since we have the no slip boundary condition, so  $V_r(r = R, z) = 0$ , hence  $V_r = 0$ . In addition, we are interested in the steady state behavior, so we can assume that all quantities are time independent.

So the assumptions can be summarized in:

- $V_z = V_r \simeq 0$
- $\partial_\theta = \partial_t \simeq 0$

plugging these assumptions in the Navier-Stokes in cylindrical coordinates mentioned above, with  $\vec{F}$  as discussed we get:

**r:**

$$\frac{V_\theta^2}{r} = \frac{1}{\rho} \frac{\partial P}{\partial r} \quad (4.17)$$

**$\theta$ :**

$$0 = \nu \left[ \frac{1}{r} \partial_r (r \partial_r V_\theta) + \partial_{z^2} V_\theta - \frac{V_\theta}{r^2} \right] - \frac{1}{\rho} J_0 \exp(-r/\lambda) B_z \quad (4.18)$$

**z:**

$$\frac{\partial P}{\partial z} = -g\rho \quad (4.19)$$

And the continuity is automatically satisfied.

We still have to deal with the  $z$ -dependence of  $V_\theta$  in the  $\theta$  equation. We assume that the variable separates and the velocity can be written as  $V_\theta = V_{\theta 1}(r)V_{\theta 2}(z)$ . Since we are measuring the velocity at the surface of the fluid, and we are assuming that there is no deformation of the surface, we could assume a constant  $z$  for our analysis. So  $V_{\theta 2}(z)$  can be taken to be a constant multiplying  $V_{\theta 1}$ . Now for the term with the second derivative of  $V_{\theta 2}$ , we know from Table 3.1 that the thickness of the Ekman layer is comparable in magnitude to that of the depth of the fluid, and that this thickness is defined as the location at which the velocity is

equal to 0.99 the bulk velocity. From this we could assume that, for all practical purposes, the gradients in the  $z$ - direction are leveling out, and that term can be ignored. What remains is a second order non-homogeneous differential equation that can be solved analytically, its solution can be obtained by first solving the homogeneous equation, and then looking for a particular solution using the Wronskian method. Now the  $z$  equation gives the hydrostatic pressure profile as function of  $z$ , the  $r$  equation gives the  $r$  dependence of the pressure through the  $V_\theta$  profile. So, the only task left is to solve the  $\theta$  equation for the  $V_\theta$  profile as a function of  $r$ .

The solution is found to be:

$$V_\theta = \frac{A}{r} + Cr + \frac{J_0 B_z \lambda^3}{\mu r} \exp(-r/\lambda) + \frac{J_0 B_z \lambda^2}{\mu} \exp(-r/\lambda) \quad (4.20)$$

The parameters that needs to be fixed in this equation are  $A$  and  $C$ , which are the integration constants set by the boundary conditions, and  $J_0$ , the constant in the current density profile, and getting it is a bit trickier. First, we have to relate  $J_0$  to the current that we measure experimentally. We know that  $I = \int \vec{J} \cdot \vec{d}\vec{a}$  with  $\vec{d}\vec{a}$  is unit area perpendicular to the flow of the current. Since the current is purley radial  $da = r d\theta dz$  in cylindrical coordinates. So  $I = J_0 \int r \exp(-(r-a)/\lambda) d\theta dz = J_0 2\pi h r \exp(-r/\lambda)$ . Now to relate this current profile to the one we measure in the experiment,  $\tilde{I}$ , we assume that  $\tilde{I}$  is proportional to the average  $I$  over the radial domain, so we have:  $\tilde{I} = \alpha \frac{\int_{R_i}^{R_o} I dr}{R_o - R_i}$ , with  $R_i$  and  $R_o$  being the inner and outer radii of the container, and  $\alpha$  a proportionality constant that we will use as a fitting parameter. Taking all of that into consideration,  $J_0$  become:

$$J_0 = \frac{\tilde{I}}{2\pi h \alpha \frac{\int_{R_i}^{R_o} r \exp(-r/\lambda) dr}{R_o - R_i}} \quad (4.21)$$

With  $r \in [a, R]$ ,  $a$  being the radius of the inner rod, and  $R$  being the radius of the cylinder.

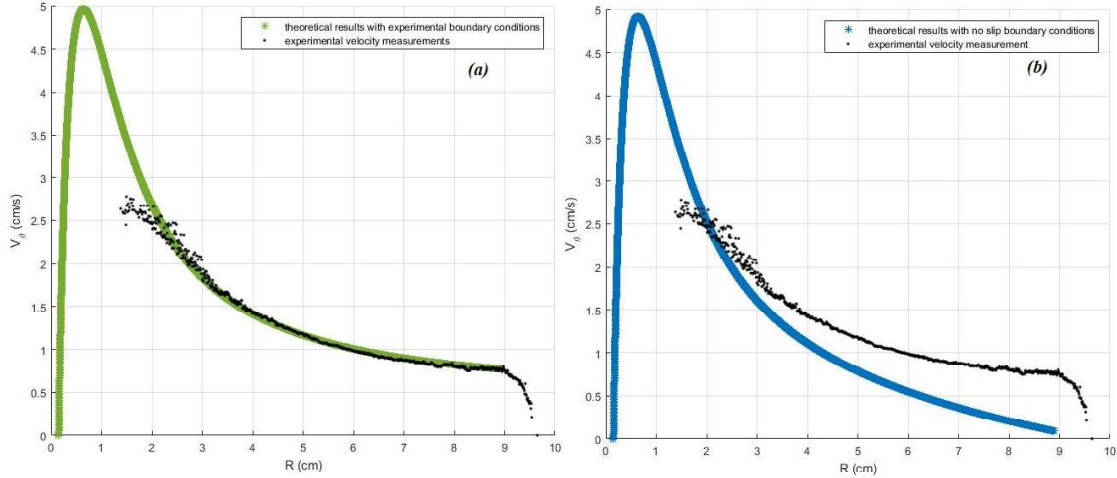


Figure 4.3: Experimental profile for  $V_\theta$  as a function of  $r$  overlaid with the theoretical profile taken the outer boundary condition as (a) experimental value of  $V_\theta$ , (b) no slip boundary condition

It is worth noting that changing the chosen profile of the current density affects the solution drastically. If one assumes that the electrolyte is a perfect conductor and uses a profile that is proportional to  $1/r$ , the agreement between theory and experiment is lost as is shown in Fig. 4.4. This was the drive to look deeper into the theory of electrolysis, which tells us that the electric current is restricted to a boundary layer near the electrodes with a thickness  $\delta$ , this is explained in Chapter 2. Now to get  $A$  and  $B$ , the natural boundary conditions to take are the no slip boundary conditions. Where  $V_\theta(R_i) = V_\theta(R_o) = 0$  with  $R_i$  and  $R_o$  being the inner and outer radius of the cylinder. But comparing this result with the experimental data showed that the two profile does not match as shown in Fig. 4.3 (b). This discrepancy is due to the effect of the boundary layer in the experiment. Our theoretical model does not take into consideration any boundary layer effect on the flow, and to account for it, a boundary layer

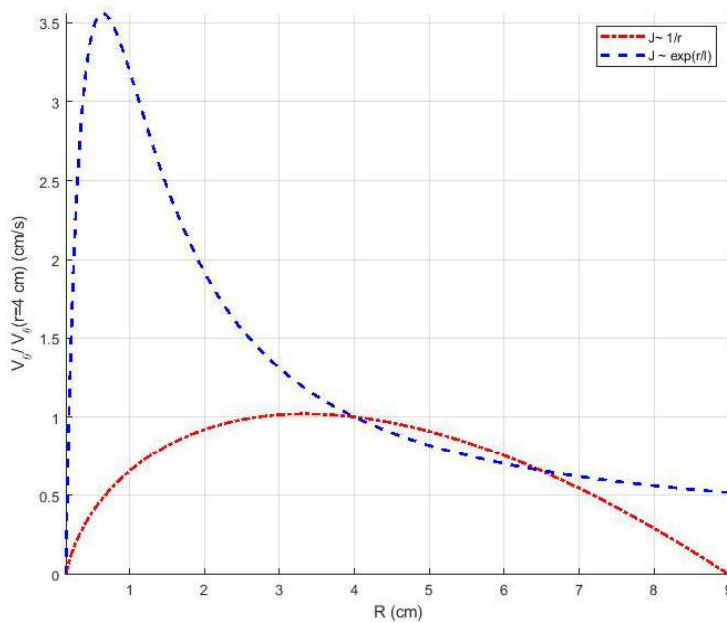


Figure 4.4:  $V_\theta$  vs  $r$  for a current density that is proportional to  $\exp(-(r-a)/\lambda)$  in dashed blue line overlaid with the same plot but for a current density proportional to  $1/r$

analysis has to be made near the outer edge of the cylinder and the resultant velocity profile should be matched with the bulk profile at a point  $\delta$  away from the boundary, with  $\delta$  as before the boundary layer thickness.

The analysis of the boundary layer in cylindrical coordinates turned out to be hairy, so we settled for an experimental value of the velocity at  $R - \delta$ , to fix our integration constants, resulting in a matching profile between the laminar theory and experiment as shown in Fig. 4.3 (b).

### 4.3 The Taylor-Couette instability

The problem of rotating flows between two concentric cylinders was extensively studied. The first to analyze such systems was none other than Newton himself

[5]. Then, many greats followed. The most notable contributions were from two scientists: M. Maurice Couette and Geoffrey Ingram Taylor [5]. The former made use of experiments with a flow between two concentric cylinders to invent one of the earliest viscometers. The latter developed linear stability models for the system taking into consideration the viscosity of the fluid, along with experimental verification of his theory. To develop his viscous theory, G.I. Taylor used the work of Lord Rayleigh, who developed the criterion for linear stability without taking into consideration viscosity, and whose work we are going to elaborate on in this section. For their great contributions, all experiments with concentric cylinders with fluid rotating between them are now called Taylor-Couette flows.

A general experimental setup of the Taylor-Couette (TC) type consists of two rotating concentric cylinders, between which a fluid is immersed. Lord Rayleigh developed the following criterion for the stability of the system disregarding viscous effects:

$$\frac{d(r^2\Omega)^2}{dr} > 0. \quad (4.22)$$

In physical terms, the square of the angular momentum of a fluid element must be a monotonically increasing function of the radius.

In this section, we will recover this criterion, following Lord Rayleigh's analysis [28], and following the proof given by S. Chandrasekhar [21].

First we write the Navier-Stokes equations for an inviscid, incompressible, axisymmetric system with no external forces:

**r:**

$$\frac{\partial V_r}{\partial t} + V_r \frac{\partial V_r}{\partial r} - \frac{V_\theta^2}{r} + V_z \frac{\partial V_r}{\partial z} = -\frac{1}{\rho} \frac{\partial P}{\partial r} \quad (4.23)$$

**$\theta$ :**

$$\frac{\partial V_\theta}{\partial t} + V_r \frac{\partial V_\theta}{\partial r} + \frac{V_\theta V_r}{r} + V_z \frac{\partial V_\theta}{\partial z} = 0 \quad (4.24)$$

**z:**

$$\frac{\partial V_z}{\partial t} + V_r \frac{\partial V_z}{\partial r} + V_z \frac{\partial V_z}{\partial z} = -\frac{1}{\rho} \frac{\partial P}{\partial z} \quad (4.25)$$

**Continuity:**

$$\frac{\partial V_r}{\partial r} + \frac{V_r}{r} + \frac{\partial V_z}{\partial z} = 0 \quad (4.26)$$

The  $\theta$  equation can be rewritten as:

$$\frac{D(rV_\theta)}{Dt} = 0, \quad (4.27)$$

which states that the angular momentum  $L = rV_\theta$ , in the direction of the axis of the cylinder, of a fluid element is conserved.

Let us take two fluid rings of the same height and having the same mass, at the radii  $r_1$  and  $r_2$  such that  $r_2 > r_1$  each with a width of  $dr_1$  and  $dr_2$ . The equality of their masses requires that  $\rho V_1 = \rho V_2$  with  $\rho$  being the density of the fluid. This leads to:  $2\pi r_1 dr_1 = 2\pi r_2 dr_2 = dS$ . On top of that the average kinetic energy of each ring is  $T \sim V_\theta^2 r dr = L^2 / r^2 r dr$ . Now if we interchange the fluid in the rings, since the angular momentum is conserved with the motion of the fluid, each fluid element after the interchange, will retain its angular momentum before the interchange. In other words, the fluid element initially at  $r_1$  and angular momentum  $L_1$  will have angular momentum  $L_1$  when it transits to radius  $r_2$ , and the same thing applies to the second fluid element. Now if calculate the change in the total kinetic energy after the interchange we get

$$\left[ \left( \frac{L_2^2}{r_1^2} + \frac{L_1^2}{r_2^2} \right) - \left( \frac{L_1^2}{r_1^2} + \frac{L_2^2}{r_2^2} \right) \right] dS = \left[ (L_2^2 - L_1^2) \left( \frac{1}{r_1^2} - \frac{1}{r_2^2} \right) \right] dS. \quad (4.28)$$

From this it is clear that when the square of the angular momentum increases outwards, in other words  $L_2 > L_1$ , the system needs an energy input to inter-

change the fluid rings, an indication of stability. On the other hand, when the square of the angular momentum decreases with the radius the system liberates energy with the interchange of the fluid elements, hence the system is unstable.

We derive now the stability criterion using a perturbative approach. Starting with the laminar velocity profile, we perturb the NS equations by assuming that the profiles are  $\vec{V} = \vec{V}_0 + \vec{V}_1$  with  $\vec{V}_0$  the laminar profile, and  $\vec{V}_1$  is a perturbed velocity with amplitude much smaller than the laminar profile. After plugging this in NS equations, and eliminating all terms of order  $V_1^2$  and above, while analyzing an inviscid perturbed system, we get the following equations

**r:**

$$\frac{\partial V_{r1}}{\partial t} - \frac{2V_{\theta 1}V_{\theta 0}}{r} = -\frac{1}{\rho} \frac{\partial P_1}{\partial r} \quad (4.29)$$

**$\theta$ :**

$$\frac{\partial V_{\theta 1}}{\partial t} + \left( \frac{1}{r} \frac{\partial (rV_{\theta 0 1})}{\partial r} \right) V_{r1} = 0 \quad (4.30)$$

**z:**

$$\frac{\partial V_{z1}}{\partial t} = -\frac{1}{\rho} \frac{\partial P_1}{\partial z} \quad (4.31)$$

**continuity:**

$$\frac{1}{r} \frac{\partial (rV_{r1})}{\partial r} + \frac{\partial V_{z1}}{\partial z} = 0 \quad (4.32)$$

To solve these equations, we could assume Fourier modes solutions in the time and  $z$  domains, due to their translational symmetry. In the  $r$  direction we need to solve in real space instead of Fourier space. So, if  $f$  represents any velocity component or pressure in our equations, the general solution would be of the form:

$$f = \tilde{f}(r)e^{-i\omega t + ik_z z} \quad (4.33)$$

Plugging this solution into the above equations we get

**r:**

$$-i\omega\tilde{V}_{r1} - \frac{2V_{\theta0}}{r}\tilde{V}_{\theta1} = -\frac{1}{\rho}\tilde{P}_1, \quad (4.34)$$

**$\theta$ :**

$$-i\omega\tilde{V}_{\theta1} + \left(\frac{1}{r}\frac{\partial(rV_{\theta01})}{\partial r}\right)\tilde{V}_{r1} = 0, \quad (4.35)$$

**z:**

$$-i\omega\tilde{V}_{z1} = -\frac{ik_z}{\rho}\tilde{P}_1, \quad (4.36)$$

**continuity:**

$$\frac{1}{r}\frac{\partial(r\tilde{V}_{r1})}{\partial r} + ik_z\tilde{V}_{z1} = 0. \quad (4.37)$$

Now eliminating  $\tilde{P}_1$  between the  $r$  and the  $z$  equations,  $\tilde{V}_{z1}$  using the continuity equation and  $\tilde{V}_{\theta1}$  using the  $\theta$  equation, we get one differential equation in  $\tilde{V}_{r1}$ . Dropping the tildes, we get:

$$\frac{d}{dr}\left(\frac{1}{r}\frac{d(rV_{r1})}{dr}\right) - k_z^2V_{r1} + \frac{k_z^2}{\omega^2}\left(\frac{2V_{\theta0}}{r^2}\frac{d(rV_{\theta0})}{dr}\right)V_{r1} = 0 \quad (4.38)$$

multiplying the above equation by  $rV_{r1}$  and integrating the first term by parts while assuming that the radial velocity at the boundaries of the cylinder vanishes, we get:

$$-\int \frac{1}{r}\left(\frac{d(rV_{r1})}{dr}\right)^2 dr - \int rK_z^2V_{r1}^2 dr + \int \frac{K_z^2}{\omega^2}\left(\frac{2V_{\theta0}}{r^2}\frac{d(rV_{\theta0})}{dr}\right)rV_{r1}^2 dr = 0 \quad (4.39)$$

rearranging we get:

$$\frac{\omega^2}{K_z^2} = \frac{\int \left(\frac{2V_{\theta0}}{r^2}\frac{d(rV_{\theta0})}{dr}\right)rV_{r1}^2 dr}{\int \frac{1}{r}\left(\frac{d(rV_{r1})}{dr}\right)^2 + rK_z^2V_{r1}^2 dr} \quad (4.40)$$



The ratio  $\frac{\omega^2}{k_z^2}$  is positive only if the integrand of the numerator is positive and negative only if it is negative. And for it to be negative,  $\omega^2$  must be negative, which means that it is a complex number, giving a solution with a positive exponent growing with time, hence the system is unstable. Looking into the integrand of the numerator on the right-hand side we have the following condition for stability:

$$\frac{2V_{\theta 0}}{r^2} \frac{d(rV_{\theta 0})}{dr} > 0 \quad (4.41)$$

putting it in terms of the angular momentum  $L$ :

$$\frac{1}{r^3} \frac{d(L^2)}{dr} > 0 \quad (4.42)$$

This is the Rayleigh criterion initially stated.

Any inviscid, incompressible fluid rotating between two concentric cylinders, admits the above criterion for stability.

## 4.4 Secondary Instability and the Breaking of Axisymmetry

After the primary instability kicks in, an axisymmetric vortex develops in the flow. As mentioned before, the aim of this thesis is to study the transition between this primary axisymmetric state, to the non-axisymmetric state. To do that, we are going to propose a velocity profile that resembles the steady state profile of the axisymmetric flow, and then we are going to apply perturbation theory to explore its stability, with the hope to explore the different destabilizing parameters of the flow.

## Modelling the primary axisymmetric vortices

To get the Rayleigh condition, we perturbed a base flow, and looked for the condition under which that perturbation grows exponentially.

Now to study the stability of the steady state primary flow, we need to get a base flow that describes it, and then perturb it and look for the conditions under which non-axisymmetric perturbations grow. But solving for the steady state primary flow, especially for the full cylinder, while taking into consideration the Lorentz forcing, is difficult. So, we simplify the system in a way that captures the necessary physics. We suspect that the key factor for the breaking of the symmetry in the axisymmetric flow is the shearing layer between the primary vortex, and the bulk flow in the cylinder, on top of that, with the current density profile that we are using there are no significant body forces near the primary vortex that might affect the dynamics. We have to take this into consideration when trying to model the flow in our experiment. So we devise a model that describes two counter rotating vortices constrained in a cylindrical channel of width  $2h$ , with  $h$  being the depth of the fluid in the channel as shown in Fig. 4.5.

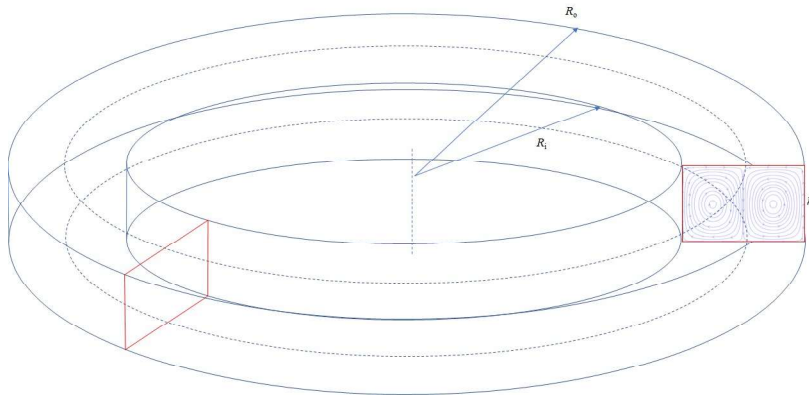


Figure 4.5: Schematics of the modeled cylindrical channel flow

We need a solution that satisfies the steady state, inviscid, incompressible

axisymmetric Navier-Stokes equations.

Starting from a suggestion for the  $V_r$  profile,

$$V_r = \frac{\delta V_r}{\sqrt{r}} \sin(K_r(r-h)) \cos(K_z z) \quad (4.43)$$

This profile is motivated by the solution of Eq. 4.38. This equation is of the Sturm-Liouville type, its solution depends on the profile of  $V_{\theta 0}$ . The  $V_{\theta 0}$  profile shown in equation 4.20 is of the form of  $Ar + \frac{B}{r} + g(r)$ . Solving Eq. 4.38 with this profile for  $V_{\theta 0}$  is extremely difficult. But if we disregard  $g(r)$  it is shown that the solution for  $V_{r1}$  is a linear combination of Bessel functions [21]. Hence, while not capturing the whole dynamics, this solution can be considered as an approximate solution of our system. Furthermore, we are working at the edge of the cylinder having a *large* aspect ratio, we could assume that we are working in the regime where  $r \rightarrow \infty$ . In that regime the Bessel functions can be approximated by  $J_\nu(r) \sim \frac{1}{\sqrt{r}} \cos\left(r - \nu\frac{\pi}{2} - \frac{\pi}{4}\right)$  [29], which verifies the radial part of the suggested  $V_r$  profile. As for the  $z$ -dependence, it is justified by the  $e^{iK_z z}$  dependence in the initial proposed solution in Eq. 4.33. The phases of the sines and cosines are fixed by boundary conditions, and all multiplicative factors are absorbed into  $\delta V_r$ , hence the suggested  $V_r$  profile in equation 4.43 is mathematically justified.

The  $V_z$  profile is obtained by solving the continuity equation of the inviscid, incompressible, axisymmetric, steady state NS equations.

$$V_z = -\frac{1}{r} \int \frac{\partial(rV_r)}{\partial r} dz + C_z \quad (4.44)$$

With  $C_z$  being the integration constant fixed by the boundary conditions.

The only thing that is left to do is to get the  $V_\theta$  profile. One could eliminate the

pressure term between the  $r$  and  $z$  equations and solve for  $V_\theta^2$ . But the resulting profile admits negative values in the domain under study, hence  $V_\theta$  is complex at those regions. Experimentally,  $V_\theta$  profile is almost constant as a function of  $r$  as is shown in Chapter 3, hence one could try a solution for the perturbed equation with  $V_\theta = cst$  and check whether this solution satisfies Eq. 4.23 to 4.26 with the transient term equated to zero.

With  $V_\theta = cst$  these equations reduces to:

**r:**

$$V_r \frac{\partial V_r}{\partial r} - \frac{V_\theta^2}{r} + V_z \frac{\partial V_r}{\partial z} = -\frac{1}{\rho} \frac{\partial P}{\partial r} \quad (4.45)$$

**$\theta$ :**

$$\frac{V_\theta V_r}{r} = 0 \quad (4.46)$$

**z:**

$$V_r \frac{\partial V_z}{\partial r} + V_z \frac{\partial V_z}{\partial z} = -\frac{1}{\rho} \frac{\partial P}{\partial z} \quad (4.47)$$

**Continuity:**

$$\frac{\partial V_r}{\partial r} + \frac{V_r}{r} + \frac{\partial V_z}{\partial z} = 0 \quad (4.48)$$

First the continuity equation is obviously satisfied. As for the momentum balance, the  $\theta$  equations seems not to be satisfied. As for the other two equations, eliminating the pressure between the  $r$  and  $z$  equations we get:

$$\frac{\partial}{\partial z} \left( V_r \frac{\partial V_r}{\partial r} \right) + \frac{\partial}{\partial z} \left( V_z \frac{\partial V_r}{\partial z} \right) - \frac{\partial}{\partial r} \left( V_r \frac{\partial V_z}{\partial r} \right) + \frac{\partial}{\partial r} \left( V_z \frac{\partial V_z}{\partial z} \right) = 0 \quad (4.49)$$

If we plug our profiles for  $V_z$  and  $V_r$  it is not satisfied also. A way out of this is by noting that both the  $\theta$  equation and equation 4.49 have an  $r^{-\alpha}$  with  $\alpha$  being a positive constant. Since we are considering a regime where  $r \rightarrow \infty$ , we

can assume that the proposed velocity profiles satisfy the Navier-Stokes.

Since for  $r \rightarrow \infty$  any circle can be approximated by a straight line, we could verify our assumption above by solving the same problem but for a straight channel, in cartesian coordinates instead of cylindrical. Fig. 4.6 shows a schematic

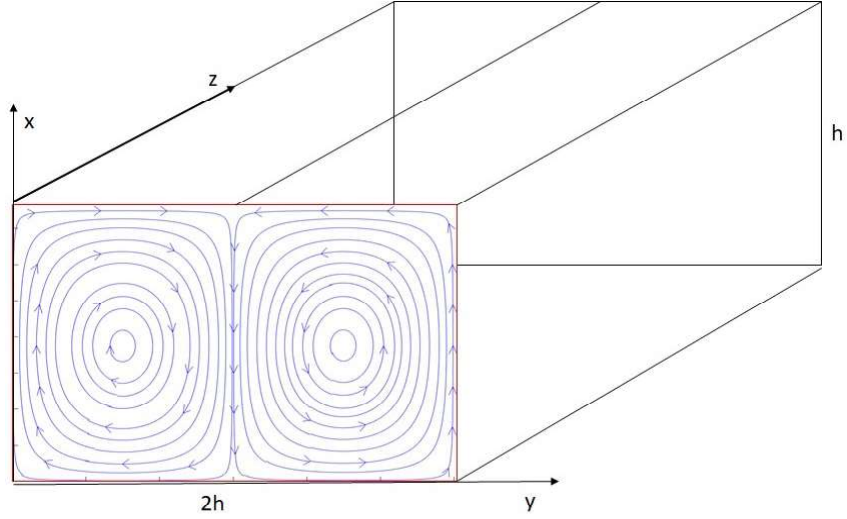


Figure 4.6: Schematics of the modeled cartesian channel flow

of the channel flow geometry with cylindrical coordinates. Now we write the inviscid incompressible steady state NS equations in cartesian coordinates, with all derivatives in the  $z$  direction, equal to zero:

**x:**

$$V_x \frac{\partial V_x}{\partial x} + V_y \frac{\partial V_x}{\partial y} = -\frac{1}{\rho} \frac{\partial P}{\partial x} \quad (4.50)$$

**y:**

$$V_x \frac{\partial V_y}{\partial x} + V_y \frac{\partial V_y}{\partial y} = -\frac{1}{\rho} \frac{\partial P}{\partial y} \quad (4.51)$$

**z:**

$$V_x \frac{\partial V_z}{\partial x} + V_y \frac{\partial V_z}{\partial y} = 0 \quad (4.52)$$

**Continuity:**

$$\frac{\partial V_x}{\partial x} + \frac{\partial V_y}{\partial y} = 0 \quad (4.53)$$

For the initial  $V_x$  profile we expand the  $\frac{1}{\sqrt{r}}$  in the  $V_r$  profile at  $r \rightarrow \infty$  and keep only the first term. We get  $V_x = \delta V_x \sin(K_x(x-h)) \cos(K_y y)$  Then we integrate the continuity to get  $V_y$  and we assume that  $V_z$  is constant. This profile satisfies Eqs. 4.50 to 4.53 exactly, hence the above approximation is valid. And as shown in Fig. 4.7, the proposed velocity profile reproduces the shear layer observed in a TC flow.

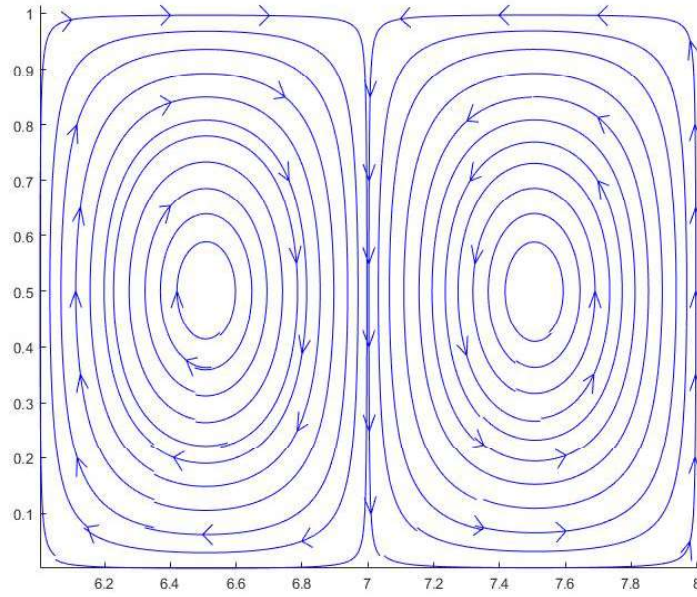


Figure 4.7: Streamlines of the zeroth order profile in normalized units

## Instabilities in the straight open channel flow

Rewriting the zeroth order profile:

$$\begin{cases} V_{x0} = \delta V_x \sin(K_x(x-h)) \cos(K_y y) \\ V_{y0} = \frac{K_x}{K_y} \delta V_x \sin(K_y y) \cos(K_x(x-h)) + cst \\ V_{z0} = cst \end{cases} \quad (4.54)$$

After proving that our profile satisfy Navier-Stokes and simulates the axisymmetric structures formed after the primary instability had set in, it is only logical that we perturb this profile and study its stability with the variation of different parameters.

Although the most insightful thing to do is to perturb the cylindrical base flow, it is also useful to perturb the cartesian base flow and prove that the perturbed equations admit unstable solutions. After that we'll come back to the cylindrical case from which we can explore the effect of different parameters on the stability of the system.

Starting off with the full Navier-Stokes equations in cartesian coordinates, and assuming that the velocity and the pressure are of the form:

$$\vec{V} = \vec{V}_0(x, y) + \vec{V}_1(x, y, z, t) \quad (4.55)$$

$$P = P_0(x, y) + P_1(x, y, z, t) \quad (4.56)$$

With  $V_1 \ll V_0$  and  $P_1 \ll P_0$  are the perturbation. We plug this in the NS equations in cartesian coordinates, while keeping only first order terms. Zeroth order terms already satisfy the equations, and second order terms can be neglected. We get the following set of equations:

**x:**

$$\partial_t V_{x1} + V_{x1} \partial_x V_{x0} + V_{x0} \partial_x V_{x1} + V_{y1} \partial_y V_{x0} + V_{y0} \partial_y V_{x1} + V_{z0} \partial_z V_{x1} = -\frac{1}{\rho} \partial_x P_1 + \nu \nabla^2 V_{x1}, \quad (4.57)$$

**y:**

$$\partial_t V_{y1} + V_{x1} \partial_x V_{y0} + V_{x0} \partial_x V_{y1} + V_{y1} \partial_y V_{y0} + V_{y0} \partial_y V_{y1} + V_{z0} \partial_z V_{y1} = -\frac{1}{\rho} \partial_y P_1 + \nu \nabla^2 V_{y1}, \quad (4.58)$$

**z:**

$$\partial_t V_{z1} + V_{x0} \partial_x V_{z1} + V_{y0} \partial_y V_{z1} + V_{z0} \partial_z V_{z1} = -\frac{1}{\rho} \partial_z P_1 + \nu \nabla^2 V_{z1}, \quad (4.59)$$

**Continuity:**

$$\partial_x V_{x1} + \partial_y V_{y1} + \partial_z V_{z1} = 0, \quad (4.60)$$

with  $\partial_q = \frac{\partial}{\partial q}$  and  $\nabla^2 = \partial_{x^2}^2 + \partial_{y^2}^2 + \partial_{z^2}^2$ .

Now before proceeding, it is always insightful to work with nondimensionalized equations. We normalize our velocity with  $V_{z0}$  the zeroth order velocity in the  $z$  direction, and our position with  $h$  the depth of the fluid, all other parameters will be nondimensionalized by combinations of these two parameters. Hence, we get the following non-dimensional variables:

$$\left\{ \begin{array}{l} X = hX' \\ V = V_{z0}V' \\ t = \frac{h}{V_{z0}}t' \\ P = \rho V_{z0}^2 P' \end{array} \right. \quad (4.61)$$

With  $X', V', t'$  and  $P'$  the non-dimensional space, velocity, time and pressure



respectively.

Plugging these variables into the above equations and rearranging we get:

**x:**

$$\partial_t V_{x1} + V_{x1} \partial_x V_{x0} + V_{x0} \partial_x V_{x1} + V_{y1} \partial_y V_{x0} + V_{y0} \partial_y V_{x1} + V_{z0} \partial_z V_{x1} = -\partial_x P_1 + Re^{-1} \nabla^2 V_{x1}, \quad (4.62)$$

**y:**

$$\partial_t V_{y1} + V_{x1} \partial_x V_{y0} + V_{x0} \partial_x V_{y1} + V_{y1} \partial_y V_{y0} + V_{y0} \partial_y V_{y1} + V_{z0} \partial_z V_{y1} = -\partial_y P_1 + Re^{-1} \nabla^2 V_{y1}, \quad (4.63)$$

**z:**

$$\partial_t V_{z1} + V_{x0} \partial_x V_{z1} + V_{y0} \partial_y V_{z1} + V_{z0} \partial_z V_{z1} = -\partial_z P_1 + Re^{-1} \nabla^2 V_{z1}, \quad (4.64)$$

**Continuity:**

$$\partial_x V_{x1} + \partial_y V_{y1} + \partial_z V_{z1} = 0, \quad (4.65)$$

with  $Re = \frac{hV_{z0}}{\nu}$  the Reynold's number of our system. Along with the non-dimensionalized zeroth order velocity profile:

$$\begin{cases} V_{x0} = \delta V_x \sin(K_x(x-1)) \cos(K_y y) \\ V_{y0} = \frac{K_x}{K_y} \delta V_x \sin(K_y y) \cos(K_x(x-1)) + cst \\ V_{z0} = 1 \end{cases} \quad (4.66)$$

All quantities in the above equations are non-dimensional, and the primes had been dropped for convenience.

To proceed, we assume a plane wave solution for all variables of the form:

$$f = \tilde{f} e^{i(-\omega t + k_x x + k_y y + k_z z)} \quad (4.67)$$

If we replace this solution in the above equations we get a system of linear equations of the form  $A\tilde{f} = 0$ , where:

$$A = \begin{pmatrix} -i\omega + i\vec{k} \cdot \vec{V}_0 + \partial_x V_{x0} - Re^{-1} |\vec{k}|^2 & \partial_y V_{x0} & 0 & ik_x \\ \partial_x V_y & -i\omega + i\vec{k} \cdot \vec{V}_0 + \partial_y V_{y0} - Re^{-1} |\vec{k}|^2 & 0 & ik_y \\ 0 & 0 & -i\omega + i\vec{k} \cdot \vec{V}_0 - Re^{-1} |\vec{k}|^2 & ik_z \\ k_x & k_y & k_z & 0 \end{pmatrix}$$

and

$$\tilde{f} = \begin{pmatrix} \tilde{V}_x \\ \tilde{V}_y \\ \tilde{V}_z \\ \tilde{P} \end{pmatrix}$$

With  $\vec{k} = (k_x, k_y, k_z)$  and  $\vec{V}_0 = (V_{x0}, V_{y0}, 1)$ .

For Eq. 4.67 to be a solution, we have to have  $\det(A) = 0$ . This gives a quadratic equation in  $\omega$ , which admits two complex roots,  $\omega_{1,2} = \omega_{r1,2} + i\gamma_{1,2}$ . To study the stability of the system we have to concern ourselves with the imaginary part of the roots,  $\gamma$ . Whenever  $\gamma$  is negative the solution is exponentially decaying with time, hence the system is stable. On the other hand, whenever it is positive the solution is exponentially growing with time, with a growth rate  $\gamma$ , which means that the system is unstable. We are left now with the task of varying the parameters of  $\gamma$  with which it becomes positive. Those parameters are  $\vec{k}$ ,

$Re$ ,  $\delta V_x$ ,  $x$  and  $y$ , all in normalized units. First  $Re$  and  $\delta V_x$  are set from the experiment, for a height of  $h = 2.5$  cm and  $V_{z0} = 1.73$  cm/s, the Reynold's number is  $Re = 343$  and  $\delta V_x = 0.025/1.73 = 0.014$ . As for  $\vec{k}$ , we assume that the perturbation in the  $x$ -direction has a wavelength of the same order as the width of the channel, so  $\lambda_x \simeq 2h$ , and the perturbation in the  $y$  direction has a wavelength of the same order as the depth of the channel, so  $\lambda_y \simeq h$ . In addition, there is no restriction on the perturbation in the  $z$ -direction, so we are going to assume it has a wavelength of  $\lambda_z = 10h$ . So the normalized wavenumbers are:  $\vec{K} = \left( \frac{2\pi}{2h/h}, \frac{2\pi}{h/h}, \frac{2\pi}{10h/h} \right) = \left( \pi, 2\pi, \frac{\pi}{5} \right)$ .

With the above set of parameters, we obtain that the system is always unstable, with maximum growth rate at the region of shear between the two vortexes as shown in Fig. 4.8.

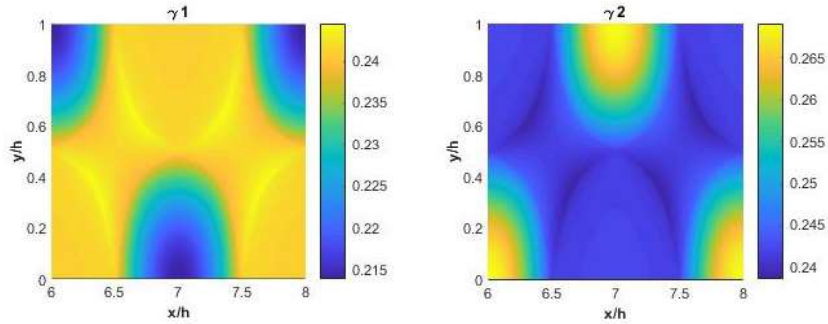


Figure 4.8:  $\gamma_1$  and  $\gamma_2$  plotted as a function of  $x$  and  $y$

We have just shown that the system admits an unstable configuration, with a maximum growth rate of the instability at the shear layer. Now we go to the cylindrical channel case, where we could explore more the dependence of the instability on the different parameters, with the addition of the mode number of the  $\theta$  direction.

## Instabilities in the toroidal open channel flow

Now we repeat the same analysis in the cartesian case to the cylindrical channel case. We start off by normalizing the zeroth order profile by  $V_\theta$ :

$$\begin{cases} V_{r0} = \frac{\delta V_r}{\sqrt{r}} \sin(K_r(r-1)) \cos(K_z z) \\ V_{z0} = \frac{-1}{2K_z r^{3/2}} [\delta V_r \sin(K_z z) (\sin(K_r(r-1))) + 2K_r r \cos(K_r(r-1))] + cst \\ V_{\theta 0} = 1 \end{cases} \quad (4.68)$$

As before we start off with the *normalized* NS equations in cylindrical coordinates, then we assume a solution of the same form as in Eqs. 4.56 and 4.55. We keep the terms of the first order, then we assume Fourier mode solutions for the equations of the form:

$$f = \tilde{f} e^{i(-\omega t + k_r r + m\theta + k_z z)}. \quad (4.69)$$

With that we get a system of linear equations of the form  $A\tilde{f} = 0$ , with

$$A = \begin{pmatrix} -i\omega + i\vec{k} \cdot \vec{V}_0 + \partial_r V_{r0} - Re^{-1} \left( \frac{m}{r} - |\vec{k}|^2 - 1/r^2 \right) & -2/r + (2i(Re)m)/r^2 & \partial_z V_{r0} & ik_r \\ 1/r - (2i(Re)m)/r^2 & -i\omega + i\vec{k} \cdot \vec{V}_0 + V_r/r - Re^{-1} \left( ik_r/r - |\vec{k}|^2 - 1/r^2 \right) & 0 & im/r \\ \partial_r V_{z0} & 0 & -i\omega + i\vec{k} \cdot \vec{V}_0 + \partial_z V_{z0} - Re^{-1} \left( ik_r/r - |\vec{k}|^2 \right) & ik_z \\ 1/r + ik_r & im/r & k_z & 0 \end{pmatrix}$$

and;

$$\tilde{f} = \begin{pmatrix} \tilde{V}_r \\ \tilde{V}_\theta \\ \tilde{V}_z \\ \tilde{P} \end{pmatrix}$$

With  $\vec{k} = (k_r, m, k_z)$  and  $\vec{V}_0 = (V_{r0}, 1, V_{z0})$ .

The procedure continues in the same as in the Cartesian channel case. The determinant of  $A$  is equated to zero, which will lead to a polynomial in  $\omega$  with two complex roots. The sign of the imaginary part of the roots,  $\gamma$  determines the stability of the system, when they are positive the perturbation grows exponentially with time and system is unstable otherwise the perturbation is damped, and the system is stable.

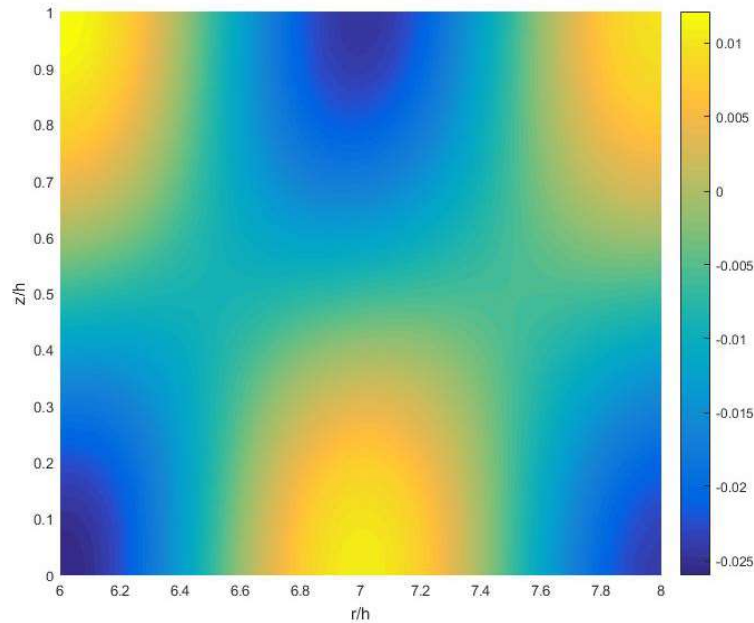


Figure 4.9:  $\gamma$  plotted as a function of  $r$  and  $z$  for  $\lambda_r = 6h$ ,  $\lambda_z = 60h$ ,  $m = 2$ ,  $Re = 205$  and  $\delta V_r/V_\theta = 0.0145$ .

The system admits unstable solutions as shown in Fig. 4.9. It is clear that the shear layer between the two vortices is an unstable region, but the maximum growth rate of the instability is at  $z/h = 1$  and  $r/h = 7$ . This could be explained by noting the following: our velocity profile is periodic in  $r$  and  $z$ , which means

at every half a period there is a shear layer between two vortices as shown in Fig. 4.10 (a). On top of that the zeroth order profile decreases radially outwards proportional to  $\sqrt{r}$ . Which means that the growth rate decreases radially outwards. A quick comparison between Fig. 4.10 (a) and (b) shows that the regions of instability are not only at the shear layer between two vortices, but at the point where the fluid of the vortices diverges from each others. This point will be elaborated on in the conclusion.

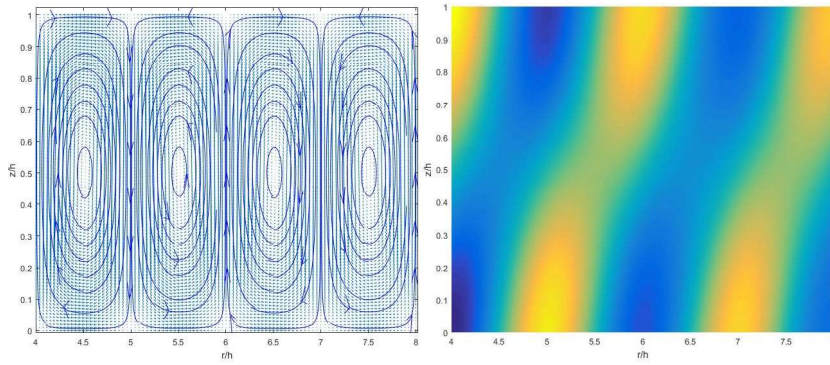


Figure 4.10: (a) periodic zeroth order velocity profile (b) the instability over four vortices

What we can do now, is to explore the parametric dependence of the  $\gamma_s$ . The relevant parameters are:  $\vec{k}$ ,  $Re$ ,  $\delta V_r$ ,  $r$  and  $z$ , all in normalized units.

$r$  and  $z$  are the domain of the channel set in such a way to get two counter rotating vortices for the zeroth order profile. The only mathematical constraint that we have on the remaining parameters is that  $m$  must be an integer so the solution would be single valued in the cylinder, otherwise the parameters are free, making our parameter space infinite. But experimental results put additional constraints that gives us a starting point to probe from. First, we note that we are working in a cylinder of finite radius, hence the perturbation in the  $r$  direction has to have a wavelength less than the radius of the experiment. On

top of that we see experimentally that the vortices of the secondary instability do not come in radial pairs, in other words we don't see two radially adjacent vortices in the  $r - \theta$  plane. From this we could take the width of the channel that we are modeling to be half the wavelength of the perturbation in the radial direction. So  $\lambda_r = 4h$  for a channel of width  $2h$ , which gives  $k_r = 2\pi/(4h)$ , or in normalized unites we get  $k'_r = hk_r = 2\pi/4$ . As for the azimuthal mode number, experimentally it ranged from 2 to 11 depending on the aspect ratio  $\Gamma$ . So, in our model we will take  $m$  varying around that range, from 1 to 15.

From experiment we have  $\delta V_r = 0.025$  cm/s,  $V_\theta = 1.72$  cm/s for  $h = 1.5$  cm. Normalizing  $\delta V_r$  by  $V_\theta$  we get  $\delta V'_r = \delta V_r/V_\theta = 0.014$ .

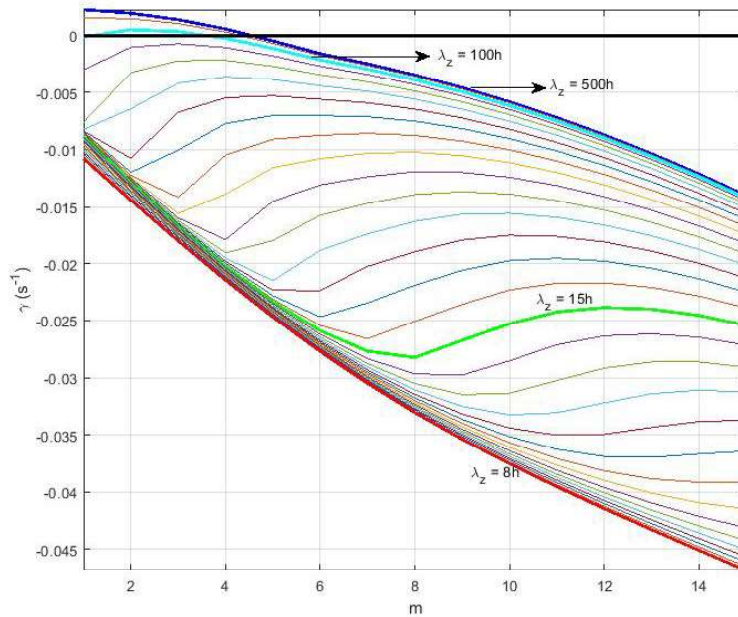


Figure 4.11:  $\gamma$  vs  $m$  for  $\lambda_z$  between  $8h$  and  $500h$  with a logarithmic scale between the  $\lambda_z$ s. Curves with  $\lambda_z = 15h$  and  $100h$  are highlighted to stress on the fact that they are the curves between which the maximum  $\gamma$  point, or the point of highest instability growth rate, varies between  $m = 2$  and  $m = 12$

Obtaining the range of  $K_z$  turned out to be a bit tricky. Fig. 4.11 shows the

variation of the  $\gamma$  vs  $m$  for different  $\lambda_z = 2\pi/k_z$ . Values of  $\lambda_z$  that are smaller or equal to  $15h$  gives a  $\gamma$  that is always negative. On the other hand, values of  $\lambda_z$  that are larger or equal to around  $100h$  have a positive  $\gamma$  at small  $m$  values, and as we increase  $\lambda_z$  no large variation of  $\gamma$  with  $m$  emerges. Based on this analysis and noting that the negative  $\gamma$ s could become positive as we increase the Reynold's number as will be shown below, we could safely limit our range of  $\lambda_z$  to a value between  $15h$  and  $100h$ . It is worth noting that the chosen range shows a variation of maximum  $\gamma$  for  $m$  between 2 and 12 which conforms to the experimental values.

Now we are left with the exploration of the dependence of the  $\gamma$ s on the Reynold's number  $Re = \frac{V_\theta h}{\nu}$ , and on  $\delta V_r$ .

It is tempting to fix one of the two parameters and vary the other independently, but this is not totally insightful. As mentioned before, the flow starts in a laminar state. Under the aforementioned conditions, this base flow becomes unstable to TC instabilities, and a new axisymmetric vortex forms throughout the flow with a periodic radial velocity of the form Eq. 4.43, with amplitude  $\delta V_r$ . The amplitude of the perturbation is correlated to the base flow velocities. We are not going to explore this relation in details, and going to settle for an experimental relation between  $V_\theta$  and  $\delta V_r$ . Experimentally at three currents 60,90, and 120 mA, and for a fluid of depth  $h = 1.5$  cm, or aspect ratio  $\Gamma = 6.4$ , the azimuthal velocity near where the axisymmetric vortex is formed is  $V_\theta = 1.36, 1.734, 2.025$  cm/s respectively. And the amplitude of the radial profile is  $\delta V_r = 0.012, 0.02, 0.025$  cm/s respectively. From these three pair of values, we assume a linear relation and interpolate different combinations of  $V_\theta$  and  $\delta V_r$ .

Fig. 4.12 shows the variation of the  $\gamma$  vs  $m$  curve at different Reynold's numbers and at different aspect ratios  $\Gamma$ . From this figure we can note two



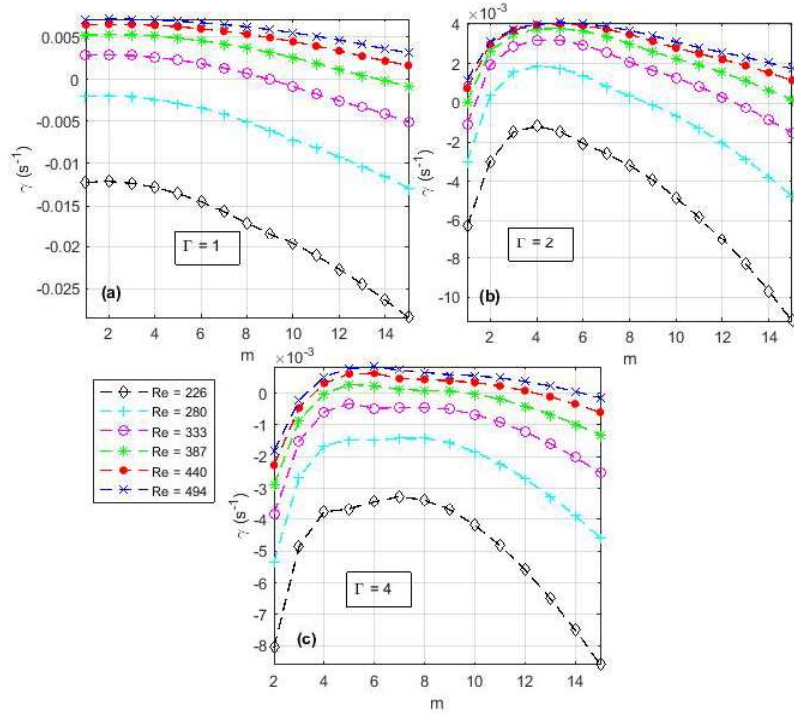


Figure 4.12:  $\gamma$  (1/s) vs  $m$  for different Reynold's numbers taken at  $h = 1.5$  cm with  $K_z = \pi/25$   $K_r = \pi i/(2 \times \text{width of the channel})$  in normalized units, (a) for aspect ratio  $\Gamma = 1$  and with a maximum  $\gamma$  at  $m_{max} = 2$  for all Reynold's numbers, (b) for aspect ratio  $\Gamma = 2$  and with a maximum  $\gamma$  at  $m_{max}$  between 4 and 5, (c) for aspect ratio  $\Gamma = 4$  and with a maximum  $\gamma$  at  $m_{max}$  between 5 and 7

things: The first is that for a constant  $\Gamma$  an increase in the Reynold's number would make the system more and more unstable, but without largely affecting the mode number at which the instability has a maximum growth rate  $m_{max}$ . Second as we increase  $\Gamma$  we can also see that  $m_{max}$  also increases. Both of those findings are confirmed by the experimental results that are presented in Chapter 3.

## 4.5 Conclusion

In this section we have proven that an axisymmetric flow can naturally transit into nonaxisymmetric with the virtue of a secondary instability, mediated by a shear layer between the two vortices of the flow, and under specific values of the flow parameters. We have also found a relation between the Reynold's number and the stability of the flow, and that when the flow is unstable, the number of non-axisymmetric vortices is related to  $\Gamma$ , the aspect ratio of the flow. The analysis of this section is of course linear in nature, so it does not replicate totally the experimental findings, but it gives insight on the controlling parameters and replicate key features of the instability.

# Chapter 5

## Conclusions and Future works

In this thesis we presented a novel experiment, in which a non-axisymmetric instability emerged on top of a primary axisymmetric instability. Novel in the sense that the development of the secondary instability was natural and without the forcing of a shear layer in the  $r - \theta$  plane. We showed both experimentally and theoretically that the source of the instability was indeed a shear layer, but counter to the previous literature it was in the  $r - z$  plane and not in the  $r - \theta$  plane. We characterized the relevant non-dimensional parameters controlling the dynamics of the flow and showed the effects of both the Reynold's number and the aspect ratio  $\Gamma$  on the properties of the flow.

More work can be done to develop both the experiment and the theory. First in terms of the experimental setup one can use a higher resolution camera with a higher frame rate, which would increase the accuracy of the experiment, and guarantee that  $\delta V_\theta$  measured is coming solely from the intrinsic fluctuations of  $V_\theta$ . The analysis code can be developed more to filter out erroneous vectors with a post processing scheme. In terms of the experimental results one could probe for the variation of the mode number with the aspect ratio, along with

the characterization of the growth rate of the instability at different Reynold's numbers. Finally, theoretically one could probe the parameter space gotten in a more in depth way, to better understand the nature of the perturbation and its effect on the flow.

# Appendices

# Appendix A

Submitted paper

# On the Onset of Non-Axisymmetric Instability in Shallow Rotating Flows

G. Antar, A. Lalti and C. Habchi \*

*American University of Beirut, Riad el-Solh, Beirut 1107-2020, Lebanon*

*\* Notre Dame University - Louaize, Zouk Mosbeh 1200, Lebanon*

(Dated: May 8, 2018)

## Abstract

Using experimental, theoretical and numerical techniques, we show that the axial symmetry of shallow rotating flow is naturally broken in the absence of externally forced gradient. We present evidence that this is caused by a secondary instability, which comes as a consequence of the gradients generated by the primary instability. The experiment consists of an electrolyte poured into a cylindrical container with radius  $R$  and height  $h$ . It is subject to electromagnetic forcing caused by an axial magnetic field and a radial current ( $J$ ). At large aspect ratio ( $R/h$ ) and low Reynolds number ( $Re$ ), the flow is laminar. At moderate aspect ratio, the flow is subject to the Taylor-Couette (TC) instability in the boundary layer generating an axisymmetric vortex in agreement with the theory. When  $Re$  is increased by changing  $h$  or  $J$ , the flow becomes unstable, at a critical Reynolds number about 260, leading to a secondary instability excited at the radial position where gradients exist due to the primary vortices. The experimental work is confirmed using theoretical calculation as we perform non-axisymmetric perturbation of two counter-rotating vortices moving in a toroidal channel. It is shown that a non-axisymmetric instability is expected to grow at the location between the two vortices under conditions close to our experiment. Direct numerical simulation is conducted and the results confirm the onset the axisymmetric vortex near the wall as well as the non-axisymmetric structures generated at the shear of the primary vortices. It is concluded that the breaking of the symmetry in shallow rotating flows take place at relatively low Reynolds numbers caused by the dynamics of the primary instability.

PACS numbers: 47.20.Lz,47.20.Qr,47.32.Ef,97.10.Gz,96.30.Mh

Keywords: Shallow rotating flow, Taylor-Couette instability, secondary instability, accretion disk

## I. INTRODUCTION

Rotating flows are found in nature and in man-made devices, they are thus ubiquitous to different fields of Physics and Engineering [1]. The domains of application span over a wide range of scales, from simple household equipment like vacuum cleaners to jet engines and magnetized thermonuclear plasmas (tokamaks) [2]. They also occur at scales of natural geophysical flows like hurricanes and polar structures [3], reaching protoplanetary disks around newly formed suns up to accretion disks around black holes [4]. The common feature to all of these themes is the rotation of a neutral or ionized fluid around an axis with a height much smaller than the radius. The understanding of these flows, their stability and turbulence remains up-to-date an active field of research with major consequences to improve our techniques and enhance our understanding of the universe.

Rotating flows were studied theoretically and experimentally by many authors where the fluid motion is produced by rotating walls leading to the so-called Taylor-Couette (TC) flows [5]. Their stability with respect to axisymmetric disturbances is determined by the Rayleigh criterion, indicating that it is unstable whenever  $\partial_r(r^2\Omega)^2 < 0$ , where  $\Omega$  being the angular velocity of the fluid [5–7]. The instability leads to Taylor vortices, which are axisymmetric occurring in the radial-height plane. The Rayleigh criterion was later on extended to three-dimensional perturbations and it was shown that it is generic regardless of the distortion from circular motion [8]. Its generalization to include centrifugal non-axisymmetric instabilities was done in Refs. [9, 10].

On the other hand, the study of accretion disks around black holes posed a contradiction. On one hand, the theory of Lord Rayleigh [11] indicates that Kepler-like profiles are stable whereas observations hint towards turbulent dynamics. This problem was understood by considering the magnetohydrodynamic equations applied to a compressible fluid subject to magnetic field perturbations. Accordingly, while astrophysical accretion disks with a Keplerian-like velocity profile are hydrodynamically stable, they are unstable to the magneto-rotational instability (MRI) [12–14]. The criterion of instability is  $\partial_r\Omega < 0$  and like the TC instability, MRI leads to the onset of axisymmetric vortices in the radial-height plane.

There is a consensus that we have a rather good understanding of axisymmetric perturbations and instabilities in rotating flows. Among the questions that persist are the symmetry breaking and the road to three-dimensional turbulence. Understanding how the axisymmetry is broken is crucial because the momentum is mainly in the azimuthal direction,



consequently, its perturbation should strongly affect the flow rotation as well as its mixing properties. Driven by the various applications, several experimental setups were designed to study the onset of non-axisymmetric instabilities in rotating flows. We divide them into two large groups, barotropic where the flow is essentially two-dimensional without gradients in the axial direction, baroclinic flow where gradient in the axial direction are important.

The onset of non-axisymmetric perturbations in barotropic flows was investigated by many groups, we recommend the following review articles and the references therein [15–17]. The experiments consist of a closed container that is filled with a fluid and set in motion by rotating top and bottom walls moving at the same speeds. A shear zone is achieved in the radial direction by dividing the top and bottom plates into two differentially rotating disks leading to an inflexion in the velocity profile at the so-called Stewartson layer [18, 19]. Using soap films with aspect ratio  $\Gamma = R/h = 20$ , where  $h$  is the height and  $R$  is the outer radius of the fluid, non-axisymmetric structures were excited at the radial position of the azimuthal velocity shear layer [20] at a critical Reynolds number, defined as  $Re_c = |\Delta\Omega|Rh/\nu$ , about 85-110;  $\Delta\Omega$  is the differential rotation of the two disks and  $\nu$  is the kinematic viscosity. The azimuthal mode number,  $m$ , is found to be inversely proportional to  $h$  and the Reynolds number. Chomaz *et al.* [21] performed a comparison between the experiment and numerical simulations using a similar setup with aspect ratios between 8 and 13.3 and found excellent agreement between the two techniques. The work in Ref. [22] with  $\Gamma = 2.5$  showed that the Reynolds number, with the characteristic length that includes the Ekman number and the depth of the fluid, is the appropriate dimensionless quantity that best describes the onset of non-axisymmetric instabilities. Good agreement was obtained between the linear theory and the experiment especially concerning the critical Reynolds number for the onset of the non-axisymmetric instability. Furthermore,  $m$  is also found to decrease with increasing Reynolds number. The apparatus used in Refs. [23, 24] is larger than those used previously with  $\Gamma = 1.5$ . Their study provided evidence that the nature of the transition is a supercritical instability through a Hopf bifurcation and suggested further evidence in support of the validity of the quasi-geostrophic approximation made in Ref. [22]. The hexagonal structure found in the north pole of Saturn motivated further work using similar setups. With  $\Gamma = 20$ , the authors in Ref. [25] studied the onset of non-axisymmetric vortices as a function of the Ekman and the Rossby numbers in a closed toroidal channel with differentially moving top and bottom walls. Non-axisymmetric vortices are reported to be caused by the unstable zonal jets and thus provided one possible explanation to the North

Pole structure on Saturn. On this topic, one can add the work on vortices and Rossby waves in Ref. [26] where the interaction between vortices generated by small jets and rotation were studied in great detail.

Baroclinic experiments are performed in closed annuli with the top or/and bottom walls rotating at different angular velocities leading to a velocity gradient in the axial direction. Other ways to produce axial dependence could be the use of temperature or density gradients in rotating flows [27–29]. Hydrodynamic instabilities in closed channels using forced differential rotation in the axial direction were done to help understanding motion in planet’s atmosphere where the motion generated by the temperature gradient between the poles and the equator is coupled to the planet rotation [30–32]. In Ref. [33], the authors use both numerical and experimental technique to investigate the instability in differentially driven rotating cylinder with an aspect ratio of 2. The three-dimensional structures were visualized showing non-axisymmetric structures different from the barotropic case as they include a gradient in the axial direction. Similar results were obtained in Ref. [34] with  $\Gamma = 2 - 20$  where it was shown that the shear layer instability is the main responsible for the patterns formation whereas the boundary layer remained stable. The results could be explained by classical Kelvin-Helmholtz instability with a negligible role of the curvature. The critical Reynolds number, with scale based on the shear layer thickness, is found to be about 110 in agreement with previous work and confirming that the transition originates from a shear layer instability.

The work on rotor-stator cavity [32, 35, 36] combines axial and radial gradients as one disk inside a closed cylinder rotates. The studies are performed at large Reynolds numbers and showed the onset of elongated non-axisymmetric structures using experiment and numerical simulation. Unlike the experiments discussed above, the onset of three-dimensional motion occurs with elongated structures in the azimuthal direction and restricted in the radial direction.

Free surface shallow rotating flows with electromagnetic forcing applied to electrolytes were studied in annular channels [37–39]. The direction of the magnetic field was chosen to change in the middle of the flow leading to a radial gradient in the azimuthal velocity as the fluid is the subject to the Lorentz force. At the shear layer, the onset of non-axisymmetric vortices was reported and the results are quite similar to those achieved by in barotropic experiments with rotating walls. The theory of electromagnetically driven flow of electrolyte in a thin annulus layer was lately revisited in Ref. [40].

The main issue addressed in this article, which complements the above research on shallow rotating flows, is the possibility to break the axial symmetry in the absence of externally imposed gradient. Our experimental setup possesses the following characteristics: The walls of the setup are all steady and only the fluid is rotating caused by the Lorentz force. Our flow is an open toroidal channel flow with an inner radius that is 50 times smaller than the outer radius. No gradient in the temperature, the density or the velocity are enforced on the system. The only velocity gradient is that generated at the walls in the boundary layer. The magnetic field is along the same direction, consequently, the flow rotates in the same direction at all radii. The aspect ratio can be varied easily, it will have values here between 4 and 33. We confirm that non-axisymmetric vortices are excited by a secondary instability at the radial position where gradients exist caused by the primary instability. The fact that primary instabilities occur in most of rotating flows makes our study relevant to most of the themes discussed above and in particular to rotating flows occurring in Nature.

This paper continues with the description of the experimental apparatus and the diagnostics used in section II. In section III, we discuss the laminar motion at high aspect ratio. We show that the flow is laminar and good agreement is obtained with the theory considering the fluid used is an electrolyte. In section IV, the primary instability at the boundary layer is discussed with the onset of axisymmetric Taylor vortices in the radial-height plane. Also, good agreement is found with the theory of linear stability reflected in the Rayleigh criterion. The breaking of the axisymmetry is done in two ways: First, we increase the Reynolds number and keep the aspect ratio unchanged, this is done in section V. Second, we decrease the aspect ratio of the flow and this is discussed in section VI. It is shown that the number of vortices in the azimuthal plane decreases with decreasing aspect ratio. With increasing Reynolds number, the growth rate increases, so the onset of secondary vortices occurs faster. In section VII, we use the perturbation method to investigate the linear stability of two counter-rotating vortices rotating azimuthally in a toroidal channel. We find that the flow is expected to be unstable with a mode number and a Reynolds number that are close to those found in the experiment. In section VIII, we present results from direct numerical simulation as it is performed using the finite volume discretization method. The results are in excellent agreement with the experiment showing that indeed the flow symmetry is broken at the velocity shear layer generated by the primary instability. We conclude by affirming the excellent agreement among the three methods used in this paper, that are, experimental, theoretical and numerical and by discussing the possible consequences in three

different fields of our study as a prelude to future work.

## II. THE EXPERIMENTAL SETUP

The experimental setup used to investigate instabilities in shallow rotating flows is illustrated in Fig. 1. It consists of a Plexiglas non-conducting cylinder with a thin stainless-steel sheet fixed on its inner wall making its radius  $R = 9.65$  cm. At its center, we install a stainless-steel rod of radius  $a = 0.125$  cm. We pour a potassium hydroxide (KOH) solution with heights chosen in this paper to be  $h = 0.3, 1.5$  and  $2.5$  cm leading to aspect ratios  $\Gamma = R/h = 33, 7$  and  $4$  respectively. The concentration of KOH is about 25% of the weight, which leads to the electrical conductivity to be  $\sigma = 55$  S/m, the density equals to  $1.24$  kg/m<sup>3</sup> and the kinematic viscosity about  $1.25 \times 10^{-6}$  m<sup>2</sup>s<sup>-1</sup>.

The inner rod is biased with respect to the outer cylindrical sheet drawing a total current  $I_M$ , which we vary here between 60 and 120 mA. With these currents, one can verify that the electrolyte remains at room temperature during the experiment, which lasts about a minute. Around the cylinder, a set of electromagnets generates an axial magnetic field at the edge of  $B = 90$  mT, which decreases towards the center to 50 mT. The Lorentz force,  $\vec{J} \times \vec{B}$ , where  $\vec{J}$  is the current density, leads to the motion in the azimuthal direction.

We obtain qualitative information about the flow motion by injecting a minute quantity of premixed fluorescent dye with the KOH solution at chosen positions and follow the spread of the dye as it is entrained by the fluid motion.

Quantitative data is obtained by using  $200 \mu\text{m}$  beads with a density smaller than water that are scattered on the surface of the electrolyte and let to move with the fluid. They thus float on the surface absorbing in the ultraviolet (UV) and emitting in the green. Two UV lamps installed above the container provide the necessary light intensity. We image the flow with a 12-bit  $2600 \times 1290$  pixels camera installed vertically at about 50 cm from the container and recording at a rate of  $f_r = 1/\Delta t = 15$  frames/second. The spatial resolution is dominated by the beads size since in one direction one pixel covers  $77 \mu\text{m}$  and in the other  $150 \mu\text{m}$ . The azimuthal velocity is obtained by following all the beads over three consecutive frames in an Eulerian fashion. It is calculated using a central difference scheme leading to  $V_{\theta,i} = (\theta_i(t + 2\Delta t) - \theta_i(t))/2\Delta t$  where  $\theta_i$  is the azimuthal position of the bead  $i$  determined at two frames separated by  $2\Delta t$ . The minimum velocity that we can resolve is  $1.5$  mm/s. To minimize the account of false neighbors, we impose a maximum angle of  $\theta_{max} = 15^\circ$  between the motion occurring in the frames  $(i, i + 1)$  and the one in  $(i + 1, i + 2)$ . This can be

interpreted as putting a condition on the vorticity over the velocity shear rate to be smaller than  $\cot 2\theta_{max}$ . The radial velocity order of magnitude is about 1/100 times that of the azimuthal velocity, consequently, we are unable to resolve it using the Eulerian method. We thus developed a Lagrangean method according to which we follow one bead motion in time. If we are able to track it for more than one full turn, then, we determine the radial velocity by determining the change in the radial position according to  $V_r(t) = (r_i(t_0 + t) - r_i(t_0))/t$ . The radial position of the bead  $i$  is  $r_i$ ,  $t_0$  is the time when we start following the bead and  $t$  is the time if the first full rotation is complete. For the radial velocity calculation, and since it requires tracking over a long period of time dedicated experiments were performed where a limited number of fluorescent beads are puffed on the fluid before starting tracking them.

In Table I, we insert the experimental parameters of the flow as well as dimensionless parameters that are relevant to our study. We use the so called external Reynolds number [23] defined as  $Re = V_\theta(r = 8)h/\nu$  to characterize the fluid dynamics. Since the secondary instability that leads to the onset of non-axisymmetric structures occurs at around  $R - h$ , the  $V_\theta$  used in the determination of the Reynolds number is at  $r = 8$  cm. The relative importance of the shear layer caused by rotation to the presence of friction with the bottom and the sides, is assessed using the Ekman number  $E_k = \nu/\Omega h^2$ . With  $\Omega = V_\theta(r)/r$  taken at  $r = 8$  cm,  $E_k$  varies from 1.2 to  $8 \times 10^{-3}$  indicating that the vertical friction plays minor role for when studying the onset of the instabilities at low aspect ratios. The thickness of the Ekman layer  $\delta = \sqrt{\nu/\Omega}$  is about 2-3 mm. It reflects the region where the flow velocity changes from the maximum at the surface of the fluid to 0 at the bottom and side walls. As no gradient is imposed in the axial direction, the flow far from the walls is considered barotropic for moderate to low aspect ratio. Actually, this is supported by the shape of our non-axisymmetry vortices, which appears to be similar to those generated in barotropic flows [21, 22] and far from those generated in baroclinic flows [33].

### III. LAMINAR FLOW DYNAMICS AT LARGE ASPECT RATIO

We study the dynamics of shallow rotating flow by filling the container with the electrolyte solution to  $h = h_0 = 0.3$  cm. This leads to a large aspect ratio  $\Gamma \simeq 33$  and a small Reynolds number ranging about 46. The main goal of this section is to study the laminar motion of the flow. We show that the best fit of the experimental data corresponds to an exponentially decreasing current with increasing radius in agreement with the studies of the Debye shielding in electrolytes in the presence of convection.

$h$ [cm]	$I_M$ [mA]	$V_\theta(r = 8)$ [cm/s]	$Re$	$E_k$	$\delta$ [mm]
0.3	60	0.9	22	1.2	3.3
0.3	90	1.4	32	0.8	2.7
0.3	120	1.9	46	0.6	2.3
1.5	60	1.3	156	$34 \times 10^{-3}$	2.8
1.5	90	1.6	192	$28 \times 10^{-3}$	2.5
1.5	120	1.9	228	$23 \times 10^{-3}$	2.3
2.5	60	1.2	240	$13 \times 10^{-3}$	2.9
2.5	90	1.6	350	$9 \times 10^{-3}$	2.4
2.5	120	1.9	380	$8 \times 10^{-3}$	2.3

TABLE I: Table presenting the main parameters of the experiment.

Using the data taken of the fluorescent beads as they move around the container, the profile of the instantaneous azimuthal velocity,  $v_\theta$ , for  $Re = 46$  is plotted in Fig. 2(a) in dots along with the average azimuthal velocity normalized by the average value at  $r = 4$  cm, that is,  $V_\theta(r = 4)$ . The average velocity profile is obtained by averaging first over the azimuthal angle, then over time.

At this aspect ratio,  $\Gamma = 33$ , the value of  $V_\theta(r = 4)$  increases linearly with the total current, it varies from 0.9 to 1.9 cm/s when  $I_M$  is increased from 60 to 120 mA. An image of the container taken 30 seconds after the dye was injected close to the center is shown in Fig. 2(b). The dye moved towards the outer edge as a result of the centripetal force and maintained a circular edge between parts of the flow with and without dye reflecting the absence of non-axisymmetric vortices. The laminar motion can also be deduced from the beads motion over time. This is shown in Fig. 2(b) where we overlaid the light signals coming from three beads as a function of time. Their motion at the three radii is circular indicating the absence of non-axisymmetric structures. From Fig. 2(a), we infer that  $V_\theta$  decreases exponentially as a function of  $r$ . Consequently, the radial velocity, caused by the centripetal acceleration, decreases even faster. The decrease of the radial velocity with  $r$  is detected in Fig. 2(b) showing that the bead closest to the center has strong radial velocity, which decreases with increasing  $r$  and becomes almost zero for the farthest bead. The ratio  $V_r/V_\theta$  in the bulk is found to be about 1/100.

To simulate the profile of  $V_\theta$ , we consider a rather simple two-dimensional model with

the axial velocity,  $V_z$ , and  $\partial_z$  are equal to 0. Moreover, the radial velocity is assumed to be negligible when compared to  $V_\theta$ . Since, we are interested in the laminar axisymmetric motion, we take no dependence on the azimuthal angle, therefore  $\partial_\theta = 0$ . Applying the above assumptions to the incompressible Navier-Stokes equations, we obtain the following equation

$$\frac{\partial^2 V_\theta}{\partial r^2} + \frac{1}{r} \frac{V_\theta}{\partial r} - \frac{V_\theta}{r^2} = -\frac{\rho J(r) B}{\nu}, \quad (1)$$

where  $\rho$  is the density of the electrolyte,  $J$  is the current density and  $B$  is the magnetic field. The equation of  $V_\theta$  is solved with the two boundary conditions,  $V_\theta(r = a) = 0$  and  $\partial_r V_\theta(r = R) = 0$ . The condition at  $R$  reflects the fact that the boundary layer physics at the outer wall is not included. We take the magnetic field to be uniform. By using permanent ring magnets instead of electromagnets, it is verified that its radial dependence does not change at all the experimental results.

The current density in electrolytes takes the form  $J(r) = J_0 \exp -(r - a)/\lambda$  with  $\lambda = 1$  mm.

Excellent agreement is obtained between the solution of the above equation and the experiment as one can deduce from Fig. 2(a). Concerning the decay length  $\lambda$ , it is known that for motionless electrolytes that  $\lambda$  is of the order of a nanometer reflecting the Debye scale of an electric double layer [41]. When the electrolyte is in motion,  $\lambda$  takes values of the order of a millimeter reflecting in this case the diffusion layer thickness [42–44]. The quantity  $J_0$  is determined from the condition  $\int_a^R J(r) h 2\pi dr = I_M$ , where  $I_M$  is the total current measured in our experiment. Consequently, the Lorentz force drive is concentrated near the center of the container and the rest of the flow rotates due to viscosity in the absence of a radial velocity.

We deduce that excellent agreement is obtained between the theory of two dimensional motion and the experiment for the laminar case with an exponentially decreasing current density that has a decay length scale consistent with the thickness of a diffusion layer in electrolytes.

#### IV. PRIMARY INSTABILITY AT MODERATE ASPECT RATIO

We increase the height of the fluid to  $h_1 = 1.5$  cm ( $\Gamma = 6.7$ ) to examine its role in affecting the two-dimensional laminar rotational motion detected at  $h_0$ . We show that at

small Reynolds numbers there exist a boundary layer instability caused by the azimuthal velocity at the outer edge leading to the onset of a TC vortex. As we increase the current, and thus the Reynolds number, non-axisymmetric vortices appear at the shear layer caused by the velocity gradients of the axisymmetric structures.

In Fig. 4(a), we plot the instantaneous ( $v_\theta$ ) and the time averaged azimuthal velocity ( $V_\theta$ ) obtained one minute after the current is switched on. The average rotation properties at  $h_1$  are different from those at  $h_0$ . The rotation speed, represented by  $V_\theta(r=4)$  increases from 1.3 to 1.9 cm/s, that is by only 50%, as the current is doubled  $60 \rightarrow 120$  mA, whereas, it doubled for  $h_0$  for the same current increase. The shape of  $V_\theta$  changes drastically from an exponential decay *vs*  $r$  at  $h_0$  to rather flat in the region  $1.5 < r < 8$  cm at  $h_1$ .

At the outer edge, the azimuthal velocity decreases to 0 starting from  $r = r_1 = R - h_1 \simeq 8$  cm reflecting an important increase in the boundary layer thickness from 2 mm the value for  $h_0$ . This large boundary layer is caused by the onset of an axisymmetric vortex with diameter equals to  $h_1$ . Because of the flat  $V_\theta$  profile, the gradient at the boundary layer near the outer wall increases. The flow thus becomes unstable to the Taylor-Couette instability. In fact, the investigation of the Rayleigh criterion, presented in Fig. 4(b), confirms that indeed  $\partial_r(rV_\theta)^2$  is negative for  $r \geq r_1$ . Consequently, the flow is TC unstable at the outer boundary leading to the formation of an axisymmetric Taylor vortex as expected from the theory.

The onset of this instability naturally increases the fluctuations of  $v_\theta$ . This is quantified using the standard deviation, defined as  $\delta V_\theta = \sqrt{\langle (v_\theta - V_\theta)^2 \rangle}$  where  $\langle \rangle$  denotes the average over the azimuthal angle and time. The result is plotted in Fig. 4(c) where the maximum of  $\delta V_\theta$  takes place at  $r \simeq 9$  cm where  $V_\theta$  gradient is the highest indicating that this increase is caused by the TC instability.

We confirm the existence of the axisymmetric vortex using dye injected close to the container outer edge at  $r \sim 9.5$  cm and  $\theta \simeq 90^\circ$ . Fig. 3(a) shows a picture of the flow where the dye causes a brighter region in the form of a ring between  $R - h_1$  and  $R$ . This shape indicates that the dye is transported not only azimuthally around the container but also radially *inward* from  $r \simeq R$  to  $r \simeq R - h_1$ . This inward motion towards the center is opposite to the outward one caused by the centripetal force detected in Fig. 2(b). Trapped by the TC vortex, the fluorescent dye remains confined in the region between  $R - h$  to  $R$  leading to a strong light intensity gradient as a function of  $r$  reflecting the complete absence of dye for  $r < R - h$ .



The existence of a radially inward motion caused by the axisymmetric TC vortex is verified by determining the radial velocity  $v_r$  radial dependence. As explained above, this quantity is obtained as beads are followed as a function of time. For  $Re = 156$ , the result is shown in Fig. 4(d) where  $v_r$  is plotted in dots and the average value,  $V_r$ , is illustrated in a thick solid line. In the central region we have  $V_r/V_\theta \simeq 1/40$  and the sign of  $V_r$  is positive reflecting an outward motion in agreement with the centrifugal acceleration induced motion. Towards the edge, the radial velocity decreases while the azimuthal one remains roughly unchanged leading to  $V_r/V_\theta \sim 1/100$ . Around  $r \simeq r_1$ ,  $V_r$  decreases sharply going through zero and then taking negative values indicating radial motion towards the center of the setup. This negative  $V_r$  confirms and quantifies the observations made using the fluorescent dye.

We deduce that at  $Re = 156$ , we have an azimuthal rotation caused by the Lorentz force on top of which comes adding motion caused by TC vortex at the outer edge which is an axi-symmetric rotational motion in the  $(r, z)$ -plane. The size of the TC vortex near the wall is about the height of the electrolyte layer. The primary instability, which generated motion in the  $(r, z)$ -plane, is unstable and leads to a *natural* breaking of the axial symmetry of the flow. By ‘natural’, we describe the fact that no velocity gradient is externally imposed on the system in any direction. Consequently, the transition occurs spontaneously at sufficiently large Reynolds number by increasing the current flowing in the electrolyte or/and by increasing the thickness of the fluid layer.

## V. NON-AXISYMMETRIC VORTICES BY INCREASING THE REYNOLDS NUMBER

At  $Re = 156$ , the coexistence of azimuthal rotation with the axisymmetric motion in the  $(r, z)$ -plane is steady as the state of the flow is unchanged even after for several minutes. We cannot judge for longer periods to avoid ohmic heating which could cause its own instabilities.

The stability of this three-dimensional flow is tested by increasing the total current leading to  $Re$  increasing from 156 to 228 while keeping the aspect ratio unchanged. As a result, the ring shape of the fluorescent dye, seen in Fig. 5(a), changes in (b) to form a polygonal structure. This behavior points towards the onset of a secondary instability leading to vortices in the azimuthal plane, thus breaking the axisymmetry of the flow. The deformation around  $r \simeq R - h_1$  continues to increase with time until the flow reaches a steady state,

depicted in (c), with the formation of  $m = 10$  vortices.

Since the onset of the non-axisymmetric structures takes place at  $r = r_1$ , which is the diameter of the TC vortex, it is thus natural to assume that this secondary instability is caused by the primary TC vortex dynamics and the consequent modifications to the average velocity profile. In fact, one can no longer neglect the motion in the  $(r, z)$ -plane and the consequent gradients. The onset of a secondary instability leads to an important increase of the fluctuations level of  $v_\theta$  around  $R - h_1$  depicted in Fig. 4(c). The radial profile of  $\delta V_\theta$  at  $Re = 156$  has one maximum at  $r_1$ , which corresponds to the maximum of the  $\partial_r(rV_\theta)^2$ . At  $Re = 228$ ,  $\delta V_\theta$  not only increases by a factor of 2.7, but also we record a shoulder at  $r \simeq r_1$  caused by the non-axisymmetric vortices.

We deduce that the dynamics related to the onset of the primary axisymmetric vortex appear to be the cause of a secondary instability, which leads to the onset of non-axisymmetric structures as the Reynolds number is increased. More evidence supporting this conclusion is supplied hereafter.

## VI. NON-AXISYMMETRIC VORTICES BY DECREASING THE ASPECT RATIO

The idea that the onset of the secondary non-axisymmetric instability takes place at the radial velocity shear layer,  $R - h$ , caused by the primary vortices is tested by increasing the height of the flow from  $h_1$  to  $h = h_2 = 2.5$  cm. This leads to the increase of the aspect ratio as well as the Reynolds number since the latter is linearly proportional to  $h$ . We divide this section into two parts: we first expose qualitative results using the fluorescent dye, followed by quantitative results using beads tracking and velocity measurement.

### A. Imaging the Onset of the Non-axisymmetric Instability

In order to image the onset of the secondary instability, and before we turn on the current, we diffuse the fluorescent dye throughout the fluid so that we have a uniform light emission. To do so, we inject the dye at different locations, we stir manually and then wait until the flow is motionless. We turn on the biasing power supply driving current into the electrolyte solution and record the evolution of the flow. The time the current is switched on is considered to be the origin  $t = 0$ .

Fig. 5 shows four images in false colors taken at different times of evolution of the flow using the same color axis. The subplot (a) is taken at  $t = 16$  s where the centrifugal force pushes the dye initially present near the center towards the edge generating a void recognized by its low level of light intensity.

At  $t = 40$  s, the dye becomes radially concentrated around  $r_2$  as illustrated in Fig. 5(b). This is produced by two effects acting in opposite radial directions: (1), the centrifugal force that moves the dye towards the outer edge, and (2) the TC vortex at the edge, which gives rise to a radial velocity pushing the dye towards the center. The former increases the void at the center of the flow, the latter causes a ring-shape void that one can see all around the container in the range  $R - h_2 < r < R$ .

At  $t = 63$  s, and without changing the conditions of the experiment, Fig. 5(c) shows that the dye intrudes into regions away from  $r_2$  at the two azimuthal angles  $\theta \simeq 45$  and  $225^\circ$ . This behavior is the consequence of the onset of the non-axisymmetric instability leading to motion in the azimuthal plane. As we follow in time these structures, they develop to become a set of 6 rotating vortices in the azimuthal plane. As a function of time, the number of azimuthal vortices increases from 2, as seen in (c) until it reaches  $m = 6$  at  $t = 115$  s as shown in (d).

For a better image of the secondary vortices, we perform a similar experiment, under the same conditions, but the fluorescent dye is inserted at  $t \simeq 60$  s at the shear location  $r_2$ . Fig 12(a) is taken 30 seconds later and clearly shows five vortices in the azimuthal plane.

## B. Radial Velocity Profiles

We turn into quantifying the results of the previous section by inserting fluorescent beads and following them as a function of time. We recall that the azimuthal velocity is determined from three consecutive frames, whereas, the radial velocity is determined for beads that undergo more than a full rotation. We use two Reynolds numbers  $Re = 240$  and  $380$ . Consequently, we have the case of two aspect ratios,  $\Gamma = 6.7$  and  $4$  but with the same Reynolds number about  $230$ .

In Fig. 6(a), we plot the radial profiles of  $V_\theta$  at the two  $Re$  where one can note that neither the amplitude nor the flat profile shape in the central region changed when compared to the case of where the flow has  $h = h_1$ . Consequently, the flow is still TC unstable near the outer wall leading to a primary vortex with diameter equals to  $h_2$ , and this is reflected in different ways:

1. The circulation in the  $(r, z)$ -plane, caused by the TC vortex, naturally leads to an increase in the boundary layer thickness deduced from the radial position where  $V_\theta$  starts to decrease towards 0. This position is deduced from Fig. 6(a) to be about  $r_2 \simeq h_2 = 2.5$  cm. Consequently, it increased from  $r_1$  for  $h_1$  to  $r_2$  for  $h_2$  in agreement with the existence of a TC vortex at the edge with size about the height of the flow. Moreover, from Fig. 6(a), one can also note that the boundary layer thickness does not depend on the Reynolds number. It appears that the main parameter dictating its dimension is the aspect ratio.
2. For  $h_1$ , we witnessed an increase in the level of fluctuations when the flow becomes unstable due to the TC instability. Furthermore, when we increased the Reynolds number, this level increased even more, by a factor of 2.7, and we recorded a shoulder around  $R - h_1$ . The comparison of  $\delta V_\theta$  for  $h_2$  with respect to  $h_1$  is done in Fig. 6(b). The effect of the non-axisymmetric vortices on the fluctuation level is clearer as it leads to another peak in the fluctuation intensity at  $R - h_2$ .
3. The radial velocity profile presented a gradient at  $r = r_1$  for  $h = h_1$ . Now this gradient clearly moved to  $r = r_2 \simeq 7 = R - h_2$  cm as shown in Fig. 6(c). Consequently, the gradient region moved from  $r_1$  to  $r_2$ , which are the positions of the TC vortex edge.

We conclude this section by highlighting the fact that we were able to generate non-axisymmetric structures in the absence of external gradients. They result from the natural onset of a secondary instability with a source that is the gradients generated by the axisymmetric vortex, which results from the Taylor-Couette instability. Moreover, the poloidal mode number increases from  $m \simeq 6$  to 10 as the aspect ratio is decreased from 6.7 to 4. This is confirmed by changing the aspect ratio while keeping the Reynolds number approximately the same. By performing several experiments, we noted that the most unstable azimuthal mode number dependence on  $Re$  is weak changing in the range 5 to 7 before the flow becomes turbulent at high values of the Reynolds number. This is in agreement with the theoretical analysis developed in the next section.

## VII. THE THEORY OF THE SECONDARY INSTABILITY

It is rather well-known that axisymmetric perturbations of a rotating flow leads to the onset of the Taylor-Couette instability caused by the velocity gradient, which in our case

takes place at the boundary layer. The onset of the instability modifies the velocity profile with vortices in the  $(r, z)$ -plane. In this section, we study, for the first time, the onset of non-axisymmetric structures, caused by the TC vortices, using perturbation theory.

### A. Toroidal Channel Flow with Two Counter-Rotating Vortices

The experiment showed the existence of one TC vortex at the edge for  $R - h \leq r \leq R$ . However, one can assume that there is a second one rotating in the opposite direction occurring in the range  $a \leq r \leq R - h$  by conservation of momentum. The evidence of the second vortex will be presented using direct numerical simulation discussed hereafter. We consider a flow that is formed of two counter-rotating vortices, as illustrated in Fig. 7(a), which are also rotating at a constant azimuthal velocity in the toroidal channel. The fluid has a height  $h$  with an outer radius of  $R_o = R$  and an inner radius of  $R_i = R - 2h$ .

Because of the cylindrical symmetry, the solutions of the Taylor-Couette instability are Bessel functions in terms of  $r$ . They are approximated by sine waves for the case of shallow rotating flows considering  $r \rightarrow \infty$ . The equations for the velocities can take the form:

$$V_{r0} = \frac{\delta V}{r^{1/2}} \sin(K_r(r - h)) \cos(K_z z) \quad (2)$$

$$V_{z0} = \frac{\delta V}{r^{1/2}} \cos(K_r(r - h)) \sin(K_z z) \quad (3)$$

$$V_{\theta 0} = C_\theta \quad (4)$$

where  $C_\theta$  is a constant and  $\delta V$  reflects the amplitude of the two counter-rotating vortices in the  $(r, z)$ -plane. One can verify that these velocities obey to the Navier-Stokes equations in the limit  $r \rightarrow \infty$ . We assume no-slip boundary conditions for  $V_r$  and  $V_z$  leading to  $K_r = K_z = \pi/h$ . For  $V_\theta$ , we assume a slip boundary condition at the walls in order not to have gradients in  $r$  and  $z$  directions. Consequently, the only gradients are those caused by the two vortices that simulate the TC vortices.

### B. The Perturbation Method

The four conservation equations, reflecting the continuity and momentum, are normalized according to  $x \rightarrow x/h$ ,  $v \rightarrow v/C_\theta$  and time  $t \rightarrow tC_\theta/h$ . Then, they are linearized to the first

order after letting  $v_r = V_{r0} + v_{r1}(r, \theta, z)$ ,  $v_\theta = V_{\theta0} + v_{\theta1}(r, \theta, z)$ ,  $v_z = V_{z0} + v_{z1}(r, \theta, z)$  and  $p = p_0 + p_1(r, \theta, z)$ ; The index ‘1’ denotes the perturbed quantities. We search for plane-wave solutions of the form  $\sim \exp -i(\omega t + k_r r + m\theta + k_z z)$  with  $\omega \in \mathbb{C}$  whereas  $k_r$ ,  $m$  and  $k_z \in \mathbb{R}$ . The result is put in a matrix form  $\underline{M}.V = 0$ , where non-trivial solutions are obtained by setting the determinant of the matrix  $\underline{M}$  equals to 0. This leads to a second order equation with two solutions  $\omega_1$  and  $\omega_2$ . The real part of the solutions reflects the oscillation frequency of the modes. The imaginary part, denoted by  $\gamma$ , acts on the initial amplitude of the velocities and pressure. If  $\gamma_1$  or  $\gamma_2$  is greater than 0, the amplitude of the perturbation grows over time reflecting an instability. On the other hand,  $\gamma < 0$  leads to an exponential perturbation decay with time. If different growth rates exist, the most positive one will dominate the dynamics since this mode will grow the fastest.

### C. Parameters of the Non-axisymmetric Instability

Five parameters exist that dictates the values of the growth rate and mainly their sign as we search for positive  $\gamma$ 's that indicate the onset of an instability. They are the Reynolds number  $Re$ , the ratio of the counter-rotating vortices amplitude with respect to the azimuthal rotation  $\delta V/C_\theta$ , the radial wavenumber  $k_r$ , the axial wavenumber  $k_z$  and azimuthal mode number  $m$ . In this study, we set  $h = 2.5$  cm and fix  $hk_r = \pi/2$ , as we look at the formation of one vortex in the radial direction similar to what was shown in Fig. 5(d). This leaves us with three parameters as the poloidal mode number is chosen to be the variable with respect to which  $\gamma$  is plotted.

The plot of  $\gamma$  as a function of  $r$  and  $z$  is shown in Fig. 7(b). The layer in-between the vortices possesses a positive  $\gamma$ , hence predicting the onset of the non-axisymmetric instability in this region. Positive  $\gamma$ 's are detected where the gradient is maximum. Now that we found that positive growth rate exists, we turn towards the dependencies on the three parameters  $hk_z$ ,  $Re$  and  $\delta V/C_\theta$  with  $\gamma$  plotted as a function of the poloidal mode number  $m$ .

Based on our experimental results, we set the azimuthal rotation to be  $C_\theta = 2$  cm/s and the ratio of the TC vortices velocity when compared to the azimuthal one to be  $\delta V/V_\theta = 0.01$ . In Fig. 8(a), we plot the growth rate as a function of  $m$  for different values of  $hk_z$ . The axial wavenumber appears to play a role in two ways. First, it changes the values of  $\gamma$  making the flow stable for  $hk_z \geq \pi/20$ . In terms of axial wavelengths, stability is reached for  $\lambda_z \leq 40h$ . Accordingly, the wavelength in the  $z$ -direction has to be much larger than the height of the fluid indicating that barotropic vortices, in the sense that the gradient along the  $z$ -direction

is very small, are unstable to non-axisymmetric perturbations. The second role of  $hk_z$  is the modification of the most unstable azimuthal mode number as it decreases from 6 to 4 with increasing  $\lambda_z$  (decreasing  $hk_z$ ). We deduce that in order for this calculation to be in agreement with the experiment, the axial wavelength could be of the order of  $40h$ .

In the dependence on the Reynolds number, which is set by  $C_\theta$  as we keep the height of the fluid and other parameters unchanged, we choose  $hk_z = 9\pi/200$  in addition to  $hk_r = \pi/2$ . Fig. 8(b) shows the growth rate as a function of  $m$  for different values of the Reynolds number, which chosen to be in the range of the experimental values. For Reynolds numbers smaller than 350, the flow is stable as  $\gamma$  is negative for all  $m$ 's. Moreover, the Reynolds number affects not only the amplitude but also the most unstable mode number similar to the effect of  $k_z$ . With increasing  $Re$  from 333 to 583, the most unstable mode number changes from 5 to 6. One can verify that the growth rate increases with increasing  $h$ , from the behavior of the Reynolds number, in agreement with the experiment.

The last parameter is  $\delta V/C_\theta$ . For its dependence, we set  $hk_z = 9\pi/200$ ,  $hk_r = \pi/2$  and  $Re = 417$  corresponding to a rotation velocity of 1.7 cm/s. Although theoretically this parameter is modified independently of  $C_\theta$ , in practice however,  $\delta V$  varies linearly with  $C_\theta$ . The result of the calculation is plotted in Fig. 8(c) where one notes a strong dependence on this parameter with the flow becoming unstable for  $\delta V/C_\theta > 0.008$ . Experimentally the ratio of the two velocities is between 1/50 and 1/100, which in the range of the theoretical values where  $\gamma$  is positive. We emphasize that the increase of  $\delta V/C_\theta$  does not lead to a modification of the azimuthal mode number corresponding to maximum growth rate.

#### D. Conclusions from the Theory

To summarize the various dependencies, we plot in Fig. 8(d) the maximum growth rate as a function of the three parameters discussed above. The  $x$ -axis thus represents  $\delta V/C_\theta$ ,  $hk_z/10$  or  $Re/2 \times 10^4$  depending on the graph. The theoretical analyses indicates that the flow composed of two vortices in the  $(r, z)$ -plane and rotating azimuthally in a toroidal channel is unstable to non-axisymmetric perturbations. The fact that we set  $V_\theta$  to be a constant indicates that its gradients are not a necessary condition for the secondary instability. It is found that the conditions for the instability are close to our experiment mainly when it comes to (1) the most unstable azimuthal mode  $m$  found to be about 6, (2) the critical Reynolds number with  $Re_c \simeq 350$ , and (3) the velocity of the counter rotating vortices when compared to the azimuthal rotation with  $(\delta V/C_\theta)_{critical} \simeq 1/100$ . Also in agreement

with the experiment, the azimuthal mode number is not found to critically depend on the Reynolds number.

## VIII. NUMERICAL SIMULATION OF AZIMUTHALLY ROTATING FLOWS

In this section, we present direct numerical simulation (DNS) results of the rotating flow presenting excellent agreement with the experiment supporting the idea that the axial symmetry is broken by the onset of a secondary instability caused by the shear layer developed from the primary instability. The goal of this section is to reproduce the experimental results and to gain more insights into the physical phenomena behind the symmetry breaking. Moreover, numerical simulations give access to the flow structure in the  $(r, z)$ -plan, which was not possible in the experimental study. We continue by discussing the numerical procedure followed by the results.

### A. Numerical Procedure

The code solves the incompressible Navier-Stokes equations for conducting or non-conducting fluid subject to a Lorentz force  $\mathbf{F}$ .

$$\nabla \cdot \mathbf{v} = 0, \quad (5)$$

$$\frac{\partial \mathbf{v}}{\partial t} + (\mathbf{v} \cdot \nabla) \mathbf{v} = -\frac{\nabla p}{\rho} + \nu \nabla^2 \mathbf{v} + \frac{\mathbf{F}}{\rho} \quad (6)$$

$$\nabla^2 \Phi = \nabla \cdot (\mathbf{v} \times \mathbf{B}). \quad (7)$$

In the above equations,  $p$  is the static pressure,  $\nu$  is the kinematic viscosity and  $\Phi$  is the electrostatic potential. Ohm's law, which states that  $\mathbf{j} = \sigma (-\nabla \Phi + \mathbf{u} \times \mathbf{B})$ , is used to reconstruct the current density  $\mathbf{j}$  during the numerical simulations. The numerical value of the vacuum permeability is  $\mu_0 = 1.1 \times 10^{-6}$  H/m and the electric conductivity of the working fluid is  $\sigma = 55$  S/m.

The numerical method used in this paper is based on that proposed by [45] and [46] to study three-dimensional conducting flows with electromagnetic forcing. It was discussed in detail and validated in a previous study in Refs. [47, 48] where excellent agreement was obtained with the literature data of a forced toroidal channel flow as well as with a confined



vortex-pair. The solver was also validated with respect to experimental data for a quasi-two-dimensional turbulent flow in the presence of non-uniform magnetic field [49].

The numerical simulations of the governing equations are performed using the open source C++ library OpenFOAM 5.0, which is based on the finite volume approach [50, 51]. For each time step, the code first initializes the Lorentz force ( $\mathbf{F} = \mathbf{j} \times \mathbf{B}$ ). Then, Eqs. (5) and (6) are solved using the PISO algorithm [52] to obtain the velocity and pressure. Poisson's equation is then solved to obtain  $\Phi$ . Finally, the current density at each cell center is reconstructed [45, 46] and the new Lorentz force is obtained to be used in Eq. (6). The above steps are then iterated about five times for each time step to ensure accurate coupling between the velocity and electric current. These iterations are sufficient to reach a convergence criterion of  $10^{-6}$ .

Non-uniform hexahedral mesh is used in the present study to cover the 10 cm radius and the 2.5 cm height of fluid. The total number of cells was around 13 million cells. On all the solid boundaries including the electrodes and bottom surface, a no-slip boundary condition is used for the velocity field ( $\mathbf{v} = 0$ ) and for the pressure  $\partial p / \partial n = 0$ , where  $n$  is the outwards facing normal of the domain. The upper surface is modeled as free shear surface with atmospheric pressure. Constant electric potential is fixed on the electrodes.

The pressure and electric potential equations are solved by using a pre-conditioned conjugate gradient (PCG) iterative solver with a diagonal incomplete Cholesky (DIC) preconditioner used for symmetric matrices. The velocity-pressure coupling equation uses the asymmetric pre-conditioned bi-conjugate gradient solver (PBiCG) with a diagonal incomplete LU decomposition (DILU) preconditioner for asymmetric matrices. The same convergence criterion of  $10^{-6}$  is used for velocity, pressure and electric potential. For more details about the numerical solver the reader is referred to Ref. [47].

The temporal discretization is performed using a second order implicit scheme. The time step is automatically adapted during the simulations by using the Courant number  $Co_{max} = \Delta t \Delta V / \Delta x = 1$  determined for each cell; the magnitude of the flow velocity at the given cell is  $\Delta V$ ,  $\Delta x$  is the cell size in the velocity direction and  $\Delta t$  is the time step. Therefore, by fixing  $Co_{max} = 1$ , the time step is computed from the minimum value of  $\Delta t = \Delta x / \Delta V$  taken over all fluid cells.

## B. Results using DNS on the Onset of Primary and Secondary Instability

From the experiment and the theory developed above, we learned that the growth rate of the instability increases with height. Consequently, and in order to save computational time,

we select  $h = 2.5$  cm and study the onset of primary and secondary instabilities occurring respectively in time. The goal of this section is to present the simulation results and as we compare them with the experiment we deduce that we have excellent agreement between the two methods.

### 1. *The Laminar State*

Fig. 9(a) and (b) show respectively the radial and azimuthal velocities of the top fluid layer taken at  $t = 5$  s. They are determined before the onset of the primary or the secondary instabilities as one can deduce from the lack of vortical structures in the radial as well as the azimuthal directions. In Fig. 9(c), the radial profiles of  $V_\theta$  and  $V_r$  are plotted. For  $V_\theta$ , we record an exponential decay with  $r$ . The radial velocity also decreases strongly with  $r$  after reaching a maximum around 1 cm from the center. One can verify that at this stage  $V_r$  is mainly driven by  $V_\theta$  caused by the centrifugal force. The sign of  $V_r$  is positive for all  $r$ 's indicating an outward motion and it becomes negligible for  $r > 6$  cm. All the results are in agreement with the experiment with  $h = 0.3$  cm where the flow is laminar.

### 2. *The Primary Taylor-Couette Instability at the Outer Boundary Layer*

In Fig. 10, we illustrate the state of the flow at  $t = 40$  s while keeping the forcing and all other parameters constant. The azimuthal and radial velocities of the top fluid layer are shown in (a) and (b) respectively. They both present major differences with respect to the laminar state taken at  $t = 5$  s. For  $V_\theta$ , one can see a net decrease in the color gradient in the bulk of the flow reflecting a decrease in the radial gradient far from the boundaries. One also note that the flow remains axisymmetric reflected by the lack of structures in the azimuthal plane. The gradient in  $V_\theta$  is detected mainly at the edge with a boundary layer thickness changing from a couple of millimeters, before the onset of the primary instability, to about 2 cm after its onset caused by the primary TC vortex. The change of the  $V_\theta$  profile from exponentially decaying to rather flat far from the edges is in excellent agreement with the experiment.

For  $V_r$ , the difference with the laminar case is even more dramatic where we note the existence of a ring, which reflects the TC axisymmetric vortex. This is in striking agreement with Fig. 5(a) where we inserted dye at the edge the container and pictured the flow after the onset of the primary instability. In both figures, the TC vortex leads to a ring-shaped

structure at  $R - h < r < R$ . Using the DNS, the onset of the primary instability caused by the velocity gradient at the wall is best seen with a cut in the  $(r, z)$ -plane shown in Fig. 10(c) for  $V_r$ . The circulation caused by the onset of the primary Taylor-Couette instability is clear leading to the co-existence of two counter-rotating vortices, one for  $r > R - h$  with a counter-clockwise rotation and the other elongated in the radial direction between  $a$  and  $R - h$  in the clockwise direction. The latter enhances the radial transport from the center to the outer wall contributing to the flattening of the azimuthal velocity profile far from the boundaries. The co-existence of two counter-rotating vortices is hard to obtain experimentally and is a direct consequence of the conservation of momentum. It justifies *a posteriori* the use of two counter-rotating vortices in our theoretical analysis. The effect of the TC vortex on  $V_r$ , shown in (e), leads to a negative radial velocity in the range  $R - h < r < R$ . These results are in excellent agreement with the experiment.

### 3. The Secondary Instability and the Breaking of the Axial Symmetry

The profiles of  $V_\theta$  and  $V_r$  after the onset of the secondary instability are shown in Fig. 11(a) and (b) respectively. The breaking of the axisymmetry of the flow is clear in the absence of any externally driven gradient at  $r = R - h$ . We verified that by changing  $h$ , not only the growth rate changes, but also the radial position where the secondary instability takes place as it is the case in the experiment. We note the onset of four vortices in the azimuthal plane enhancing the mixing in the radial direction with negative radial velocities reaching areas from from the shear region. The secondary instability changes the radial profile of  $V_\theta$  in the boundary layer without drastically modifying the boundary layer thickness, which is still dominated by the TC vortex.

The onset of the secondary instability modifies the profiles of  $V_\theta$  and  $V_r$  mainly near  $R - h$ . For the radial velocity, before the onset of the primary instability, it was determined by the centrifugal force, that is set by  $V_\theta$ . Its sign is only positive throughout the domain reflecting outward motion only. The primary instability leads to a rotation in the opposite direction detected in the simulation by a negative radial velocity, which occurs for  $r > R - h$ . After the secondary instability, the radial velocity amplitude grows slightly but its main characteristics remain.

### C. Conclusion of the Numerical Simulation

In conclusion, performing direct numerical simulation of the rotating flow with conditions similar to the experiment confirmed that the axisymmetry of shallow rotating flow is broken by the onset of a secondary instability at the shear layer generated by the TC vortices, which results from the primary instability. The comparison between the DNS and the experiment shows excellent agreement before the primary instability, before and after the secondary instability.

## IX. CONCLUSION AND FUTURE WORK

Our experiment demonstrated the onset of non-axisymmetric structures in shallow rotating flows occurs ‘naturally’ in the absence of external forcing of a velocity gradient. We use a thin layer of an electrolyte freely and azimuthally rotating in response to the Lorentz force generated by an axial magnetic field and a radially decaying current. We found that the azimuthal velocity gradient near the outer wall excites the Taylor-Couette instability, in agreement with the theory. This leads to radial gradients in the velocity field, which are at the origin of the secondary instability occurring at the distance  $(R - h)$  from the center. The non-axisymmetric instability is thus a natural evolution after the onset of the primary instability. Consequently, we claim that our findings apply to a wide range of rotating and shallow flows where primary instabilities lead to the onset of vortices in the radial-height plane. We complement our experimental results by a theoretical model, which consists of two counter-rotating vortices in the  $(r, z)$ -plane in addition to the azimuthal rotation. The stability analysis of this flow indicates the onset of non-axisymmetric instability leading to an azimuthal mode number around five for parameters that are close to the experiment. Excellent agreement between the theory and the experiment is thus obtained. Furthermore, direct numerical simulation is also conducted using a finite volume numerical method replicating the experimental flow. The results are also in agreement with the experiment with a primary instability kicking in at the outer boundary layer followed by a secondary instability generating four non-axisymmetric structures.

This study shows a new route towards 3D complex motion in an unexplored shallow flow configuration. The 3D vortical motion takes place at relatively low Reynolds numbers ( $Re \sim 300$ ) with large-scale structures. Hence, we expect it to have strong impact on the angular momentum transport and on the resulting turbulent mixing. Increasing the aspect

ratio leads to a lower azimuthal mode number and thus to larger primary vortex size.

Future work will be dedicated to the understanding of turbulence in these flows and the interaction among the vortices. Fig. 12(a) illustrates the flow with  $h = 2.5$  cm after the onset of the secondary instability and gives a clearer image of the secondary vortices in the azimuthal plane, which is in agreement with Fig. 5. As we increase the Reynolds number by increasing the current, the interaction among the vortices leads to a state represented in (b) where the dynamics are complex and require dedicated investigation. It is worth also pursuing in parallel the work using DNS. The agreement with the experiment apparently extends to higher Reynolds numbers as one can see from (c), which shows the same type of structures as in (b) when the flow is in the turbulent state.

Hereafter, we briefly discuss three areas for future work where the onset of a secondary instability could play a major role in understanding the underlying dynamics.

In planetary geophysical flows, the above results have important implications as they emphasize the strong interaction between motions parallel and perpendicular to the planet surface in the formation of non-axisymmetric structures. The case of the hexagonal structure observed on Saturn north pole [53–56] or more recently the set of vortices observed near the north pole of Jupiter [?] is of particular interest and is worth revisiting in the lights of the present experimental findings. Our results suggest that the origin of this structure could lie in the coupling between the atmospheric rotational motion near the pole with the vertical motion caused, for example, by convection cells. The vertical motion on Saturn and Jupiter are known to be enhanced by its thick gaseous atmosphere [57], which appears to be an important parameter according to our study. It is worth noting that, like other experiments but in the absence of a radial shear in the azimuthal velocity, we have reproduced the Saturn hexagonal structure in a laboratory experiment.

Future investigations of the secondary instability role at low Reynolds numbers could help us understand planets formation around protostar [58–61]. After the formation of a disk of dust around it, a primary instability of hydrodynamic or magnetohydrodynamic nature could be excited. The interaction of the resultant axisymmetric vortex with the rotational motion is expected to excite the secondary instability leading to the formation of non-axisymmetric structures [62–64]. Our results suggest that planets could emerge early on after the disk formation since vortices in the azimuthal plane tend to agglomerate matter around their centers quite rapidly. The inward rotational motion towards the vortices centers added to the gravitational attractive field lead to a strong acceleration of the rate at which planets

are formed.

Several observations have documented the active dynamics of accretion disks around black holes with indications of non-axisymmetric structures [65–68]. On the other hand, it was suggested that strong turbulence is needed to explain the temperatures detected in accretion disks [14, 69–74]. These flows are expected to be subject to a MR instability where the magnetic field fluctuations lead to the formation of axisymmetric vortices similar to our primary vortex. Based on our results, future work could investigate the role of a secondary instability in the onset of the non-axisymmetric structures in accretion disks. Moreover, because the vortical structures are in the azimuthal plane and they have large scales, the resultant 3D motion could give rise to strong turbulence. Consequently, we hypothesize that the non-axisymmetry and the strong turbulence in accretion disks around black holes could have the same origin, that is, the onset of a secondary instability in the flow.

### **Acknowledgments**

Fruitful discussions with Drs. J. Fraine, M. Darwish and X. Garbet are acknowledged.

- 
- [1] Peter RN Childs. *Rotating flow*. Elsevier, 2010.
- [2] Patrick H Diamond, Sanae-I Itoh, and Kimitaka Itoh. *Modern Plasma Physics: Volume 1, Physical Kinetics of Turbulent Plasmas*. Cambridge University Press, 2010.
- [3] Joseph Pedlosky. *Geophysical fluid dynamics*. Springer Science & Business Media, 2013.
- [4] James Binney and Scott Tremaine. Galactic dynamics. *Princeton Series in Astrophysics (Princeton: Princeton Univ. Press)*, 1998.
- [5] Subrahmanyan Chandrasekhar. *Hydrodynamic and hydromagnetic stability*. Courier Corporation, 2013.
- [6] PG Drazin and LN Howard. Hydrodynamic stability of parallel flow of inviscid fluid. *Advances in applied mechanics*, 9:1–89, 1966.
- [7] FH Busse. Shear flow instabilities in rotating systems. *Journal of Fluid Mechanics*, 33(3):577–589, 1968.
- [8] BJ Bayly. Three-dimensional centrifugal-type instabilities in inviscid two-dimensional flows. *Physics of Fluids (1958-1988)*, 31(1):56–64, 1988.
- [9] Denis Sipp and Laurent Jacquin. Three-dimensional centrifugal-type instabilities of two-dimensional flows in rotating systems. *Physics of Fluids (1994-present)*, 12(7):1740–1748, 2000.
- [10] Paul Billant and Francois Gallaire. Generalized rayleigh criterion for non-axisymmetric centrifugal instabilities. *Journal of Fluid Mechanics*, 542:365–379, 2005.
- [11] Lord Rayleigh. On the dynamics of revolving fluids. *Proceedings of the Royal Society of London. Series A*, 93(648):148–154, 1917.
- [12] Steven A Balbus and John F Hawley. A powerful local shear instability in weakly magnetized disks. i-linear analysis. ii-nonlinear evolution. *The Astrophysical Journal*, 376:214–233, 1991.
- [13] Steven A Balbus, John F Hawley, and James M Stone. Nonlinear stability, hydrodynamical turbulence, and transport in disks. *The Astrophysical Journal*, 467:76, 1996.
- [14] Steven A Balbus. Enhanced angular momentum transport in accretion disks. *arXiv preprint astro-ph/0306208*, 2003.
- [15] Tony Maxworthy. Turbulent vortex rings. *Journal of Fluid Mechanics*, 64(02):227–240, 1974.
- [16] EJ Hopfinger and GJFV Heijst. Vortices in rotating fluids. *Annual review of fluid mechanics*,

- 25(1):241–289, 1993.
- [17] GJF Van Heijst and HJH Clercx. Laboratory modeling of geophysical vortices. *Annual Review of Fluid Mechanics*, 41:143–164, 2009.
- [18] K Stewartson. On almost rigid rotations. *Journal of Fluid Mechanics*, 3(01):17–26, 1957.
- [19] K Stewartson. On almost rigid rotations. part 2. *Journal of fluid mechanics*, 26(01):131–144, 1966.
- [20] M Rabaud and Y Couder. A shear-flow instability in a circular geometry. *Journal of Fluid Mechanics*, 136:291–319, 1983.
- [21] JM Chomaz, M Rabaud, C Basdevant, and Y Couder. Experimental and numerical investigation of a forced circular shear layer. *Journal of fluid mechanics*, 187:115–140, 1988.
- [22] Hiroshi Niino and Nobuhiko Misawa. An experimental and theoretical study of barotropic instability. *Journal of the atmospheric sciences*, 41(12):1992–2011, 1992.
- [23] Wolf-Gerrit Frueh and Peter L Read. Experiments on a barotropic rotating shear layer. part 1. instability and steady vortices. *Journal of Fluid Mechanics*, 383:143–173, 1999.
- [24] W-G Früh. Methods to describe barotropic vortices by global fields and vortex characteristics. *Nonlinear Processes in Geophysics*, 9(3/4):189–200, 2002.
- [25] Ana C Barbosa Aguiar, Peter L Read, Robin D Wordsworth, Tara Salter, and Y Hiro Yamazaki. A laboratory model of saturns north polar hexagon. *Icarus*, 206(2):755–763, 2010.
- [26] J Sommeria, SD Meyers, and Harry L Swinney. Experiments on vortices and rossby waves in eastward and westward jets. *Nonlinear Topics in Ocean Physics*, 109:227–269, 1991.
- [27] Peter M Saunders. The instability of a baroclinic vortex. *Journal of Physical Oceanography*, 3(1):61–65, 1973.
- [28] By P Hignett, AA White, RD Carter, WDN Jackson, and RM Small. A comparison of laboratory measurements and numerical simulations of baroclinic wave flows in a rotating cylindrical annulus. *Quarterly Journal of the Royal Meteorological Society*, 111(467):131–154, 1985.
- [29] PL Read, MJ Bel, DW Johnson, and RM Small. Quasi-periodic and chaotic flow regimes in a thermally driven, rotating fluid annulus. *Journal of Fluid Mechanics*, 238:599–632, 1992.
- [30] RT Pierrehumbert and KL Swanson. Baroclinic instability. *Annual review of fluid mechanics*, 27(1):419–467, 1995.
- [31] JA Van de Konijnenberg, Ah H Nielsen, J Juul Rasmussen, and B Stenum. Shear-flow insta-



- bility in a rotating fluid. *Journal of Fluid Mechanics*, 387:177–204, 1999.
- [32] Brian Launder, Sébastien Poncet, and Eric Serre. Laminar, transitional, and turbulent flows in rotor-stator cavities. *Annual review of fluid mechanics*, 42:229–248, 2010.
- [33] JM Lopez, JE Hart, F Marques, S Kittelman, and Jie Shen. Instability and mode interactions in a differentially driven rotating cylinder. *Journal of Fluid Mechanics*, 462:383–409, 2002.
- [34] Frédéric Moisy, Olivier Doaré, Thomas Pasutto, Olivier Daube, and Marc Rabaud. Experimental and numerical study of the shear layer instability between two counter-rotating disks. *Journal of Fluid Mechanics*, 507:175–202, 2004.
- [35] Sébastien Poncet, Roland Schiestel, and Marie-Pierre Chauve. Centrifugal flow in a rotor-stator cavity. *Journal of Fluids Engineering*, 127(4):787–794, 2005.
- [36] Sébastien Poncet. The stability of a thin water layer over a rotating disk revisited. *The European Physical Journal Plus*, 129(8):167, 2014.
- [37] VA Dovzhenko, AM Obukhov, and VM Ponomarev. Generation of vortices in an axisymmetric shear flow. *Fluid Dynamics*, 16(4):510–518, 1981.
- [38] Dolzhanskiĭ. Stability and vortex structures of quasi-two-dimensional shear flows.
- [39] FV Dolzhanskii, VA Krymov, and D Yu Manin. An advanced experimental investigation of quasi-two-dimensional shear flow. *Journal of Fluid Mechanics*, 241:705–722, 1992.
- [40] Sergey A Suslov, James Pérez-Barrera, and Sergio Cuevas. Electromagnetically driven flow of electrolyte in a thin annular layer: axisymmetric solutions. *Journal of Fluid Mechanics*, 828:573–600, 2017.
- [41] CW Tobias, M Eisenberg, and CR Wilke. Diffusion and convection in electrolysis a theoretical review. *J. Electrochem. Soc*, 99(12):359C–365C, 1952.
- [42] JN Agar. Diffusion and convection at electrodes. *Discussions of the Faraday Society*, 1:26–37, 1947.
- [43] Allen J Bard, Larry R Faulkner, et al. Fundamentals and applications. *Electrochemical Methods*, 2:482, 2001.
- [44] Diogo MF Santos, César AC Sequeira, and José L Figueiredo. Hydrogen production by alkaline water electrolysis. *Química Nova*, 36(8):1176–1193, 2013.
- [45] Ming-Jiu Ni, Ramakanth Munipalli, Peter Huang, Neil B Morley, and Mohamed A Abdou. A current density conservative scheme for incompressible mhd flows at a low magnetic reynolds number. part ii: On an arbitrary collocated mesh. *Journal of Computational Physics*,

227(1):205–228, 2007.

- [46] Vincent Dousset and Alban Pothérat. Characterization of the flow past a truncated square cylinder in a duct under a spanwise magnetic field. *Journal of Fluid Mechanics*, 691:341–367, 2012.
- [47] Charbel Habchi and Ghassan Antar. Direct numerical simulation of electromagnetically forced flows using openfoam. *Computers & Fluids*, 116:1–9, 2015.
- [48] Charbel Habchi and Ghassan Antar. The dynamics of two-dimensional turbulence excited at two scales using electromagnetic forces. *Physics of Fluids*, 28(5):055102, 2016.
- [49] LM Moubarak and GY Antar. Dynamics of a two-dimensional flow subject to steady electromagnetic forces. *Experiments in fluids*, 53(5):1627–1636, 2012.
- [50] Henry G Weller, Gavin Tabor, Hrvoje Jasak, and Christer Fureby. A tensorial approach to computational continuum mechanics using object-oriented techniques. *Computers in physics*, 12(6):620–631, 1998.
- [51] F Moukalled, L Mangani, M Darwish, et al. The finite volume method in computational fluid dynamics. 2016.
- [52] Raad I Issa. Solution of the implicitly discretised fluid flow equations by operator-splitting. *Journal of computational physics*, 62(1):40–65, 1986.
- [53] DA Godfrey. A hexagonal feature around saturn’s north pole. *Icarus*, 76(2):335–356, 1988.
- [54] Kevin H Baines, TW Momary, T Temma, BJ Buratti, M Roos-Serote, A Showman, RH Brown, RN Clark, PD Nicholson, SK Atreya, et al. The structure of saturn’s poles determined by cassini vims: Constraints on winds and horizontal and vertical cloud distributions. In *Bulletin of the American Astronomical Society*, volume 39, page 423, 2007.
- [55] Kevin H Baines, Thomas W Momary, Leigh N Fletcher, Adam P Showman, Maarten Roos-Serote, Robert H Brown, Bonnie J Buratti, Roger N Clark, and Philip D Nicholson. Saturn’s north polar cyclone and hexagon at depth revealed by cassini/vims. *Planetary and Space Science*, 57(14):1671–1681, 2009.
- [56] Arrate Antuñano, T Río-Gaztelurrutia, Agustin Sánchez-Lavega, and Ricardo Hueso. Dynamics of saturn’s polar regions. *Journal of Geophysical Research: Planets*, 120(2):155–176, 2015.
- [57] Graham O Hughes and Ross W Griffiths. Horizontal convection. *Annu. Rev. Fluid Mech.*, 40:185–208, 2008.

- [58] Xue-Ning Bai. Magnetorotational-instability-driven accretion in protoplanetary disks. *The Astrophysical Journal*, 739(1):50, 2011.
- [59] Eugene Chiang and AN Youdin. Forming planetesimals in solar and extrasolar nebulae. *Annual Review of Earth and Planetary Sciences*, 38:493–522, 2010.
- [60] S Inaba and P Barge. Dusty vortices in protoplanetary disks. *The Astrophysical Journal*, 649(1):415, 2006.
- [61] Anders Johansen, Hubert Klahr, and Th Henning. Gravoturbulent formation of planetesimals. *The Astrophysical Journal*, 636(2):1121, 2006.
- [62] P Barge and Je Sommeria. Did planet formation begin inside persistent gaseous vortices? *arXiv preprint astro-ph/9501050*, 1995.
- [63] Patrick Godon and Mario Livio. Vortices in protoplanetary disks. *The Astrophysical Journal*, 523(1):350, 1999.
- [64] Mark R Petersen, Keith Julien, and Glen R Stewart. Baroclinic vorticity production in protoplanetary disks. i. vortex formation. *The Astrophysical Journal*, 658(2):1236, 2007.
- [65] Sheperd S Doeleman, Jonathan Weintroub, Alan EE Rogers, Richard Plambeck, Robert Freund, Remo PJ Tilanus, Per Friberg, Lucy M Ziurys, James M Moran, Brian Corey, et al. Event-horizon-scale structure in the supermassive black hole candidate at the galactic centre. *Nature*, 455(7209):78–80, 2008.
- [66] Vincent L Fish, Sheperd S Doeleman, Avery E Broderick, Abraham Loeb, and Alan EE Rogers. Detecting changing polarization structures in sagittarius a\* with high frequency vlbi. *The Astrophysical Journal*, 706(2):1353, 2009.
- [67] Sheperd S Doeleman, Vincent L Fish, Avery E Broderick, Abraham Loeb, and Alan EE Rogers. Detecting flaring structures in sagittarius a\* with high-frequency vlbi. *The Astrophysical Journal*, 695(1):59, 2009.
- [68] Christopher S Reynolds. The spin of supermassive black holes. *Classical and Quantum Gravity*, 30(24):244004, 2013.
- [69] Hubert H Klahr and Peter Bodenheimer. Turbulence in accretion disks: vorticity generation and angular momentum transport via the global baroclinic instability. *The Astrophysical Journal*, 582(2):869, 2003.
- [70] Robert F Penna, Jonathan C McKinney, Ramesh Narayan, Alexander Tchekhovskoy, Rebecca Shafee, and Jeffrey E McClintock. Simulations of magnetized discs around black holes: effects

of black hole spin, disc thickness and magnetic field geometry. *Monthly Notices of the Royal Astronomical Society*, 408(2):752–782, 2010.

- [71] Jonathan C McKinney, Alexander Tchekhovskoy, and Roger D Blandford. General relativistic magnetohydrodynamic simulations of magnetically choked accretion flows around black holes. *Monthly Notices of the Royal Astronomical Society*, 423(4):3083–3117, 2012.
- [72] Marek A Abramowicz and P Chris Fragile. Foundations of black hole accretion disk theory. *Living Reviews in Relativity*, 16(1):1, 2013.
- [73] Feng Yuan and Ramesh Narayan. Hot accretion flows around black holes. *Annual Review of Astronomy and Astrophysics*, 52:529–588, 2014.
- [74] Aleksander dowski and Ramesh Narayan. Three-dimensional simulations of supercritical black hole accretion discs—luminosities, photon trapping and variability. *Monthly Notices of the Royal Astronomical Society*, 456(4):3929–3947, 2016.
- [75] [//www.nasa.gov/feature/jpl/nasa-s-juno-mission-provides-infrared-tour-of-jupiter-s-north-pole](http://www.nasa.gov/feature/jpl/nasa-s-juno-mission-provides-infrared-tour-of-jupiter-s-north-pole)

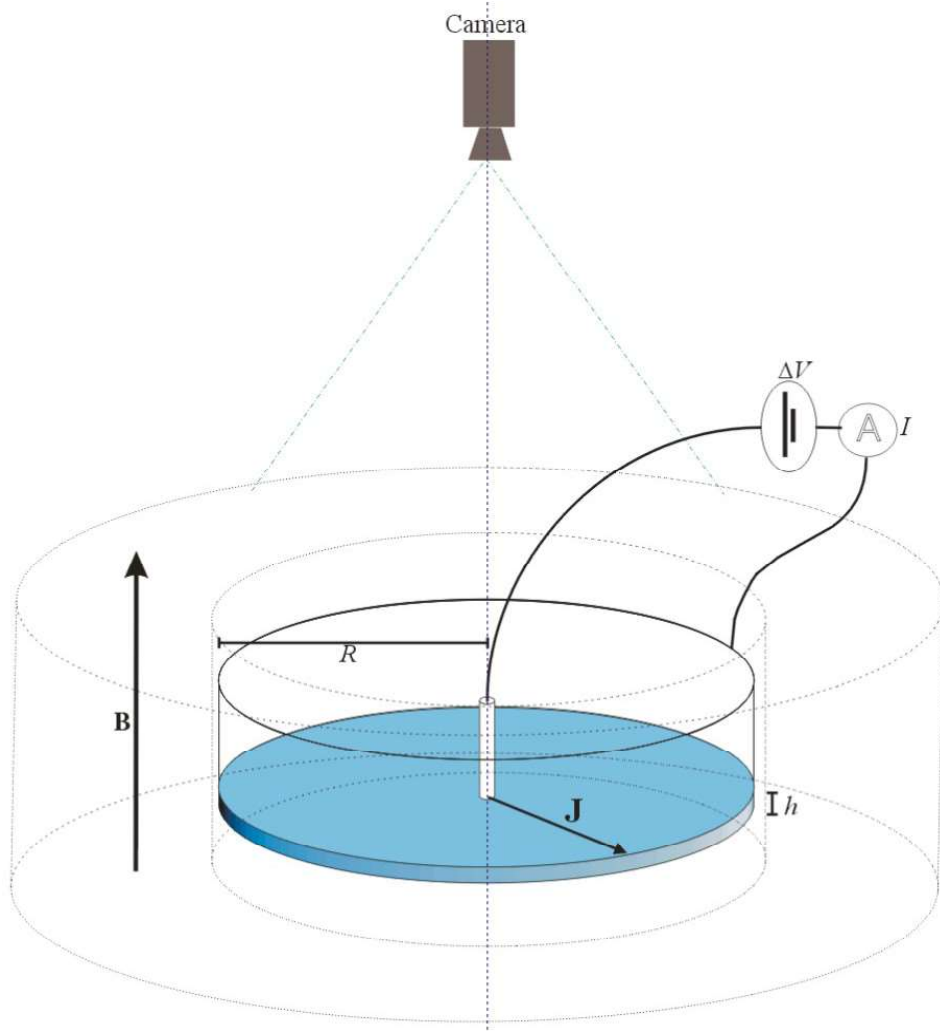


FIG. 1: The experimental setup is illustrated where the magnetic field  $\vec{B}$  is generated by a set of electromagnets illustrated in a dotted cylinder. A solution of potassium hydroxide is poured into the Plexiglas cylinder (the colored cylinder) up to a chosen height  $h$ . The current density  $\vec{j}$  is driven in the fluid by two electrodes biased by  $\Delta V$  using a power supply. The electrodes are made of stainless steel, one is a rod with radius 0.125 cm installed at the center of the container and the other is a sheet fixed on the inner wall of the Plexiglas cylinder. A high-resolution camera is installed at a distance about 50 cm from the container to image the fluid motion.

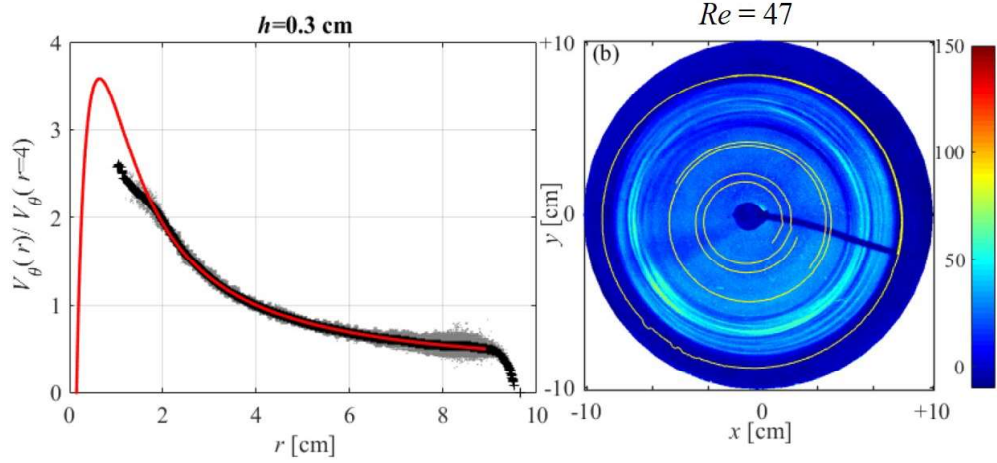


FIG. 2: In (a), we plot the profile of  $v_\theta/v_\theta(r = 4)$  for  $Re = 46$  in dots. The average radial profile is plotted in crosses (+) and the one from the two-dimensional theory in thick solid line; Good agreement is reached in the bulk of the flow far from the boundaries. In (b), a picture of the container in false colors where the bright area reflects the presence of the fluorescent dye. The motion of three beads as a function of time, deduced from the light intensity they generate, is overlaid. The bead near the center has a large radial displacement, the bead near the middle has a moderate radial displacement and the one at the edge having almost no radial displacement.

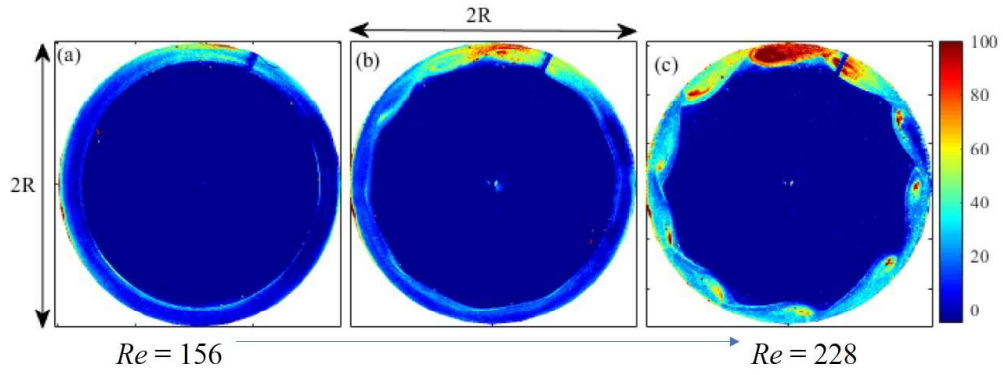


FIG. 3: The pictures in (a) and (c) are taken as the Reynolds number is increased from  $Re = 156$  to 228 due to the increase in the current from 90 to 120 mA. In (a), the effect of the TC vortex is visible as the dye, which was injected at the edge, remains confined to a ring with radius  $h$ . (b) shows the formation of a polygonal structure that appears during the evolution of the flow from (a) to (c) where we have  $m = 10$  vortices in the azimuthal plane.

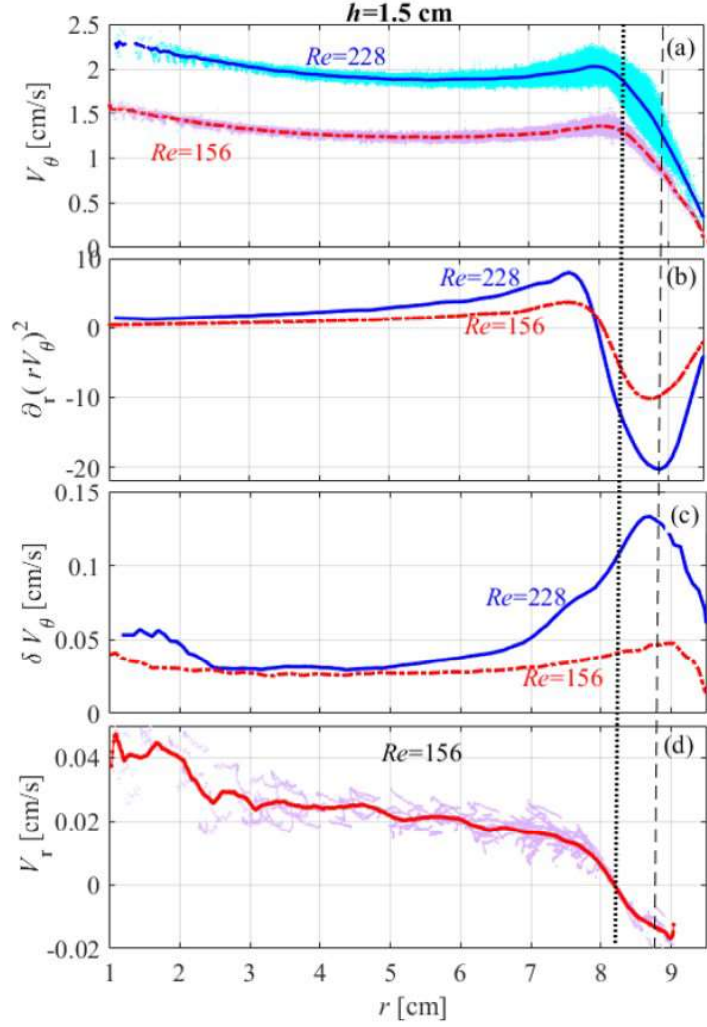


FIG. 4: In (a) we plot  $V_\theta$  vs  $r$  for two Reynolds numbers  $Re = 156$  and  $228$  at  $h = 1.5$  cm in dash-dotted and solid lines respectively. In (b),  $\partial_r (rV_\theta)^2$  vs  $r$  is shown to emphasize that the region  $r > r_1$  is TC unstable since it is negative. (c)  $\delta V_\theta$  vs  $r$  peaking at maximum  $\partial_r V_\theta$  for the two Reynolds numbers. In (d), the profile of  $V_r$  as measured by the beads location over time at  $Re = 156$ . The two vertical dashed lines illustrate the positions of the maximum of  $\partial_r V_\theta$  and  $\partial_r V_r$ .



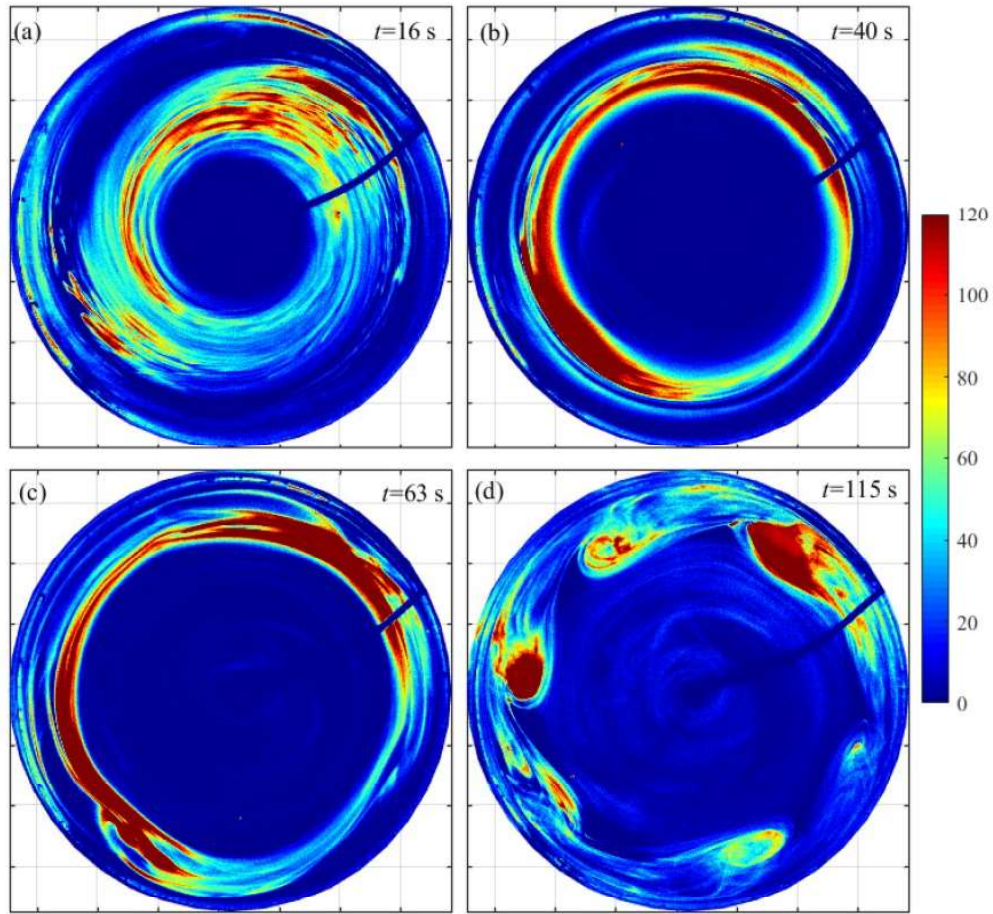


FIG. 5: At  $h = 2.5$  cm, the pictures in (a)-(d) show pictures of the flow in false colors at different times after the dye was distributed uniformly throughout the flow. The light intensity is proportional to the presence of the fluorescent dye. The Reynolds number is 240. Note the dye motion towards  $r_2$  in (a) and then (b), the onset of the non-axisymmetric instability at two azimuthal locations in (c) and the presence of  $m = 6$  vortices in (d).

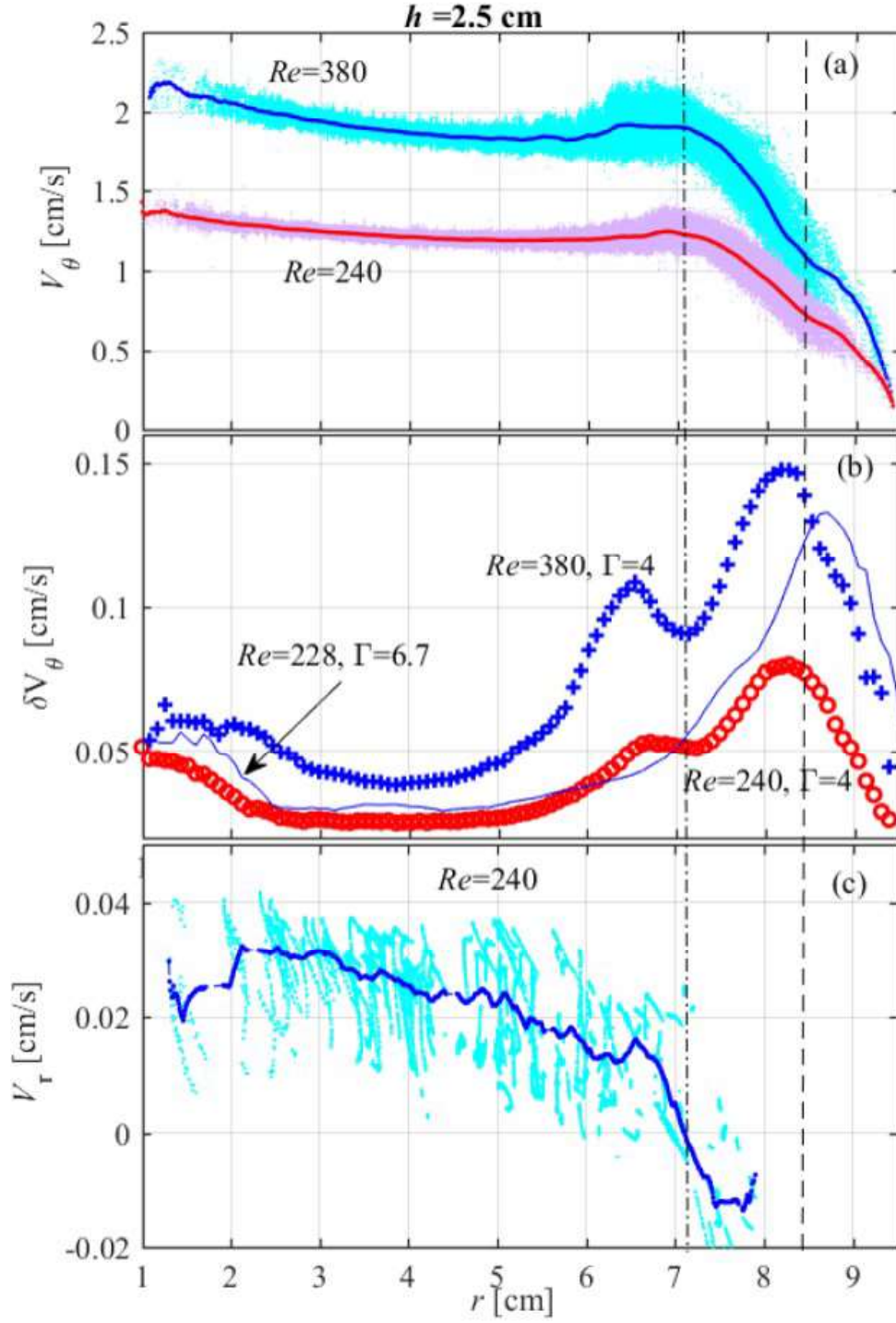


FIG. 6: In (a) and (b), we plot respectively the radial profiles of  $V_\theta$  and  $\delta V_\theta(r)$  taken at  $h = 2.5 \text{ cm}$ . For  $Re = 240$  and  $380$  we use respectively the ‘o’ and ‘+’ markers. The solid curve in (b) is for  $\delta V_\theta(r)$  taken at  $h = 1.5 \text{ cm}$  for comparison. In (c),  $V_r$  is determined at  $Re = 240$  showing a gradient at  $R - h_2 = 7 \text{ cm}$ . The two vertical dashed and dotted lines illustrate respectively the positions of maximum  $\partial_r V_\theta$  and  $\partial_r V_r$ .

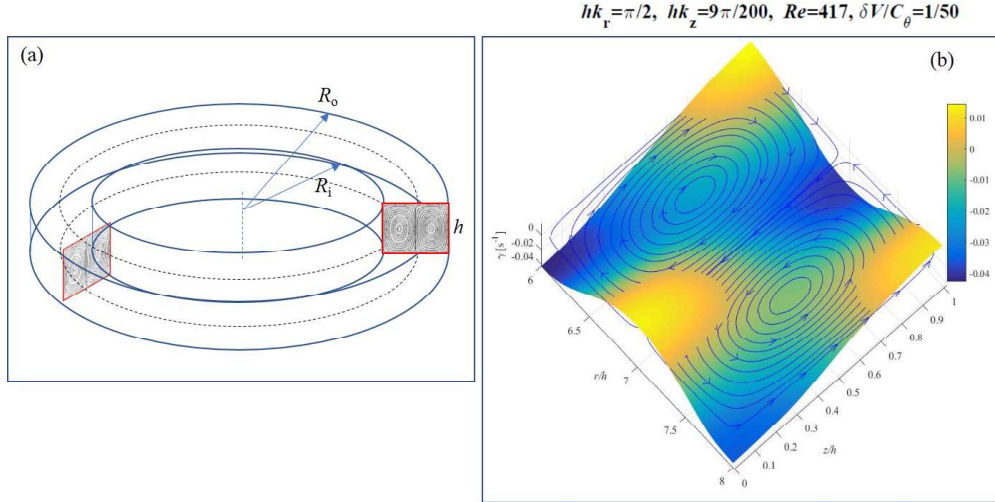


FIG. 7: In (a), we illustrate the geometry of the toroidal channel with two counter-rotating vortices in  $(r, z)$ -plane. In (b), we plot the growth rate  $\gamma(r, z)$  as a function of  $r$  and  $z$  showing where the flow is unstable at the top in-between the two vortices.

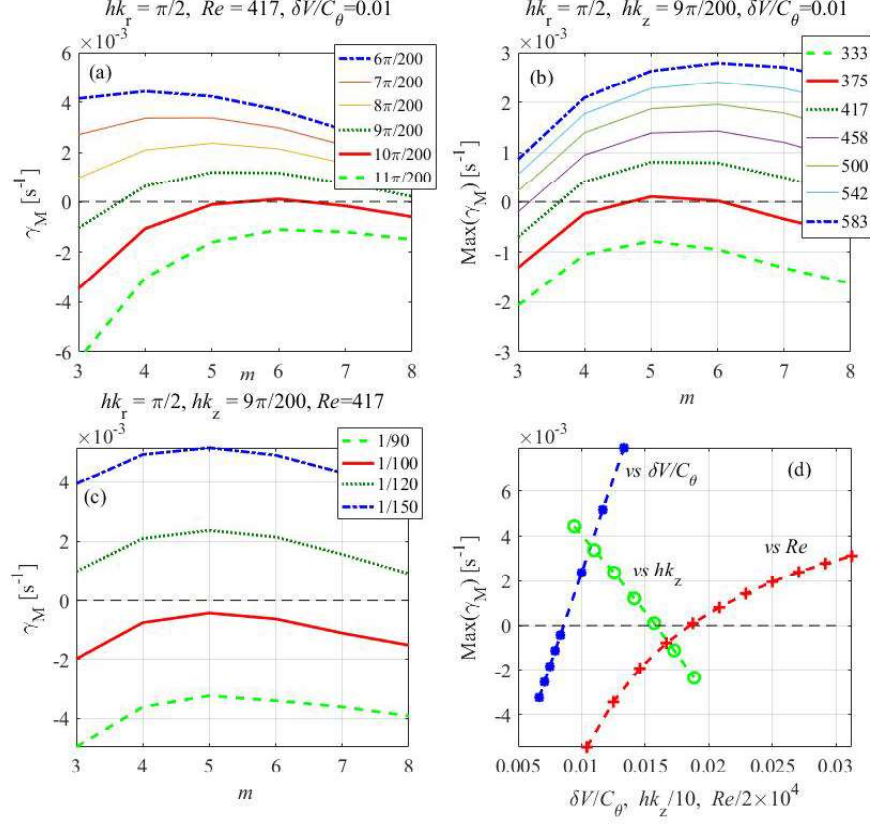


FIG. 8: The dependence of the maximum of the growth rates ( $\gamma_M = \max(\gamma(r, z))$ ) for three parameters after fixing  $hk_r = \pi/2$ . In (a), we plot  $\gamma_M$  as a function of the poloidal mode number  $m$  for different  $hk_z$  showing that the flow becomes stable with decreasing  $hk_z$ . This is shown in (d) where the maxima of  $\gamma_M$  are plotted as a function of  $hk_z$  using ‘o’ marker. In (b), the effect of the Reynolds number is investigated by changing  $C_\theta$ . The flow is unstable with increasing  $Re$  as expected but the growth rate saturates at high  $Re$  as shown in (d) using the ‘+’ marker. In (c), we illustrate the dependence of  $\gamma_M$  on  $\delta V/C_\theta$ , which reflects the relative importance of the velocity of the two counter-rotating vortices.  $\gamma_M$  increases steeply with  $\delta V/C_\theta$ , and this is highlighted in (d) using the ‘•’ marker. the figure in (d) summarizes the various dependencies where the  $x$ -axis is at the same time  $\delta V_\theta/v_\theta$ ,  $Re/2 \times 10^4$  and  $hk_z/10$  where the normalization is chosen so that all of the plots fit on the same figure.

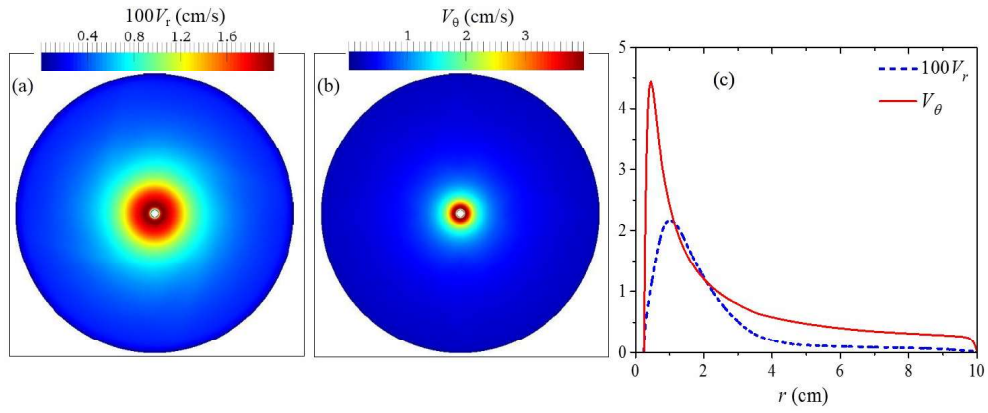


FIG. 9: In (a) and (b), we show respectively the radial and azimuthal velocity of the top fluid layer before the onset of the primary instability at  $h = 2.5$  cm. In (c), we plot the radial profile of  $V_\theta$  and  $V_r$  vs.  $r$ . Note that  $V_r$  is multiplied by 100 so that the two dependencies are visible.

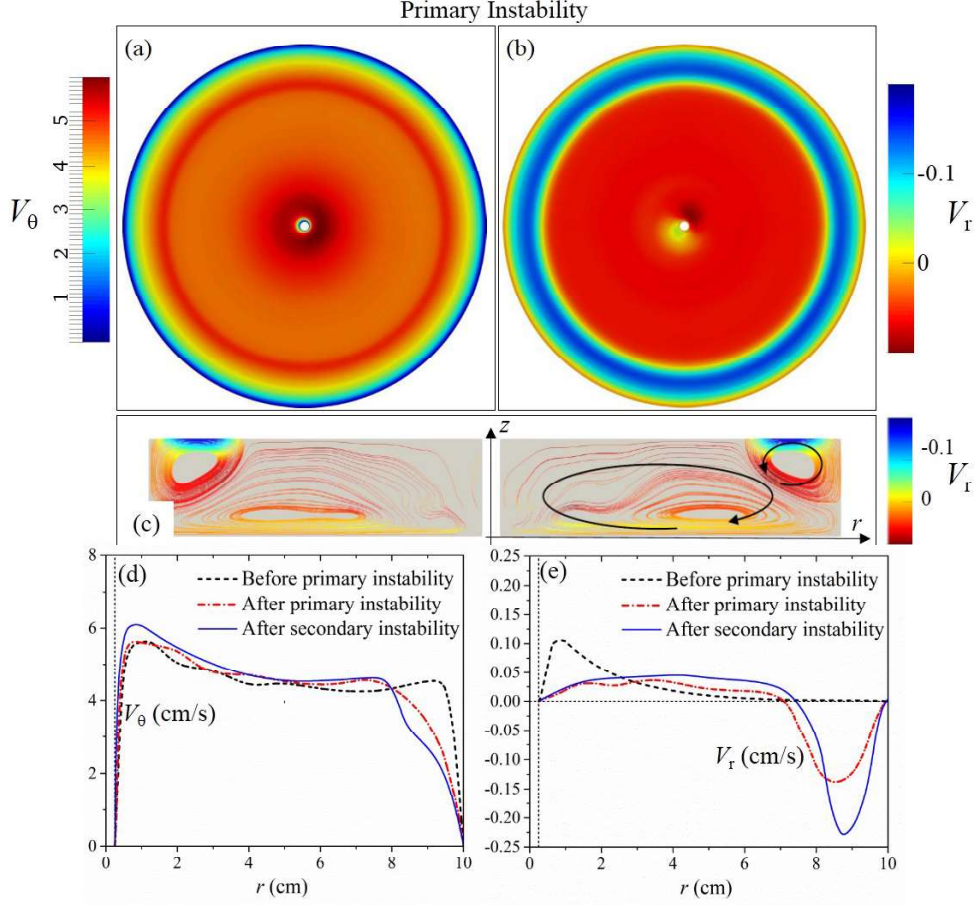


FIG. 10: In (a), we show  $V_\theta$  of the top fluid layer where the onset of the primary instability led to modifications near the outer edge. This is better seen in (b), which illustrates the dependence of  $V_r$  on space. The onset of the primary instability leads to the formation of a ring structure which reflects high radial velocities for  $r > R - h$ . In (c), we plot  $V_r$  as a function of  $r$  and  $z$  clearly showing the structure of the TC vortex. In (d) and (e), the radial profiles of  $V_\theta$  and  $V_r$  respectively at times before the onset of the primary instability (dashed line), after the primary but before the secondary instability (dash-dotted) and after the secondary instability (solid).

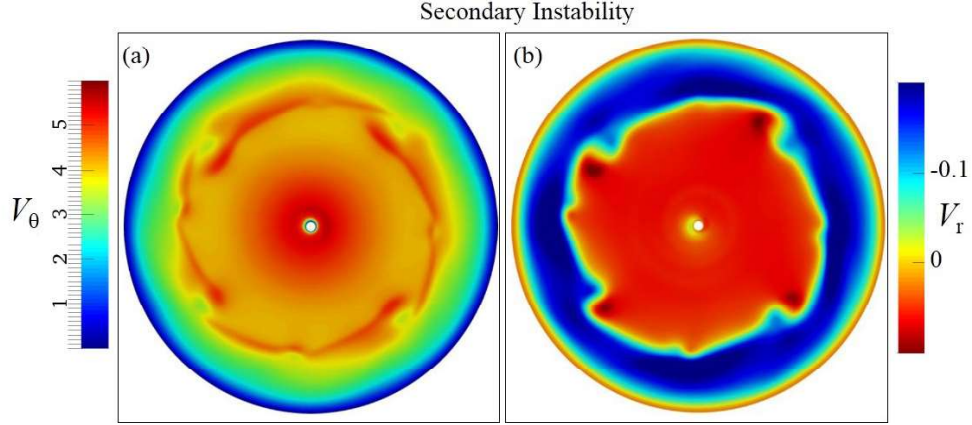


FIG. 11: In (a) and (b) we illustrate the spatial dependence of  $V_\theta$  and  $V_r$  respectively after the onset of the secondary instability. We note the existence of four vortices in the azimuthal plane in agreement with the experiment.

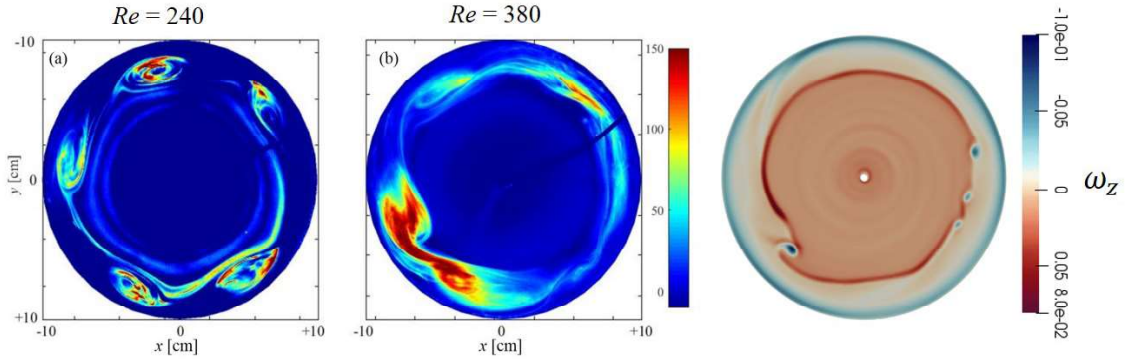


FIG. 12: In (a), we show the flow at  $Re = 240$  with  $m = 5$  vortices, in (b) we shown a case where the flow is turbulent at  $Re = 380$  and in (c) the result of the DNS.

# Bibliography

- [1] Hiroshi Niino and Nobuhiko Misawa. An experimental and theoretical study of barotropic instability. *Journal of the atmospheric sciences*, 41(12):1992–2011, 1984.
- [2] Peter M Saunders. The instability of a baroclinic vortex. *Journal of Physical Oceanography*, 3:61–65, 1973.
- [3] David J Tritton. *Physical fluid dynamics*. Springer Science & Business Media, 2012.
- [4] Peter RN Childs. *Rotating flow*. Elsevier, 2010.
- [5] R. J. Donnelly. Taylor-Couette flow: The early days. *Physics Today*, 44:32–39, November 1991.
- [6] Steven A Balbus, John F Hawley, and James M Stone. Nonlinear stability, hydrodynamical turbulence, and transport in disks. *The Astrophysical Journal*, 467:76, 1996.
- [7] Steven A Balbus and John F Hawley. A powerful local shear instability in weakly magnetized disks. i-linear analysis. ii-nonlinear evolution. *The Astrophysical Journal*, 376:214–233, 1991.



- [8] Steven A Balbus and John F Hawley. Instability, turbulence, and enhanced transport in accretion disks. *Reviews of modern physics*, 70(1):1, 1998.
- [9] Steven A Balbus. Enhanced angular momentum transport in accretion disks. *arXiv preprint astro-ph/0306208*, 2003.
- [10] Tony Maxworthy. Turbulent vortex rings. *Journal of Fluid Mechanics*, 64(02):227–240, 1974.
- [11] EJ Hopfinger and GJFV Heijst. Vortices in rotating fluids. *Annual review of fluid mechanics*, 25(1):241–289, 1993.
- [12] GJF Van Heijst and HJH Clercx. Laboratory modeling of geophysical vortices. *Annual Review of Fluid Mechanics*, 41:143–164, 2009.
- [13] M Rabaud and Y Couder. A shear-flow instability in a circular geometry. *Journal of Fluid Mechanics*, 136:291–319, 1983.
- [14] Tony Vo, Luca Montabone, Peter L Read, and Gregory J Sheard. Non-axisymmetric flows in a differential-disk rotating system. *Journal of Fluid Mechanics*, 775:349–386, 2015.
- [15] JM Chomaz, M Rabaud, C Basdevant, and Y Couder. Experimental and numerical investigation of a forced circular shear layer. *Journal of fluid mechanics*, 187:115–140, 1988.
- [16] Ana C Barbosa Aguiar, Peter L Read, Robin D Wordsworth, Tara Salter, and Y Hiro Yamazaki. A laboratory model of saturn’s north polar hexagon. *Icarus*, 206(2):755–763, 2010.
- [17] By P Hignett, AA White, RD Carter, WDN Jackson, and RM Small. A comparison of laboratory measurements and numerical simulations of baro-

- clinic wave flows in a rotating cylindrical annulus. *Quarterly Journal of the Royal Meteorological Society*, 111(467):131–154, 1985.
- [18] Frédéric Moisy, Olivier Doaré, Thomas Pasutto, Olivier Daube, and Marc Rabaud. Experimental and numerical study of the shear layer instability between two counter-rotating disks. *Journal of Fluid Mechanics*, 507:175–202, 2004.
- [19] J Pérez-Barrera, JE Pérez-Espinoza, A Ortiz, E Ramos, and S Cuevas. Instability of electrolyte flow driven by an azimuthal lorentz force. *Magneto-hydrodynamics*, 51(2):203–213, 2015.
- [20] Sergey A. Suslov, James Prez-Barrera, and Sergio Cuevas. Electromagnetically driven flow of electrolyte in a thin annular layer: axisymmetric solutions. *Journal of Fluid Mechanics*, 828:573600, 2017.
- [21] Subrahmanyan Chandrasekhar. *Hydrodynamic and hydromagnetic stability*. Courier Corporation, 2013.
- [22] R.J. Gilliam, J.W. Graydon, D.W. Kirk, and S.J. Thorpe. A review of specific conductivities of potassium hydroxide solutions for various concentrations and temperatures. *International Journal of Hydrogen Energy*, 32(3):359–364, 2007. Fuel Cells.
- [23] W.M. Haynes. *CRC Handbook of Chemistry and Physics, 97th Edition*. CRC Press, 2016.
- [24] J. N. Agar. Diffusion and convection at electrodes. *Discuss. Faraday Soc.*, 1:26–37, 1947.

- [25] C. W. Tobias, M. Eisenberg, and C. R. Wilke. Fiftieth anniversary: Diffusion and convection in electrolysis? a theoretical review. *Journal of The Electrochemical Society*, 99(12):359C–365C, 1952.
- [26] Wolf-Gerrit Frueh and Peter L Read. Experiments on a barotropic rotating shear layer. part 1. instability and steady vortices. *Journal of Fluid Mechanics*, 383:143–173, 1999.
- [27] Joseph Pedlosky. *Geophysical fluid dynamics*. Springer Science & Business Media, 2013.
- [28] On the dynamics of revolving fluids. *Proceedings of the Royal Society of London A: Mathematical, Physical and Engineering Sciences*, 93(648):148–154, 1917.
- [29] John David Jackson. *Classical electrodynamics*. Wiley, New York, NY, 3rd ed. edition, 1999.